VACCINE AND STRUCTURAL STUDIES OF SCHMALLENBERG VIRUS

PhD Thesis

Gabriel Soares Guerra

eman ta zabal zazu

Universidad del País Vasco
Euskal Herriko Unibertsitatea

2022

CIC bioGUNE
MEMBER OF BASQUE RESEARCH
& TECHNOLOGY ALLIANCE

EXCELENCIA
SEVERO
OCHOA

BRTA
BASQUE
RESEARCH &
TECHNOLOGY
ALLIANCE

VACCINE AND STRUCTURAL STUDIES OF SCHMALLENBERG VIRUS

Gabriel Soares Guerra

PhD Thesis

Thesis Supervisor:

Dr. Nicola G. A. Abrescia (CIC bioGUNE)

Tutor:

Dr. Ana María Zubiaga Elordieta (UPV-EHU)

eman ta zabal zazu

Universidad
del País Vasco

Euskal Herriko
Unibertsitatea

2022

Aknowledgements

Firstly, I would like to thank ¨La Caixa¨ Foundation for the three years of financial support for my thesis *(ID 100010434 - INPhINIT "La Caixa" fellowship LCF/BQ/DI19/11730041)* which allowed the present work to be conceived. I also thank CIC bioGUNE and all its staff for hosting me for the past three years, a research center with outstanding excellency that surely will thrive more and more in the years to come. Also, to the Universidad del País Vasco (UPV-EHU) and its staff, particularly my tutor Ana Zubiaga, for all the encouragement through these years.

I want to say thank you particularly to my thesis supervisor Nicola G. A. Abrescia. Nicola, you have (shockingly for me at the time) accepted me to get on board of your group 3 and a half years ago and, without any doubt, have been a vital piece for the acceptance of my fellowship (which I constantly remind you that you totally spoiled the day I received it by telling me I got it *yourself*). Over the past three years, I feel that I have grown not only professionally but also personally in your group by means your ¨firm¨ guidance. You truly are an example to be followed scientifically and will always be an inspiration for my future career. I sincerely hope to have fulfilled your expectations as a student, I did try to achieve that in the best way I could. I cannot help to also add that one of the biggest problems we face in countries like my home is the lack of opportunities. Once they are given to those who deserve, one can use them to build a better life, not only for oneself, but most importantly for those we love and have raised us. This is precisely the opportunity you have given me, for which I will be, forever, grateful.

I also want to thank everyone who I have worked with at the CISA-INIA. A big thank you to Nuria, Celia, Sergio, Luis, Belén, Sandra and Javier. I want to thank particularly Gemma for all the hours spent together at the endless ELISAs and for teaching me several times how to turn on the hood. I really appreciated working with you. Finally, an enormous thank you to Alejandro Brun for hosting me and for your guidance on my days at the CISA, for the many carpool rides to weight the mice at the weekends and for putting my birthday at the lab calendar. I really feel that my time in Madrid was one of the high points of my thesis and I have you all to thank for that.

I have countless thank yous for the people of bioGUNE. First, for everyone at the EM platform. Adriana for your support specially in my early days at bioGUNE, Idoia for the many adventures we had on the small microscope and for always, *always*, reminding me to sign the notebook. A big thank you to Isaac for all the experiences shared microscopically and touristically and for being such a wonderful portuguese learner. Thank you specially to Diego, now at the plaform, but above all for the years working together in our group. Apart from teaching practically everything I know now in terms of processing (which I will, forever, be thankful) I want to thank you for your enormous patience with me and for sharing your wisdom for example when you say that usually a small silly thing is the one impairing the experiment to work (which has proven to be true, too many times, sadly). Thank you for everything Diego. Thank you to Melisa for the countless times I asked for your help (not on the ultracentrifuge though) both at the lab and outside it. A big thank you and good luck at the end of your thesis for Ailleen, the second biggest fan of Madrid (I´m the first, sorry guapa), and Fer who is practically part of our group aswell. A big thank you to Diego Barriales for the several hours spent doing the experiments, particularly at the (endless) re-stimulation stainings and the FACs (where usually you left me alone now that I think of it), I could not ask for a better second author and have no doubt that you will have a brilliant career. A big thank you to Leti and finally to Juan Anguita for being practically a second supervisor to my thesis, you have unquestionably enriched the work presented here with your countless suggestions over the past three years.

I have everyone without exception from our group to thank. First to Iker specially for the assistance on poster-making and for the many coffees together. To Ander with who I sadly did not share much time but already consider part of the family. To Borja, for everything. Since you were with us as a master and now as PhD even though you sing too much, thank you very much for the friendship and your kindness with me even on moments I didn’t quite deserve it. To Miguel for being half a pupil half a mentor during my time at the group, for explaining the AAV ELISAs every time, for all the peaches and tangerines given after lunch, for my dreams, and above all for the friendship. It was always a pleasure working with you. Thank you to Juan who has been with me since I started and for the sad competition on who suffers more with tomography (probably you). I sincerely wish you all the best and, who knows, maybe you will see me in Colombia someday. Many nikes and *all* the patience of the world in this last year of PhD. I always told you that your thesis will be the coolest one and I still stand by it. Count with me for anything you need.

Thank you to Cristina for every single conversation we had when we were stressed, and of course when we were not aswell (even though we usually are, and use one another to desestress). I am very thankful for your friendship, the Salamanca tours, and all the help you have given me over these years, *especially* now at the end of the thesis. We will see each other again very soon *guapi*. I thank Antonella for being one of the most chaotic and at the same time kindest persons I have ever met, who is so similar to me in practically everything which actually concerns me. Anto, I will keep our many conversations and adventures forever with me, you are trully special to me and I have no doubt that in no time you will be visiting me wherever I am and we will have fun like we did in the past two years, I am very thankful for having met you.

Ane. I find it very difficult to say thank you and goodbye without getting emotional, which is actually fine because you are probably crying already. You have been the *best* friend I could ask for in these years in Spain. You always helped me in every single angle possible and above all was always there for me no matter what, and by no matter what I mean *literally,* from crying at the -2 to watching trash TV series or for calling me in the middle of a date to tell me you did something at the AKTA. You were there for me even when I was at my lowest, always helping me standing up. I can´t thank you enough for all that. I wish you all the happiness and fulfilment possible, professionally and personally. You are the one I will miss the most, tia.

Thank you also to the *many* friends I made in Bilbao not only in bioGUNE, but ouside it aswell. Rebeca for being my living Spanish-C2-certificate and specially for the many going-outs we had in Vitoria, for teaching me how to open my sofa, for cleaning my rug (and my wall) of wine and for sending me videos every single time you hear ABBA playing somewhere, my warmest regards to your *special* boyfriend aswell. Alexa for still talking to me after I was such a *hard* person on you on my early days at bioGUNE (when you instantly fell in love with me, I know) and for the many times we met every 4 months or something because more than that is too much for us. Mikel for being an outstanding house-mate (and even room-mate in Girona) at the first year and for all the help in my beginning here for example providing us a roof in Deusto and teaching me how to say fridge in Spanish. Julene for being so joyful all the time, helping me learn Spanish, getting lost with me in the Lekeitio island, our adventures at the sea. To Valentina for our dates in, Madrid, Rome and the ones to come. Weverton, Igor and Wallace I have to thank equally for being my piece of Brazil here In Bilbao, specially Weverton but not that much for all the vegan food I was obliged to eat.

To my best friends from Brasil: Adriana, Julia, Isabella E, Felipe B, Ilze (my biggest pride in Yale), Maria (which is actually in Portugal and my dearest Bruno too), Pedro, Rayra, Leticia P, Isabela M, Fernanda, Marília, Jaquelinne, Ana, Geovana, Caio, Carolina, Flávia, Beatriz, Camila S, Letícia C. Letícia T. Giulianna, Luciana, Lucas I, Felipe I among many others… Being far from all of you for this long was one of the most difficult decisions I ever had to make and I miss you all each and every day. Thank you for all the support through seas and 4-5 hours distance, it meant and means the world to me.

Finally, to my family. My mother Daniella, my brother Thiago, sister-in-law Luna, niece Ayan and father Osmar. We were never the standard family and probably never will be, but your support makes all my achievements possible. Os amo muito.

Obrigado, Gracias, Thank you.

*Sentaron una gitana en el extremo de la aldea e instalaron el catalejo a la entrada de la carpa. Mediante el pago de cinco reales, la gente se asomaba al catalejo y veía a la gitana al alcance de la mano****. "¡La ciencia ha eliminado las distancias!****", pregonaba Melquíades. "Dentro de poco, el hombre podrá ver lo que ocurre en cualquier lugar de la Tierra, sin moverse de su casa."*

Cien Años de Soledad

Gabriel García Márquez
Nobel Prize for Literature, 1982.

Publications

Boshra H, Lorenzo G, Charro D, Moreno S, **Guerra GS**, Sanchez I, Garrido JM, Geijo M, Brun A, Abrescia NGA. A novel Schmallenberg virus subunit vaccine candidate protects IFNAR$^{-/-}$ mice against virulent SBV challenge. **Sci Rep. 2020** Nov 23;10(1):18725. doi: 10.1038/s41598-020-73424-2. PMID: 33230115; PMCID: PMC7684302.

Guerra GS, Barriales D, Lorenzo G, Moreno S, Anguita J, Brun A, Abrescia NGA. Immunization with a small fragment of the Schmallenberg virus nucleoprotein highly conserved across the *Orthobunyaviruses* of the Simbu serogroup reduces viremia in SBV challenged IFNAR$^{-/-}$ mice. **Transbound Emerg Dis. 2022. *Under 2nd revision*.**

Conference participation

1. November 2019. Reunión de la Red Temática de Física Virológica, **Derio, Spain**.
2. August 2020. EMBO Practical Course Cryo-electron microscopy and 3D image processing, **Heidelberg, Germany**.
3. July 2021. Phage and Virus Assembly Virtual Meeting, **Portugal**.
4. September 2022. Poster presentation at the 16th MCM Multinational Congress of Microscopy ¨Preliminary Morphological Characterization of Schmallenberg Virus using cryo-TEM¨ **Brno, Czech Republic**.
5. September 2022. I Selected speaker at the 16th Vaccine Congress ¨Epitope mapping of Schmallenberg Virus Nucleoprotein unveiled an immunogen that induces cell-mediated T CD8+ protection in IFNAR -/- mice¨ **Riva del Garda, Italy**.

Ethics statement

The study was approved by the Diputación de Bizkaia as competent body for the experiments carried out at CIC bioGUNE and by the Animal Care and Biosafety Ethics' Committees of INIA and Comunidad de Madrid (Resolution PROEX192/17) for research performed at the Animal Health Research Center (INIA-CISA).

Abstract

Schmallenberg Virus (SBV) is an arbovirus that belongs to the *Peribunyaviridae* family and *Orthobunyavirus* genus, being its closely counterparts Bunyamwera virus (BUNV) and Akabane Virus. SBV was discovered in late 2011 in Germany, it is transmitted by midges' bite and have been spreading on Europe, Asia and Africa ever since. The virus causes a disease associated with ruminants that includes fever, drop on milk production, diarrhoea and stillbirths, becoming a burden for small and large farms since its discovery.

The SBV virion is pleomorphic and enveloped, enclosing its ribonucleoproteins, formed by the Nucleoprotein (SBV-N) in association with the segmented negative-sense RNA genome, beneath the lipid bilayer. The viral membrane is decorated by the G_C and G_N glycoproteins that together form the viral spike, the main mediators of viral infection. Among *Orthobunyaviruses,* the BUNV glycoprotein spike was already structurally described by cryo-EM. On the other hand, structural data on SBV for its glycoprotein spikes and the whole virons and are currently very scarce.

Concomitantly, due to the increasing spread of the arthropod vectors, there is a growing demand for alternative vaccines formulations against SBV. Hopefully, new prototypes will enter into the market in the future, complementing the current costly unattractive inactivated vaccines against SBV.

The present work builds on previous studies from our findings on SBV-N as a promising vaccine candidate. We have investigated which regions from SBV-N are responsible for protection. Based on state-of-art immunological assays using mice models, we have identified both the N-terminal domain (N-term; Met1-Thr133) and a smaller fragment of it (C4; Met1-Ala58) as promising subunit vaccine prototypes. For the structural characterization of SBV, we have optimized purification protocols in order to obtain viral particles for different EM methodologies. This allowed preliminary analyses of the whole virion morphology and the glycoprotein spikes.

Complementing vaccinology and structural studies, the present work proposes new immunogens against SBV infection at the same time that it enriches the current knowledge on the SBV morphology. Altogether, these findings are pivotal for a better understanding of the SBV pathology, finally allowing to tackle more efficiently this important veterinary pathogen in the inevitable outbreaks to come.

Resumen

Gran parte de los virus patógenos tanto humanos como vegetales y animales se encuentran dentro de las 13 familias que pertenecen al orden *Bunyavirales,* entre ellas, *Peribunyaviridae, Arenaviridae, Nairoviridae, Hantaviridae* y *Phenuiviridae*. En concreto, la familia *Peribunyaviridae* tiene cuatro géneros característicos: *Orthobunyavirus, Herbevirus, Pacuvirus y Shangavirus*.

En el género *Orthobunyavirus* la mayoría de los virus son arbovirus, es decir, transmitidos por artrópodos. Estos virus presentan una gran diversidad genética debido a su amplia distribución geográfica alrededor del mundo y son responsables por algunas enfermedades graves. Las patologías humanas relacionadas con los *Orthobunyavirus* pueden asociarse con el virus Oropouche (OROV) y el virus La Crosse (LACV). Los virus veterinarios incluyen, además del virus de Schmallenberg (SBV), el virus Bunyamwera (BUNV), el virus Akabane (AKAV) y el virus Shamonda (SHAV).

El virus BUNV es un miembro destacado, el cual fue descubierto en Uganda (1943) pero actualmente se considera endémico en muchos países africanos subsaharianos. Por otro lado, SBV fue descubierto en la segunda mitad de 2011 en la región de Renania del Norte-Westfalia, Alemania, e identificado como agente etiológico de una enfermedad desconocida asociada con el ganado lechero en esta región y en los Países Bajos. SBV se transmite por la picadura de mosquito y la sintomatología típica de la enfermedad que causa es fiebre, disminución aguda de la producción de leche y diarrea. El virus también posee la capacidad de atravesar la barrera placentaria y replicarse en el sistema nervioso central del feto, provocando malformaciones congénitas, abortos y muertes en las crías de rumiantes, lo que representa un grave problema en el sector ganadero.

La vacunación y el control de la diseminación de la población de insectos son, hasta la fecha, las formas más efectivas de controlar el contagio de SBV. Para combatir el primer brote de SBV se desarrollaron vacunas que fueron estudiadas en ovejas y vacas. Actualmente, existen tres vacunas inactivadas disponibles comercialmente que son utilizadas en Europa: Zulvac SBV (Zoetis, Bélgica), Bovilis SBV (MSD Animal Health, Reino Unido) y SBVvax (Merial, Francia).

Sin embargo, la inmunidad inducida por este tipo de vacunación se desarrolla después de 2 semanas y requiere de varios refuerzos para alcanzar una protección inmunológica más allá de seis meses, lo que implica elevados costos y tiempo, siendo una alternativa poco práctica y atractiva para los propietarios de las granjas.

Debido a la creciente propagación de los vectores artrópodos y a la colonización de nuevos nichos con factores ambientales que favorecen su propagación y reproducción, existe una creciente demanda de vacunas alternativas a las actualmente vigentes contra SBV, ya que, la presencia de este virus en nuevas regiones podría resultar catastrófica, especialmente en las pequeñas y medianas haciendas de ganado de los países subdesarrollados.

También se han ensayado prototipos de vacunas de subunidades frente a SBV, que en principio son más asequibles económicamente que las inactivadas o modificadas. En este sentido, se vacunaron pequeños roedores con la nucleoproteína del SBV (SBV-N). En concreto, la SBV-N completa producida de forma recombinante en células bacterianas junto con el adyuvante de Saponina, además de prevenir la pérdida de peso, ha disminuido la viremia en ratones desafiados con SBV.

Morfológicamente, el virión de SBV es pleomórfico y envuelto por membrana, encerrando sus ribonucleoproteínas, formadas por la SBV-N en asociación con el genoma de RNA segmentado (ssRNA) de sentido negativo (-), debajo de la bicapa lipídica. El genoma de SBV consta de tres segmentos de ssRNA (-), flanqueados por regiones no traducidas en las extremidades 3´ y 5´ con una organización de codificación similar y denominadas según su tamaño: Pequeño (S), Mediano (M) y Grande (L).

El segmento L es responsable de codificar las polimerasas de RNA dependientes de RNA, estas proteínas son responsables de la transcripción del RNA (-) en RNA mensajero (RNAm) de sentido positivo (+) para que pueda ocurrir la traducción de proteínas. El segmento M codifica las dos glicoproteínas G_N y la G_C, junto con una proteína no estructural NSm. Finalmente, el segmento S codifica la SBV-N.

La envoltura viral está decorada por las glicoproteínas G_C y G_N, proteínas transmembrana que atraviesan la membrana lipídica viral y que juntas forman la espícula viral. La espícula es el principal mediador de la infección del virus. Por esa razón, la organización de las glicoproteínas virales es de gran importancia debido a (i) su papel vital en las primeras etapas del ciclo de vida viral al unirse principalmente a los receptores de las células huésped; (ii) la fusión de membranas, ya que los virus que poseen envueta lipídica fusionan su propia membrana con la de la célula huésped para entregar el genoma al citoplasma celular; (iii) el ensamblaje viral, por ejemplo, se propuso que las colas citoplásmicas de la proteína G_N ya sirven como proteína matriz; (iv) por seren factores de restricción de tropismo y (v) el objetivo principal de las defensas inmunitarias del huésped, siendo los complejos de la glicoproteína de la espícula objetivos interesantes para el desarrollo de fármacos y vacunas.

Entre los *Orthobunyavirus*, la glicoproteína de la espícula de BUNV ya se describió estructuralmente de manera extensa. Los complejos de espícula de BUNV, descrito por tomografía crioelectrónica (Cryo-ET), adoptan una estructura tripodal única que cubre toda la superficie del virión y se subdivide en tres regiones: la región del piso proximal de la membrana, compuesta por proteínas G_C y G_N, la región de la cabeza distal de la membrana en la punta de la espícula, que está compuesta únicamente por la porción N-terminal de la G_C y una región de tallo, que conecta ambas regiones y presumiblemente también está compuesta por la G_C.

La G_C de BUNV, y también de SBV, ya fueron resueltas por cristalografía de rayos X. En este sentido, la G_C de SBV muestra un buen ajuste dentro del mapa de densidad electrónica de la espícula del BUNV. Inicialmente, se propuso que tanto la G_C de SBV como de la de BUNV adoptan una configuración de trímero en sus porciones N-terminales en la punta de la espícula de glicoproteína. Sin embargo, la baja resolución de la espícula de BUNV perjudica una asignación de dominio correlacionada con la secuencia. En conjunto, los datos estructurales sobre las glicoproteínas de la espícula y los virones de SBV enteros son actualmente muy escasos.

El presente trabajo se basa en estudios previos de nuestros hallazgos sobre SBV-N como un candidato a vacuna prometedor. Como ya se mencionó, la SBV-N completa tenía la capacidad de proteger a los pequeños roedores desafiados (ratones IFNAR$^{-/-}$), lo que resultó en una fuerte inmunidad mediada por células. En esta tesis, hemos investigado qué regiones de la SBV-N son responsables de la protección. Primero, probamos varios péptidos derivados de la SBV-N como posibles inmunógenos y epítopos para el complejo MHC-I.

A continuación, producimos varias construcciones proteicas a partir de secciones de la SBV-N para usarlas como candidatos a vacunas de subunidades. Hemos realizado distintos ensayos inmunológicos de última generación utilizando modelos de ratones IFNAR$^{-/-}$ y C57BL/6.

Realizamos (i) clasificación de células activadas por fluorescencia (FACs) para caracterizar las poblaciones de CD8+ tras la re-estimulación de esplenocitos de ratones C57BL/6 vacunados con las subunidades candidatas a vacuna; (ii) análisis de la secreción de interferón-γ (IFN-γ) en esplenocitos de ratones IFNAR$^{-/-}$ desafiados y C57BL/6 no-desafiados; (iii) ensayos de reacción en cadena de la polimerasa cuantitativa con transcripción inversa en tiempo real (RT-qPCR) para caracterizar la viremia sanguínea de ratones IFNAR$^{-/-}$ tras la vacunación y el desafío viral.

Al final, hemos identificado tanto el dominio N-terminal (N-term; Met1-Thr133) como un fragmento más pequeño del mismo (C4; Met1-Ala58) como prototipos prometedores de vacunas de subunidades, capaces de generar respuestas TCD8+ específicas del virus en ratones. Además, la conservación de la secuencia evolutiva de la porción C4 de la SBV-N y de la nucleoproteína en otros virus del serogrupo Simbu (como AKV, BUNV y SHAV) podría ser el paso inicial en el desarrollo de una vacuna de nanopartículas con posibles propiedades de protección cruzada, siendo una posible "pan" vacuna contra varios *Orthobunyavirus*.

Para la caracterización estructural de SBV, primero hemos optimizado los protocolos de purificación para obtener partículas virales para diferentes metodologías de microscopía electrónica (EM). Tuvimos como punto de partida una metodología derivada de la purificación de viriones de BUNV. Demostramos la eficacia de gradientes de densidad continuos y discontinuos sometidos a ultra-centrifugación para separar las partículas de SBV producidas por células de riñón de Hamster bebé (*Baby Hamster Kidney*; BHK).

Como control de calidad, investigamos el efecto citopático de las partículas producidas, así como la ligación con un anticuerpo dirigido a la proteína G_C de las espículas virales seguido de tinción negativa y visualización por microscopía electrónica de transmisión (TEM).

La implementación sistemática de la producción de partículas de SBV permitió el análisis preliminar de la morfología del virión completo y las glicoproteínas de su espícula. Las micrografías obtenidas por crio-EM que albergan los viriones SBV producidos permitieron una distinción directa de características estructurales virales tales como (i) el interior densamente empaquetado; (ii) la bicapa lipídica y (iii) las densidades por encima de la envoltura de la membrana, correspondientes a las espículas G_C/G_N. La presencia de tales espículas ¨coronando¨ la envoltura viral permitió una caracterización estructural 2D de la misma.

Como resultado, las densidades en la parte superior de las bicapas de las partículas de SBV proporcionaron un promedio inicial del complejo de espícula de aprox. 5-7 nm, entre dos y tres veces más corta que la espícula de BUNV. A continuación, se logró una caracterización preliminar por crio-ET del complejo de espícula G_C/G_N de SBV.

Después de distintas metodologías de promedio de sub tomogramas (*sub tomogram averaging*; STA), se recuperaron capas de alta densidad en los volúmenes resultantes. Nuestra caracterización 3-D permitió estimaciones preliminares de esas densidades. Ese análisis muestra que las regiones de alta densidad correspondientes a la espícula viral se encuentran a aprox. 4.2-6.3 nm de las densidades de la envoltura viral.

Los resultados morfológicos del presente trabajo aún se encuentran en una fase inicial, pero representan un avance en nuestro conocimiento actual de la morfología de SBV y la caracterización de las glicoproteínas G_C/G_N, lo que proporciona una visión global de la arquitectura del complejo de espícula de SBV. Señalamos que las espículas de SBV G_C/G_N no siguen la misma organización que BUNV, como se propuso anteriormente. Para tener en cuenta, en la literatura no se dispone de una metodología para la producción de SBV ni imágenes derivadas de crio-ET del virión completo, así como de las glicoproteínas G_C/G_N.

En conclusión, el presente trabajo (i) propone nuevos inmunógenos contra la infección por SBV (construcciones N-terminal y C4) mediante varias metodologías inmunológicas y (ii) enriquece el conocimiento actual sobre la morfología y descripción de la espícula de glicoproteína del SBV, obtenida por diferentes metodologías de crio-EM. En conjunto, estos hallazgos son fundamentales para una mejor comprensión de la patología del SBV, lo que finalmente permitirá abordar de manera más eficiente este importante patógeno veterinario en los inevitables brotes que se avecinan.

Abbreviations

Å: Angstrom

aa: Amino acid

Ab: Antibody

AG-HE: Arthrogryposis and Hydranencephaly syndrome

α: Rotation angle alpha

Amp: Ampicilin

ANDV: Andes Virus

AINOV: Aino Virus

AKV: Akabane Virus

AU: Asymmetric Unit

β: Rotation angle Beta

BHK: Baby Hamster Kidney

bps: base pairs

BoLA: Bovine leukocyte antigens

BSA: Bovine Serum Albumin

BUNV: Bunyamwera Virus

C2: Construct 2

C3: Construct 3

C4: Construct 4

C57BL/6: C57 black 6 mice

C_C: Chromatic Aberration

CC: Cross Correlation

CCC: Constrained Cross Correlation

CCD: Charge Coupled Device

CCHFV: Crimean-Congo Haemorrhagic Fever Virus

CME: Clathrin-mediated endocytosis

CNS: Central Nervous System

ConA: Concanavalin A

CPE: Cytopathic effect

Cq: Quantification Cycle

Cryo-EM: Cryo-electron microscopy

Cryo-ET: Cryo-electron tomography

C_S: Spherical Aberration

C-Terminal: Carboxy terminal

CTF: Contrast Transfer Function

CVV: Cache Valley Virus

ΔZ: Defocus

DMEM: Dulbecco’s modified Eagle’s médium

DMSO: Dimethyl Sulfoxide

DOUV: Douglas Virus

Dpi: Days post infection

DQE: Detective Quantum Efficiency

dsRNA: Double Stranded RNA

DTT: Dithiothreitol

e^- : Electron

EIP: Extrinsic Incubation Period

ELISA: *Enzyme-linked immunosorbent assay*

EM: Electron microscopy

EMDB: Electron Microscopy Data Bank

ER: Endoplasmic Reticulum

FACs: Fluorescence-Activated cell sorting

FBS: Fetal Bovine Serum

FSC: Fourier Shell Curve

FT: Fourier Transform

FT^{-1}: Inverse Fourier Transform

GPC: Glycoprotein Precursor

GST: Glutathione S-transferase

HAZV: Hazara Virus

HSPG: Heparan Sulphate proteoglycan

ICTV: International Committee in Taxonomy of Viruses

IFN: Interferon

IFNAR$^{-/-}$: Knockout for type-I interferon receptors mice

IgG: Immunoglobulin G

IIP: Intrinsic Incubation Period

IPTG: isopropyl β-d-1-thiogalactopyranoside

KAIV: Kaikalur Virus

Kan: Kanamycin

kDa: Kilodalton

kV: Kilovolt

LACV: La Crosse Virus

λ: Wavelenght

LAMP: Lysosomal-associated membrane protein

LASV: Lassa Virus

LB: Luria-Bertani

LPF: Low Pass Filter

mAb: Monoclonal Antibody

MBP: Maltose Binding Protein

MHC-I Major Histocompatibility Complex class I

MOI: Multiplicity of Infection

MP: Matrix protein

mRNA: Messenger RNA

MS: Mass-spectroscopy

MTF: Modulation Transfer Function

MW: Missing Wedge

MWCO: Molecular Weight cut-off

NA: Numerical Aperture

NAbs: Neutralizing antibodies

N-terminal: Amino terminal

OD: Optical Density

ORF: Open Reading Frame

OROV: Oropouche Virus

PBS: Phosphate Buffer Saline

PBST: Phosphate Buffer Saline Tween-20

PCR: Polymerase chain Reaction

PD: Proportional Distance

PDB: Protein Data Bank

PEAV: Peaton Virus

PFA: Paraformaldehyde

Ψ: Rotation angle; Azymuth rotation

PUUV: Puumala Virus

R0: Basic reproductive number

RdRp: RNA-dependent RNA polymerase

ρ: density (g/mL)

RNAm: Messenger RNA

RNP: Ribonucleoprotein

RSV: Rous Sarcoma Virus

RT-qPCR: Real-time reverse transcription quantitative polymerase chain reaction

RVFV: Rift Valley Fever Virus

SANV: Sango Virus

SATV: Sathuperi Virus

SBV: Schmallenberg Virus

SBV-N: Schmallenberg Virus Nucleoprotein

SD: Standard deviation

SDS-PAGE: Sodium dodecyl-sulfate polyacrylamide gel electrophoresis

SEC: Size exclusion chromatography

SENP2: Sentrin-specific-protease-2

SFV: Semliki Forest Virus

SHAV: Shamonda Virus

SIRT: Simultaneous Iterative Reconstruction Technique

SNR: Signal to noise ratio

SP: Signal Peptide

SPA: Single Particle Analysis

ssRNA: Single Stranded RNA

STA: Sub tomogram averaging

SUMO: Small ubiquitin-like modifier

TCD8: Cytotoxic T lymphocyte

$TCID_{50}$: Tissue Culture Infectious Dose

TINV: Tinaroo Virus

TULV: Tula Virus

Uac: Uranyl Acetate

UTR: Untranslated Region

WBP: Weighted back-projection

GENERAL INDEX

Chapter 1:

INTRODUCTION

I. The threat of the *Orthobunyavirus* genus

The *Bunyaviridae* family, which was elevated to the rank of order and named as *Bunyavirales* in 2017 by the International Committee on Taxonomy of Viruses (ICTV) to better accommodate the increasing number of related viruses constantly identified. It is, to date, the most diverse known group of RNA viruses comprising more than 350 named isolates, infecting a broad range of hosts (1). This group of viruses is characterized for being enveloped by a lipid bilayer and harbour a negative sense (-) single stranded RNA (ssRNA) genome. The viral particles rely on their own RNA dependent RNA polymerases (RdRp) to make copies of the genetic material. Their genome is fragmented in two to six segments, having the different sections of RNA individual jobs on the viral life cycle, as described later on (2,3).

The *Bunyavirales* order was named after Bunyamwera virus (BUNV), the best characterized virus from the group. BUNV was first isolated in the Semliki Forest, Uganda, in 1943 from *Aedes* spp. Mosquitoes. This virus is now considered endemic in many African sub-Saharan countries such as Nigeria, Tanzania, Mozambique and Democratic Republic of Congo (4).

The *Bunyavirales* order contains 13 families, several of them containing important human, plant and animal pathogens, being the *Peribunyaviridae, Arenaviridae, Nairoviridae, Hantaviridae, and Phenuiviridae* families' classical examples (5) (Figure 1). Specifically, the *Peribunyaviridae* family, having BUNV as its prototype member (Table 1), has four characterized genera: *Orthobunyavirus*, *Herbevirus*, *Pacuvirus* and *Shangavirus*.

Order	Family	Genus	Virus members
Bunyavirales	*Peribunyaviridae*	*Orthobunyavirus*	Bunyamwera virus, Akabane Virus, Shamonda virus, Schmallenberg Virus, La Crosse virus, Oropouche Virus, Douglas Virus, Peaton Virus Tinaroo Virus
		Herbevirus	Herbert Virus
		Pacuvirus	Pacui Virus
		Shangavirus	Shuāngào insect virus 1

Table 1. Summary of *the Peribunyaviridae* family. Adapted from Hughes *et al.* 2020.

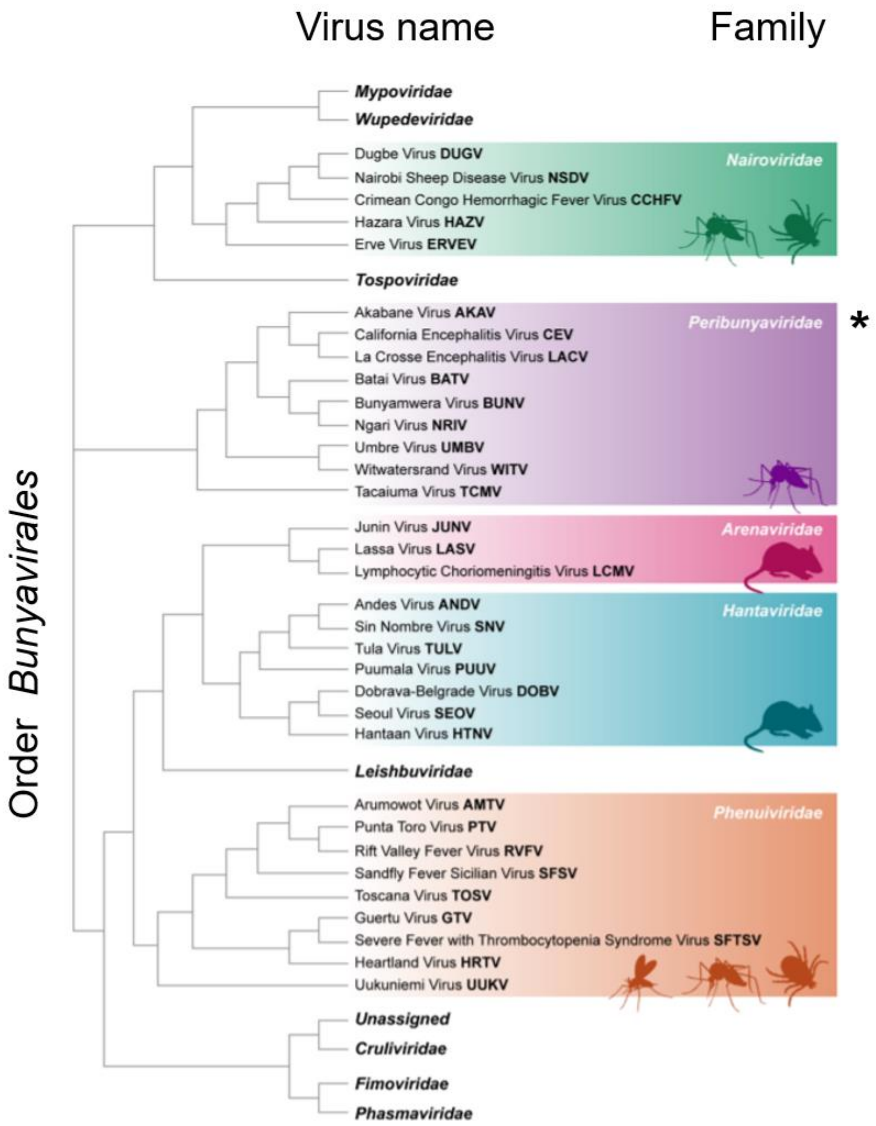

Figure 1. *Bunyavirales* order phylogenetic tree. The classification was made based on the nucleoprotein amino acid (aa) sequence of 13 families from the order. The distances are not scaled. The distinct families are shown in bold right after the tree node or in white at the coloured areas. Viruses' names are given before their abbreviations (in bold). Animals that work as vectors from viruses from a particular family are shown in shadows. The *Peribunyaviridae* family is denoted with an asterisk. Adapted from Leventhal *et al*. 2021.

Among the four, the *Orthobunyavirus* is of increasing importance being the one with the most pathogens characterized. This genus includes 19 different serogroups and 48 species complexes. Most of the viruses from this genus are arboviruses (arthropod transmitted) and, aside from having a great genetic diversity due to their broad geographic distribution around the globe, are responsible for some serious diseases, both veterinarian and human (6).

Human pathologies related with *Orthobunyaviruses* can be associated with Oropouche virus (OROV) for example, which is the cause of the Oropouche fever. This disease is similar to dengue with common symptoms such as headache, fever and muscle pain that may progress to encephalitis in more serious cases. OROV was first detected in 1955 in the Amazonian region and since then it has been responsible for several epidemics in the South and Central Americas (7). La Crosse Virus (LACV) on the other hand, isolated post-mortem from the brain of a child in Wisconsin, USA, is transmitted by the *Aedes triseratus* mosquito and usually causes mild fever. Still, on severe cases the disease can develop to seizures, meningoencephalitis, paralysis and even death. Moreover, the LACV fever is considered the most common cause of pediatric arboviral encephalitis in the USA (8).

As for the *Orthobunyaviruses* that pose as animal threats, Akabane virus (AKV) was first isolated in the village of Akabane, Japan, in 1959. It is transmitted by midges and is the main cause of hydrocephaly in ruminants in Australia, Japan, Korea, among other countries in Africa and the Middle East. Outbreaks of congenital malformations caused by AKV occur when environmental conditions allow midges to disperse beyond their normal range and are able to infect naïve cattle (9, 10). Another veterinarian disease causing *Orthobunyavirus* pathogen Aino virus (AINOV), closely related to AKAV, is also associated to stillbirth, abortions and calve malformations when pregnant animals get infected and is endemic on the same Asiatic and Oceanic regions (11).

Shamonda Virus (SHAV), another *Orthobunyavirus* associated with disease in ruminants, was first isolated in Nigeria in 1965 and re-emerged in Japan on the early 2000s (12). Cache Valley virus (CVV), on the other hand, was first isolated in the state of Utah, USA, in 1956 and is considered endemic in North America, the Caribbean and Argentina. CVV has a deep economic impact on the sheep industry in these regions, causing fetal malformations and abortions (13). Other relevant veterinarian pathogens among *Orthobunyaviruses* are Douglas (DOUV), Peaton (PEAV) and Tinaroo (TINV), all viruses associated with congenital deformities in ruminants in Asia, Africa and Oceania (9).

New *Orthobunyaviruses* are constantly being identified, having the number of species catalogued almost doubled from 49 in 2011 to 87 in 2019 according to the ICTV (14, 15). It is speculated that this rapid increase has direct or indirect relation with human action on climate change, specifically on massive deforestation and cattle farming (16). In general, severe diseases affecting the Central Nervous System (CNS) from the mammal hosts are caused by many *Orthobunyaviruse*s. As exemplified before with LACV, OROV among others, this family genus is of urgent importance for human and animal health around the globe (15).

II. Schmallenberg Virus (SBV): Discovery, pathology and epidemiology

Schmallenberg Virus (SBV), a member of the *Peribunyaviridae* family, *Orthobunyavirus* genus and Simbu serogroup, was first detected in the second half of 2011 in the region of North Rhine-Westphalia, Germany. The virus was identified as the etiological agent of an unidentified disease associated with dairy cattle in this region and in The Netherlands that included fever, an acute drop on milk production and diarrhea. Metagenomic analyses from blood samples of a cattle farm near the town of Schmallenberg, Germany, confirmed that the pathogen was closely related to *Orthobunyaviruses* from the Simbu serogroup, being its closely counterparts SHAV, AINOV and AKV, all previously described as domestic animal pathogens (17).

Remarkable pathological characteristics from these close related viruses were soon identified for SBV, as well as its transmission by biting arthropods and by crossing the placental barrier. The latter mode of transmission allows the viral replication in the foetuses CNS and ultimately leads to congenital malformation and stillbirths in the ruminant offspring (18). The first malformed animal as a direct cause of a SBV infection was detected in the Netherlands in late 2011 and the symptoms included arthrogryposis along with several neuronal malformations on the brain, cerebellum, hydrocephaly and porencephaly (19).

The musculoskeletal defects observed in aborted foetuses and neonates, the direct consequences of lesions on the spinal cord caused by the virus, along with the hydrocephaly previously detected, culminates with the arthrogryposis and hydranencephaly syndrome (AG-HE). The AG-HE is the most severe scenario of SBV infection on animal offspring that ultimately leads to death on affected animals (20, 21) (Figure 2).

Figure 2. AG-HE syndrome. SBV positive by RT-qPCR calves showing severe arthrogryposis and musculoskeletal alterations such as limb deformities, Obtained from Garigliany *et al*. 2012.

In adult cattle, which become infected by the biting of an infectious *Culicoides* vector and develop viraemia, symptoms are typically unspecific ranging from mild to moderate: loss of body condition, hyperthermia, diarrhea and drop in milk production, being the latter an important economic problem specially for small and medium size farms (18). After passing the infection, animals possess antibodies against SBV for at least two years (22, 23). Apart from being primarily identified in farm animals such as cattle, goat and sheep, SBV RNA or antibodies against this virus have also been identified in several wild and exotic ruminants. Alpacas, deers, bisons, buffalos and even camelids were detected as SBV positive in a number of European countries from 2012 onwards (24). Non-ruminant species reported with direct or indirect infection with SBV include wild boars, horses and several exotic animals on UK zoos (25-27).

During 2012, several European countries such as France, Italy and Spain reported positive cases of SBV infection (28). The virus spread through Europe in 2013 and reached Asia being first reported in Turkey in March 2014 (29). In the period following the initial 2011 and 2012 outbreak until 2015, several reports have described a low, but constant, circulation of the virus in European countries. Méroc and colleagues have described a great decline of the viral spread in 2012 following the first outbreak, which meant that younger animals had lower chances to get infected in the following vector seasons (30). Indeed, the scenario above manifested in Germany in 2014, where the virus re-emerged due to a decline in the herd seroprevalence caused by the absence of infection in the younger stock, untouched by the initial outbreaks in the vector seasons of 2011 and 2012 (31). This high initial herd immunity also reduced SBV circulation in Ireland during 2014 and 2015 vector seasons (32). Same as reported for other *Orthobunyaviruse*s, its re-circulation is most likely cyclical and imminent, aggravated by climate change which modulates vectors' population and spreading (16).

As mentioned previously, SBV is an arbovirus, being the haematophagous insects from the *Culicoides* genus the main vectors responsible for the dissemination of this virus. More specifically, SBV RNA was already detected in *C. obsoletus, C. scoticus,* and *C. dewulfi*, all belonging to the *C. obsoletus* group. The virus was also reported in *C. pulicaris* and *C. punctatus*, from the *C. Pulicaris* group (24). Other insect species which have tested positive for SBV genome include *C. nubeculosis, C. imicola, C. newsteadi,* and *C. lupicaris* (33, 34, 35).

Regarding the transmission cycle of SBV, uninfected insects that feed on the blood of a SBV-infected mammalian host become rapidly infected (24). Still, a vector being infected is not the same as being infectious. The extrinsic incubation period (EIP), the time gap between ingestion of infected blood and the ability to transmit the virus to a new host, is directly related to the temperature of the microenvironment were the midges rest after feeding. Such period accounts for 90% of the vector´s lifetime and is also when oocytes are produced (36,37). The EIP for the SBV infected *Culicoides* can go from 9 to 41 days, depending on the temperature of the environment (38).

The transmission from insect to mammalian host happens via saliva when an infectious female *Culicoides* bites immunologically naïve animal. The intrinsic incubation period (IIP), in which the virus is now replicating inside the mammalian host, can go between 2 and 6 days (17). When a pregnant mammalian female gets bitten by an infectious insect, following the IIP, the virus crosses the placental barrier. By reaching the offspring in formation, SBV can lead to serious malformations specially by reaching the still not fully developed CNS, as previously pointed out (39).

In 2016, a new outbreak of congenital malformations and stillbirth on ruminants was reported in different European countries that were already affected in previous vector seasons such as Belgium and Ireland (40,41). SBV is, to this date, continuously spreading and new reports have indicated its presence in cattle from eastern Europe countries such as Kosovo and Albania (42). Also, as mentioned before with its first detection in Turkey (29), the virus was either direct or indirectly detected in countries outside Europe such as Israel (43,44), China (45), Namibia (46), Iran (26), Azerbaijan (47), Lebanon (48), Mozambique (47), Ethiopia (49) and South Africa (50). Overall, this demonstrates the broad spreading of SBV through the planet since its first detection and raises concerns globally (Figure 3).

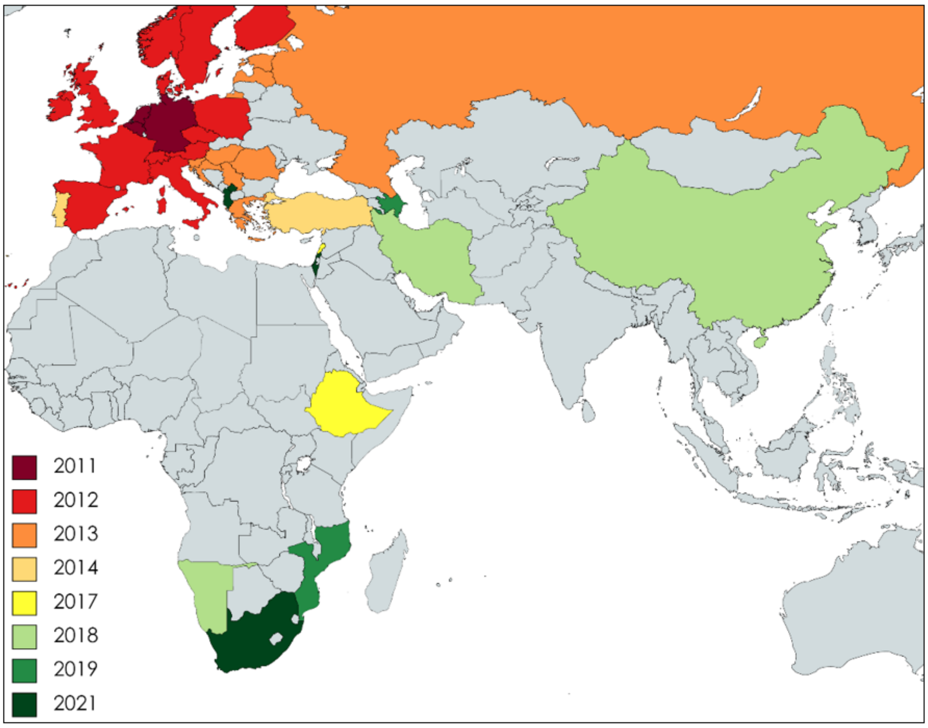

Figure 3. Schmallenberg virus dispersion in the world until 2021. SBV positive reports on different countries according to year of first detection either by RT-qPCR, serology of calves presenting arthrogryposis and musculoskeletal alterations or vector surveillance positive RT-qPCRs *Culicoides*. Modified from Collins *et al*. 2019. Map created with mapchart.net ©.

In 2014, Gubbins and colleagues have developed a mathematical model for the transmission of SBV suggesting that vector dispersal is the main mechanism of action for the virus spreading (51). In fact, environmental factors have recently been linked to the dynamics of infectious diseases by arboviruses, in which vector abundance so as breeding rates can be modulated by changes in temperature (52,53). If SBV reaches new regions that have not yet reported its presence it could mean catastrophic outcomes, especially regarding small and medium size farms of underdeveloped countries.

III. Detection, immunology and current vaccine development against SBV

Genome and/or serological diagnosis is needed to confirm the suspicion of SBV infection, especially due to similarities between clinical features of SBV caused disease and other ruminant viral infection. For example, Crimean-Congo Haemorrhagic Fever Virus (CCHFV) (fam. *Nairoviridae*) and Rift Valley Fever Virus (RVFV) (fam. *Phenuiviridae*) cause diseases that could eventually lead to cross-reactivity (54). Currently, being virus isolation not always ideal due to low viral titers in most biological samples including blood, real-time reverse transcription quantitative polymerase chain reaction (RT-qPCR) allows a fine and specific detection of the viral genome confirming infection. The pitfall of using this technique is that only samples from the CNS such as brain, brain stem and spinal cord, along with placental fluid and umbilical cord, have proven to be appropriate for reliable viral detection (55-58).

The basic reproductive number (R0) for the virus reaches highs of 7.7 and 6.2 for sheep and cattle farms (59). This high spreading significantly reduces the chances of finding seronegative animals among a population that already had a first contact with the virus and diminishes the chances of severe complications in pregnant cattle and ewe if the infection happens between the 3rd and the 6th month of a nine months pregnancy (60, 61). Thus, the SBV infection of naïve animal populations leads to the development of a robust immunity (22). It has been demonstrated that anti-SBV antibodies can last as far as 48 and 38 months on sheep and cattle, respectively (20). Moreover, it has been shown that offspring born from previously infected animals remains protected against the virus for at least six months of life (62).

Inactivated vaccines against SBV were quickly developed to combat the first virus outbreak and had their efficacies tested in sheep and cows (63,64). Also, a modified live vaccine with deletions at key segments of the viral genome had resulted in high protection against infection although its safety is still under tests (65). A modified Equine Herpes Virus 1 expressing the SBV spike protein resulted in partial protection in cattle at the same time that a Vaccinia Virus Ankara expressing the same protein conferred full protection (66).

Currently, three commercially available inactivated vaccines, Zulvac SBV (Zoetis, Belgium) Bovilis SBV (MSD Animal Health, UK) and SBVvax (Merial, France) have been in use in European countries. Moreover, the so-called inactivated vaccine-induced immunity develops after no longer than 2 weeks after vaccination (64). Still, the duration of the immunity is a concern, being several boosts required for protection beyond 6 months. That *per-se* make the inactivated vaccines somewhat cost unattractive for the farm owners to buy.

Subunit vaccines prototypes against SBV, which are in principle more economically affordable than the inactivated or modified ones, have also been tested. Prototypes which contained the full or partial G_c and G_N proteins of the viral spike produced in human embryonic kidney cells (HEK) provided only a partial protection in challenged cows. On the other hand, no protection was detected using these same proteins, further produced in Baculovirus (67). Robust protection of cattle, however, was obtained when the animo terminal (N-terminal) portions of G_C from SBV and AKV were covalently linked together and used as immunogens (68).

A DNA vaccine which coded for SBV G_C along with the coding sequence of SBV nucleoprotein (SBV-N) have proven to prevent weight loss in small rodents (69). Moreover, the full SBV-N recombinantly produced in bacterial cells in conjunction with saponin adjuvant has, aside from preventing loss of weight, diminished the viraemia in mice challenged with SBV (70). Vaccination, along with surveillance of insect population dissemination are, to date, the most effective ways of controlling the SBV spread. Specifically, the vaccination on breeding animals is the most critical in order to prevent the foetal infection and consequently the most drastic outcomes of the disease, the AG-HE syndrome, abortions and stillbirths (20,58).

IV. Molecular biology of SBV

The genome of SBV consists of three (-) ssRNA segments flanked with 3´ and 5´ untranslated regions (UTRs) with a similar coding organization and named depending on their sizes: Small (S), Medium (M) and Large (L) (21,71,72) (Figure 4). Regarding this sizes, usually consistent within the *Orthobunyavirus* genus, they are about 7.0 kb for the L, 4.5 kb for the M and 1.0 kb for the S. Besides, the terminal base pairs at the 3´ and 5´ UTRs are complementary, a feature that allows a formation of a ¨panhandle¨ structure important for the positive-sense (+) messenger RNA (RNAm) synthesis by the RdRps (72). Similar to other RNA arboviruses, antigenic drift in SBV is limited i.e., mutations that could significate an advantage at the mammal host might impair replication into the insect host and vice versa (42). It is plausible then to assume that the virus has, with some exceptions, a somewhat stable genome in terms of mutations, which has been demonstrated both *in vivo* and *in vitro* (73).

Since the genomic segments have a (-) polarity first they have to be transcribed into (+) mRNA so that translation can occur. This process relies on the RdRp encoded by the L segment (21). Apart for being responsible both for catalysing transcription and genome replication, the N-terminal section of the RdRp contains an endonuclease domain that has the ability to cleave the capped oligonucleotides from hosts mRNA 5´ ends. Afterwards, these ¨caps¨ are used to prime its own viral mRNA transcription. This mechanism, known as cap snatching, was first described for Influenza Virus (fam. *Orthomyxoviridae)* (74) and is now known to be broadly used by segmented negative sense segmented RNA viruses such as the ones from the *Bunyavirales* order and the *Orthomyxoviridae* family (75,76). The cap snatching mechanism takes place at the nucleus and cytoplasm of the host cell in *Orthomyxoviridae* and *Bunyavirales* infections, respectively (76).

The M segment encodes the two transmembrane viral spike glycoproteins, the smaller in size G_N (SBV G_N 33.4 kDa) and the bigger G_C (SBV G_C 105.6 kDa), along with a non-structural protein NSm in a single Open reading frame (ORF) (77). These three proteins are encoded as a glycoprotein precursor (GPC) polypeptide that is co-translationally processed by host proteases resulting in the three individual proteins. The GPC processing for BUNV was extensively described by Shi and colleagues (78,79). BUNV GPC contains three Signal Peptides (SPs), each located at the N-terminal end of the final product. The GPC is first co-translationally processed by means of SPs cleavage by host proteases in the Endoplasmic Reticulum (ER), generating a pre-G_N and mature NSm and G_C. The SP of NSm, which remains linked to pre-G_N after this first step, is released from it afterwards by a peptidase to generate the final mature G_N (79). It's worth mentioning that, similarly to AKV (80), among the three genomic segments the M is known to be the most susceptible to genetic variability especially due to the presence of a hypervariable region inside the 5´ G_C coding region (81,82).

Finally, the S segment encodes the SBV-N (83). This protein plays a main role in genome encapsidation and viral assembly (21). The molecular association between the nucleoprotein and the genome is usually referred as ribonucleoprotein (RNP). The ORF from SBV-N overlaps with the one from a small non-structural protein (NSs), which acts as an antagonist of the interferon (IFN) system in mammalian cells (84). Similarly to the N-terminal domain of G_C, SBV-N is a promising vaccine candidate considering the protective effect from both its cDNA and the full protein itself in mouse models (69,70).

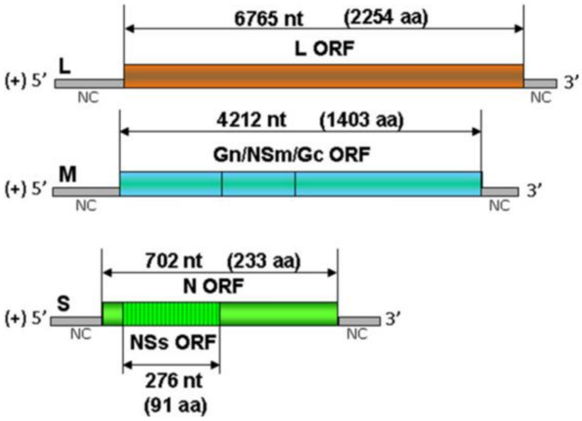

Figure 4. Schmallenberg virus genome representation. The three ssRNA Segments S, M and L ORFs flanked by the 5´ and 3´ UTRs, the different ORFs are indicated by double-sided arrows so as the corresponding number of nucleotides (nt) and amino acids (aa) shown above each ORF. Modified from Doceul *et al*. 2013.

V. <u>The SBV life cycle</u>

To invade both the arthropod vector and the mammal host cells, the glycoproteins G_C and G_N must interact with cell membrane receptors: proteins, saccharides, lipids or a combination of them (85). This interaction is highly specific, but its avidity relies on the particular identity of the viral proteins and the receptor itself. The polysaccharides of glycoproteins and glycolipids, present in the surface of many mammalian cells, are strongly polar molecules. As a primary attachment step, many viruses rely on the electrostatic interactions between their glycoproteins with these polar molecules (85,86). In 2017, the Heparan Sulfate Proteoglycan (HSPG), a glycosaminoglycan, was reported by Murakami and collaborators as a key interaction factor for cell penetration of both SBV and AKAV (87). The same finding was also shown by a CRISPR-Cas9 screen developed by Thamamongood and colleagues three years later (88). Regarding the viral glycoproteins of *Orthobunyaviruse*s as whole, it is widely accepted that G_C is the main responsible for binding to the cellular receptor and SBV is most likely no exception (89). However, deep knowledge in the cellular receptor for SBV is limited.

After internalization, *Orthobunyaviruses* go through the endocytic pathway finally reaching endosomal vescicles where the fusion of the viral and host´s membranes happens and the RNPs enter the cytosol. The complex transport from the early to the late endosome is accompanied by a proton concentration increase reported to be essential for *Orthobunyavirus* infection (89). Still, details specifically on SBV endosome trafficking are scarce and limited to reports on close related counterparts such as OROV (90). The last step of the internalization, the membrane fusion itself, is mediated by a viral fusion protein and so far, three main classes of fusion proteins have been described (91). More details in this topic are given later on. It was already reported the G_C protein of BUNV and SBV resemble a class-II fusion protein and that, apart from receptor recognition, it is also its function to carry on the membrane fusion and viral RNPs release (92). This process occurs in the late endosomes and was reported for SBV to be partially impaired by the K+ channel blocker tetraethylammonium (86). Details in G_C, membrane fusion mechanism and SBV spike architecture will be described below.

Following RNP entry, the early transcription is performed by the RdRp, which aims to produce mRNA having as template the (-) ssRNA genome. The viral polymerase relies on the cap snatching process to initiate the RNA production, as described earlier (76). Strikingly, the viral transcription happens simultaneously, and is in fact dependent, of the host cell translation machinery (93). The genome replication however, happens by using as template a full length (+) RNA known as antigenome, also produced by the RdRp but this time not being necessary any capping or priming events. Later, if enough SBV-N is produced, the genome is encapsidated forming the RNPs (21,94).

Concomitantly, the GPC, by harbouring its SPs, is co-translationally processed into the ER and the mature glycoproteins G_N and G_C are targeted to the Golgi apparatus (74), accumulate into its membrane. These glycoprotein-rich regions receive the RNPs, where finally the assembly occurs in Golgi-derived vesicles (21). In the viral life cycle of Lassa virus (LASV) (fam. *Arenaviridae*) and of Influenza, the genome packaging is described to be a tightly regulated process that ultimately allows the incorporation of all the different genome segments into the nascent virion (95). However, there is still a lot to be investigated regarding the genome packaging organization of viruses from the *Peribunyaviridae* family such as SBV. It is known that, in the mature virion, the three segments from the genome are bound to the nucleoprotein forming the RNPs with a pseudo-circular ¨panhandle¨ structure, mainly due to interactions on the complementary UTRs present in the 5’ and 3’-ends, as previously mentioned (72). Such untranslated regions have also been directly linked to genome packaging on BUNV and UUKV (96, 97).

It is worth mentioning that viruses from the *Bunyavirales* order, in comparison other (-) ssRNA viruses such as Influenza *(Articulavirales* order) and Ebola (*Mononegavirales* order), do not encode a matrix protein (MP). MPs have several functions related to the coordination of the viral assembly in the correct time and place. These proteins are able to interact with most of the key components of the viral packaging machinery such as cellular membranes, RNPs and cytoplasmic tails of glycoproteins, ultimately orchestrating the viral assembly (98). However, for the viruses belonging to the *Bunyavirales* order, the carboxy terminal (C-terminal) cytoplasmic tails of the glycoproteins, specially G_N, could play the role of matrix proteins given its size and predicted presence of domains that might have this function (99).

Recently, the RNPs packaging was investigated using SBV and RVFV (100). A combination of *in situ* hybridization and immunofluorescence techniques has demonstrated that the genome packaging is more efficient in insect cells when compared to mammals (most likely contributing to the efficiency of the viral transmission from the arthropod vector to the vertebrates). Also, progeny SBV virions produced by previously infected VERO cells result in very heterogenous populations in terms of genetic composition: virions were observed harbouring all three genome segments, different combinations of them, one segment alone or even as empty particles. Surprisingly, regarding both SBV and RVFV, only around 10% of the progeny particles contained all the genomic segments and therefore were fully infectious on their own. The authors raise the questioning whether co-infection by complementing incomplete particles might compensate for this inefficient packaging, which was already demonstrated for segmented genome plant viruses (101). It has been also pointed out that a flexible genome packaging contributes to reassortment events, indirectly favouring genetic diversity (21).

Finally, the release of the progeny virions follows the exocytic pathway, which was reported using green fluorescent protein (GFP) tagged G_C in BUNV virion model (21, 102). Maturation steps of the viral spike were also shown with BUNV and include acquiring endo-β-*N*-acetylglucosaminidase-H resistance, glycosylation steps and lateral interactions of the glycoproteins within the lipid bilayer (102). A scheme of the *Orthobunyavirus* life cycle into the host cell is given on Figure 5.

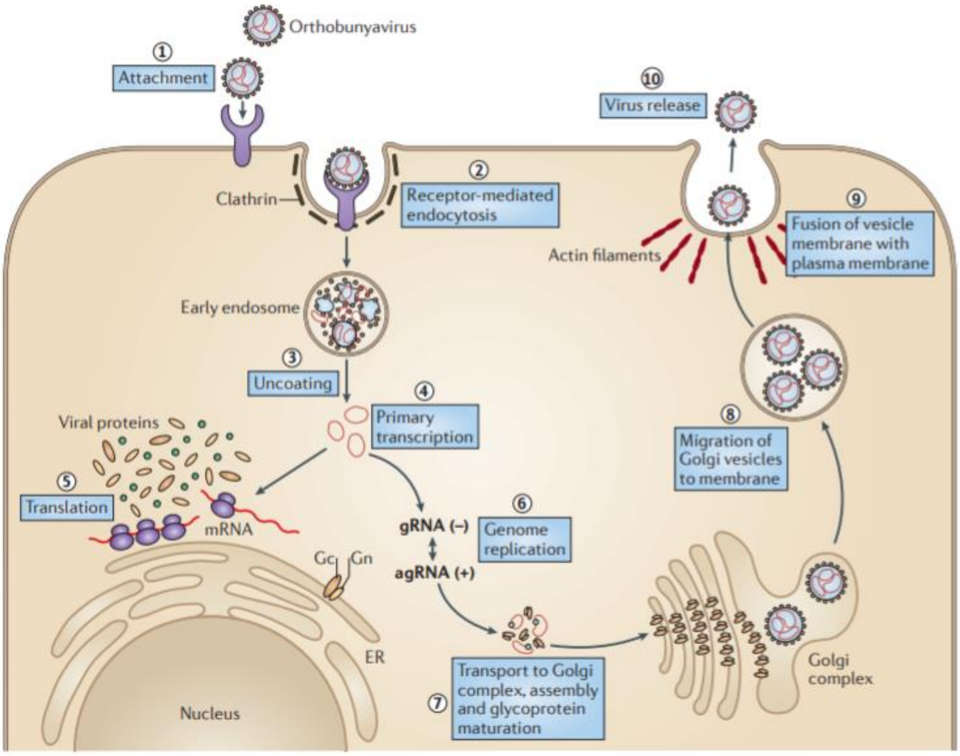

Figure 5. *Orthobunyavirus* life cycle. Different stages from the Orthobunyaviruses infection into the host cell from attachment to viral release are numbered from 1 to 10, which are described in detail in the main text. Obtained from Elliot 2014.

VI. Details on the SBV Nucleoprotein structure: Domains and oligomeric organization

The Nucleoprotein, whose molecular weight ranges between 25 and 30 kDa for *Orthobunyavirus* (233 aa residues long and 26.1 kDa specifically in SBV-N) is the most abundant protein produced during the viral infectious cycle. By encapsidating the genomic (-) ssRNA, the RNPs serve as template for the RdRps transcription and genome replication. As mentioned before, a ¨panhandle¨ structure is formed by the RNP in conjunction with the RdRps, which are packaged inside the nascent virion (96). Moreover, besides interacting with RNA, the nucleoprotein also interacts with the glycoproteins G_C and G_N, specially the G_N cytoplasmic tail, in a way that is speculated to function as a matrix protein (98,99,105,106).

Although in principle the nucleoproteins from (-) RNA viruses accomplish common functions, sharing a notable amino acid identity among viruses from the same genus, i.e. the nucleoproteins from SBV and BUNV share a 37 % identity (105), structurally they might differ (107). The SBV-N structures deposited into the Protein Data Bank (PDB) were obtained by X-ray crystallography (PDB IDs 4IDU and 41DX) and gave important insights into the nucleoprotein structural organization. The protomer from SBV-N consists of two organized domains: N-terminal (Asn19 –

Ala127) and C-terminal (Glu128 – Trp213), which are flanked in both their extremities by two highly flexible ¨arms¨ named N (Met1 – Phe18) and C-terminal (Ala214 – Ile233) arms respectively (Figure 6A). Between the N and C-terminal domains, there is a highly positively charged cleft further proven to be the RNA binding site (Figure 6B and C) (108).

SBV-N presents an oligomeric form, predominantly as a tetramer (108). This tetramer was also observed both in the SBV-N structure deposited by Ariza and colleagues (PDB ID: 3ZL9) and in the BUNV nucleoprotein (PDB ID: 3ZLA). It is worth mentioning that on this two, the oligomer structure was solved by X-ray diffraction bound to RNA (105), the same as in another SBV-N structure deposited by Dong and colleagues (PDB ID: 4JNG) (107).

There is a degree of consensus between the Ariza and Dong groups regarding the tetrameric organization of SBV-N oligomers: The N and C-terminal arms actively hold the whole structure together. The N-terminal arm hydrophobically interacts with the C-terminal edge of the RNA binding cleft from the adjacent protomer and the C-terminal arm, which contains a highly hydrophobic α-helix, buries itself inside a hydrophobic pocket from a different protomer (Figure 6D) (105,108). This configuration is also seen in the BUNV tetramer organization (105). The presence of arms that interact and mediate oligomerization on nucleoproteins, however, was not strikingly new. The nucleoprotein from RVFV, was also solved by X-ray crystallography (PDB ID: 4V9E) and presents a N-terminal arm as well, which allows oligomeric configurations to occur (109). Also, besides forming tetramers, the crystal structure of SBV-N was also shown to adopt a hexamer configuration (PDB ID:41DX) (108).

However, the tight constriction of the RNA molecule inside the tetrameric RNPs is a two-handed way. It does not allow the formation of double stranded RNA (dsRNA) and base pairing with nascent RNA chains, but at the same time also prevents the access of the RdRp for genome replication and transcription (105). For that reason, a model for a conformational change in which the whole quaternary structured molecule rotates exposing the RNA was proposed by Dong and colleagues (107). That still remains under investigation, along with the use of the SBV-N itself (70) and its corresponding cDNA (69) as immunogens in vaccine prototypes, which is one of the topics of the current doctoral thesis.

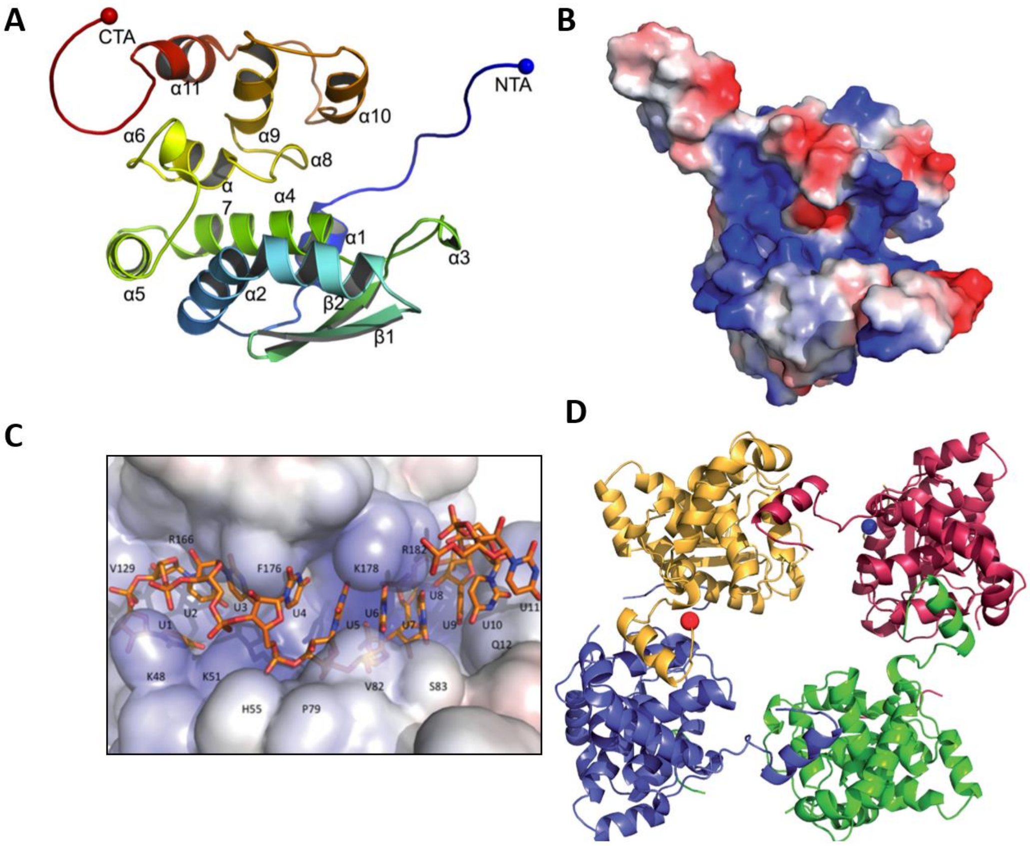

Figure 6.SBV-N structure. (A) Protomer of SBV-N with its different secondary structure sections, the N-terminal arm (NTA) is shown in blue and the C-terminal arm (CTA) in red. Obtained from Dong *et al.* 2013. **(B)** Electrostatic surface of a protomer of SBV-N, positively and negatively charged regions are depicted in blue and red, respectively. The RNA binding positively charged region is clearly found in the center of the structure. Obtained by Ariza *et al.* 2013. **(C)** RNA chain, depicted in orange sticks, shown inside SBV-N positively charged chamber, shown with an electrostatic potential in the colouring same fashion as (B), obtained by Dong *et al.* 2013. **(D)** SBV-N tetramer shown in ribbons, each monomer is shown in a different colour. Obtained by Ariza *et al.* 2013.

VII. Structural insights into SBV structure utilizing BUNV as a model

Contrary to SBV, the structure from its close related counterpart BUNV was already extensively described: its pleomorphic, matrix proteins are absent and harbour an ordered patch of glycoproteins at the top of its membranes (110). In details, the average diameter for BUNV particles is 108 nm (Figure 7A) as shown by Bowden and colleagues, that also gave details about the G_C/G_N heterodimer organization obtained by Cryo-electron tomography (Cryo-ET) and deposited it to the Electron Microscopy Data Bank (EMDB) in 2013 (EMDB ID: 2352) (110).

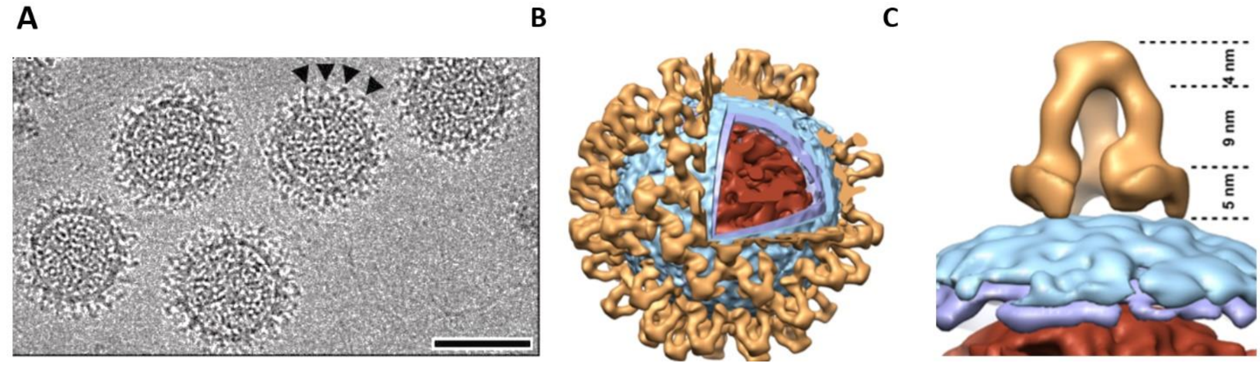

Figure 7. BUNV structure and glycoprotein spike domains. (A) Electron cryo microscopy (Cryo-EM) image of BUNV, triangles point to the glycoprotein spikes. Scale bar 100 nm. Obtained from Bowden *et al.* 2013. **(B)** Cut open model of a BUNV particle, the spike is represented in orange, outer leaflet of the lipid bilayer in blue, inner leaflet of lipid bilayer in purple and RNP corresponding densities in red. **(C)** Side view from the glycoprotein spike trimer, floor (5 nm), stalk (9 nm) and head (4 nm) regions have their sizes on the side, the colouring follows the same pattern as in B. Obtained from Bowden *et al* 2013.

The glycoprotein spike complexes from BUNV form a unique pyramidal structure that covers the entire virion surface and is subdivided into three regions: the membrane proximal floor region, composed by both G_C and G_N proteins, the membrane distal head region at the tip of the spike, which is composed solely by the N-terminal portion of G_C and a stalk region, that connects both regions and presumably is also composed by G_C (Figure 7B and C). G_N and G_C are respectively 34 and 109 kDa in size in this virus. In details, G_N is composed by a 205 aa residues N-terminal ectodomain and a long 55 aa residues C-terminal tail connected by a transmembrane domain. G_C, three times its size, harbours a considerably larger N-terminal domain of 910 aa residues, a transmembrane region and a short cytoplasmic tail (110). BUNV´s genome M segment, responsible for coding G_N and G_C, shares striking 54% sequence identity with the M segment from SBV (110). Regarding their glycoproteins, the primary sequences from BUNV and SBV GPCs have 34.29% identity. Their G_{Cs} and G_{Ns} share 35.48% and 40.07% identities, respectively (110). Recently, the structure from the N-terminal domain of SBV G_C (PDB ID: 6H3S) was well fitted inside the density from BUNV spike (92).

In details, the crystal structure from SBV G_C N-terminal half, obtained by Hellert and colleagues in 2019, shows two domains, named head (α-helical) and stalk (two β-sheet subdomains in tandem), separated by a short hinge adopting an overall V-shaped conformation (92). The protein also carries two N-linked sugars at Asn 493 and Asn 686 (110) (Figure 8A). An oligomer´s trimeric organization was initially proposed for SBV G_C and this protein has, as the authors mention, an unambiguous fit with to the BUNV EM map with a correlation coefficient reaching as high as 0.92. A trimeric configuration was experimentally obtained when G_{Cs} from BUNV, LACV and OROV structures were resolved (PDB IDs 6H3V, 6H3W, and 6H3X respectively) which might indicate a structural conservation of G_C among *Orthobunyavirus* (92).

Even though the low resolution from BUNV spike (30 Å) impairs a sequence-correlated domain assignment, it is proposed by the authors that both the G_C from SBV and BUNV adopt a trimer configuration in their N-terminal portions at the tip of the glycoprotein spikes. A trimer was, however, experimentally seen only for BUNV G_C at the present moment. Also, the membrane proximal regions for BUN, and putatively for SBV, should correspond to contacts with the smaller in size G_N (Figure 8B). Finally, SBV G_C structure was also obtained conjugated to antibodies (PDB IDs: 6H3U and 6H3T) and has demonstrated therapeutical activity when head and stalk domains were used as immunogens in small rodents (92).

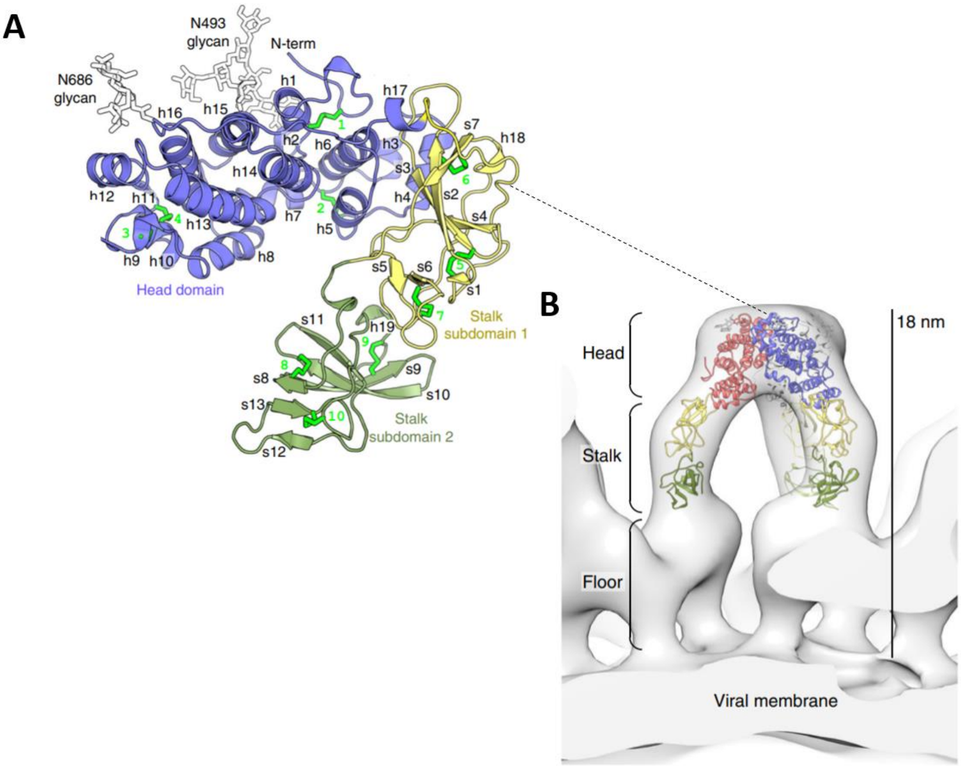

Figure 8. SBV G_C structure fitted inside the BUNV Spike. (A) G_C Head domain as obtained by X-ray Crystallography shown in dark blue and the two stalk subdomains shown in yellow and green. Sugars are shown as white sticks. Disulfide bonds are numbered sequentially and shown in bright green. Secondary structure shown as h for α-helices and s from β strands. **(B)** Side view from the Positioning of the head and stalk domains from G_C N-terminal structure within the cryo-ET map of the BUNV spike. SBV G_C protomers are proposed to form a trimer and fit inside the head of the BUNV spike. The proteins are shown with their head domains in red, dark blue and white. Retrieved from Hellert *et al.* 2019.

Hellert and colleagues also interestingly point out that by being more exposed to the host immune defenses, the N-terminal from G_C head domain along with the pyramidal architecture from the spike as a whole ¨shields¨ the critical membrane fusion motifs from the spike proteins, presumably the C-terminal part of G_C along with the N-terminal ectodomain from G_N, both present at the floor region of the tripod. Moreover, this shielding might also be a fine evolutionary optimization since the head region, and not the membrane fusion motifs, is responsible for escaping the immune pressure and consequently is more susceptible to antigenic drifts (92). This statement is in harmony with what was described by Coupeau and colleagues in 2013 that have shown a hypervariable region in G_C (81,92). However, despite the good fitting inside the BUNV spike, the structure and architecture of the SBV G_C/G_N complex remains obscure.

VIII. Glycoprotein spikes: From receptor recognition to membrane fusion

As previously mentioned SBV particle is enveloped, enclosing its RNPs inside a lipid bilayer. This lipidic membrane envelope is also present in (+) RNA viruses' families such as *Flaviviridae* and *Togaviridae*. G_C and G_N are transmembrane glycoproteins that cross the viral lipidic membrane, both encoded by the M segment of the *Peribunyaviridae* genome. These proteins are very likely to have emerged from a similar ancestor as these (+) RNA counterparts (111). The organization of the viral glycoproteins is of striking importance due to their vital role in the early stages of the viral life cycle, primarily binding to the host cells receptors, membrane fusion (as seen bellow), in many cases for viral assembly, and also for being both a tropism restriction factors and the primary target of the host immune defences, being interesting targets for drug and vaccine development (79, 92, 112).

The process of viral internalization starts with the interaction of the glycoproteins with a cellular receptor (87). A broad range of mammalian, invertebrate and even plants are infected by viruses from the *Bunyavirales* order. It is reasonable to assume that not one but many receptors and co-factors likely take part in the process of infection, some of which have already been identified (79). LACV for example has been liked to interact with DC-SIGN, a calcium dependent lectin presents at the surface of dendritic cells. DC-SIGN was also pointed out to be related with RVFV internalization (113).

SBV and AKAV in principle should not follow this route since DC-SIGN is incompatible with their tropism for not being expressed in CNS cells, which are their main site of infection in animals. HSPG however, is expressed in all cells, including neuronal. The study of Murakami and collaborators shows that this might be the preferred route for their infection, which was probed by heparinase susceptibility experiments and HSPG gene knockout cell lines usage (87). The authors, however, ask for caution and state that the 3D structure of the G_C/G_N heterodimer is required to define the HSPG or other attachment co-factors binding sites to the viral spike. Same as for the initial receptors, the endocytic route followed by *Bunyaviruses* is vast, even among the same genus. Regarding viruses from the *Orthobunyavirus* genus, Clathrin-mediated endocytosis (CME) was described for OROV (90) and LACV (114) and Clathrin and caveolin independent for AKAV (115). Still, data regarding SBV´s endocytosis specifically, is currently scarce.

In order to deliver their genomes into the cytoplasm of the host cell, viruses that possess a lipidic envelope utilize a fusion mechanism between their own membranes and the one from the host. This process is mediated by fusion proteins, which are classified according to their structural features into class I, II or III (115). Briefly, Class I fusion proteins are present into viruses such as Influenza (*Orthomyxoviridae* family*)* and Ebola (*Filoviridae* family), to name a few. Class II fusion proteins, on the other hand, are the mediators of genome release of viruses like Dengue virus (*Flaviviridae* family*),* Semliki Forest Virus (SFV) (*Togaviridae* family*)* and also *Peribunyavirdae* family members like SBV (116). Finally, Class III fusion proteins are present into viruses from the *Herpesviridae* family such as Herpes Simplex virus type 1*, Rhabdoviridae* family like Vesicular Stomatitis virus, among others (117).

The G_C from RVFV (*Phenuiviridae* family) was the first *Bunyavirales* order virus derived glycoprotein structure to be resolved back in 2013 (PDB ID: 4HJ1) (118). Similarly as the of G_C from the Puumala Virus (PUUV) (*Hantaviridae* family*)* resolved three years after (PDB ID: 5J9H) (119), it adopts a class II fusion protein architecture (120). Briefly, the structure of class II fusion proteins consists of three β-structured domains named I, II and III. Domain I is the central β sandwich with an ¨up and down¨ topology, Domain II is formed by extensive disulphide bonded loops and most importantly by the hydrophobic ¨fusion loop¨ responsible for membrane fusion. Finally, the Ig-like Domain III connects the former two to the transmembrane section of the protein by a region named the stem (91,121).

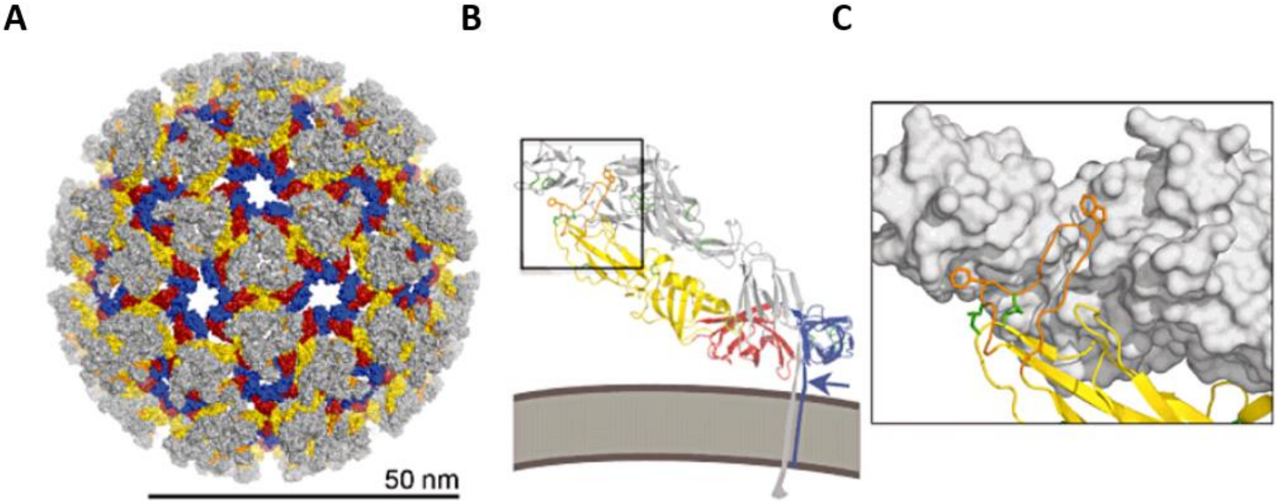

Figure 9. Regular packing of envelope proteins at the surface of infectious class II virions. (A) The icosahedral SFV particle is made of 80 trimeric spikes made of E1/E2 heterodimeric subunits. E2 is coloured grey, and E1 is coloured according to domains (red, yellow and blue for domains I, II and III, respectively, with the fusion loop in orange). **(B)** Ribbon diagram of the E2/E1 heterodimer, with E1 coloured by domains and E2 shown in grey, the membrane is shown in brown, disulphide bonds are shown in green. The blue arrow points to a cartoon drawing of the stem. **(C)** Interactions of the fusion loop within the glycoprotein shell. The unit in the foreground is displayed in ribbons, and the one in the background is shown as a grey surface. Obtained by Vaney and Rey, 2011 and adapted from Lescar *et al*. 2001.

Fusion proteins are held at a prefusion conformation, which precedes insertion of the fusion loop into the host membrane. In this conformation, the hydrophobic fusion loop is maintained unexposed by means of protein-protein interactions between the spike proteins (120). An illustration of the basic structure of a class II fusion protein in the pre-fusion state using the E1/E2 glycoprotein heterodimer from SFV (*Togaviridae* family*)* is exemplified in Figure 9.

A scheme for membrane fusion mediated by a class II fusion protein using SFV as a model is shown in Figure 10. Briefly, an initial ¨priming¨ event exposes the hydrophobic internal fusion loop which culminates in its insertion at the host membrane favouring trimerization of the viral spikes (116). The membrane fusion is triggered by the endosomal low pH for SFV (121) and for *Orthobunyaviruses* like SBV as mentioned previously (21). A massive conformation rearrangement moves the stem region and the domain III of the fusion protein towards the inserted loop, causing distortions both at the host and viral membranes leading to the hemifusion state (mixing of the outer leaflets of both bilayers).

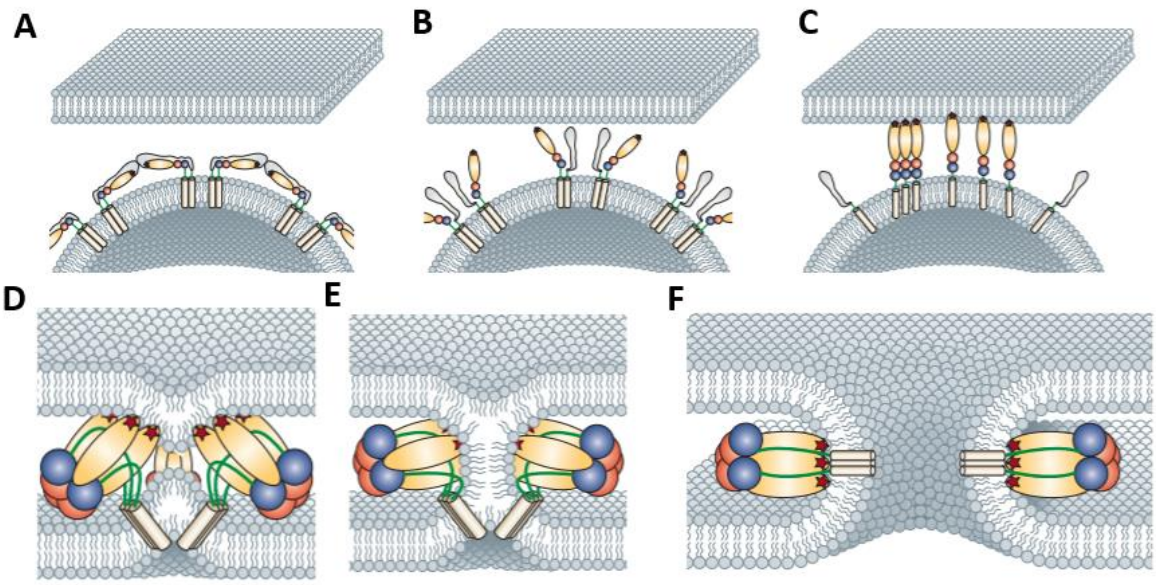

Figure 10. Scheme from class II membrane fusion obtained from SFV. The fusion protein has its Domains I, II and III coloured in red, yellow and blue respectively, the stem region is shown in green. **(A)** Prefusion state in which the fusion loop inaccessible. **(B)** Priming event. **(C)** Fusion loop insertion into the host membrane **(D)** Distortion of the viral and host membranes. **(E)** Hemifusion state. **(F)** Fusion pore formation. Obtained from Kielian and Rey, 2005.

Afterwards, a final stable conformation is achieved by the formation of the fusion pore (116). Although the fusion of two lipid bilayers is thermodynamically favourable, a kinetic barrier is raised by a repulsive ¨hydration force¨ when both membranes are no more than 20 Å apart. The job of the fusion loop in creating the hemifusion state is precisely the way that enveloped viruses found to overcome this energetic barrier (91).

Chapter 2:

HYPOTHESIS AND OBJECTIVES

Hypothesis

Based on the previous findings regarding the protection provided by the full SBV-N in immunized small rodents following SBV challenge, the hypothesis behind the current vaccinology study is that the identification of smaller SBV-N fragments as immunogens for multimeric subunit particle vaccine technology is possible.

Concomitantly, the structural characterization of viruses and surface viral proteins represents a powerful means to understand viral assembly and antibody neutralization mechanisms. Because this information is scarce on SBV virions, the present work aims at laying the basis for a deeper structural characterization of the SBV whole virion and spike complexes. The latter is essential for virus entry and antibody recognition and neutralization.

Objectives

I. Epitope mapping of Schmallenberg virus nucleoprotein (SBV-N)

a. Investigate the MHC-I epitopes responsible for the immunogenicity and protection provided by SBV-N against SBV infection.
b. Identification of SBV-N fragments that harbour the above-mentioned properties as subunit-vaccine candidates.

II. Structural investigation of SBV particles

a. Optimization of protocols for propagation and purification of SBV virus
b. Initial morphological characterization of the SBV virion and glycoprotein spikes by single particle analyses and cryo-electron tomography.

Chapter 3:

MATERIALS AND METHODS

Part 1 – SBV-N Epitope mapping and vaccine prototype development

I. Design of peptides used for the investigation of the MHC-I epitopes of SBV-N

The putative Major Histocompatibility Complex class I (MHC-I) epitopes from SBV-N were *in silico* investigated using the NetMHCpan 4.0 server (122). This server is, in principle, able to find hotspot hits on possible binders to the cattle MHC-I system, made up by the bovine leukocyte antigens (BoLA). NetMHCpan 4.0 was fed with the FASTA sequence of the SBV-N protein (Uniprot ref. H2AM13). Seven strong binders were identified in the SBV-N sequence (P1-P7; Table 2), mapped out the structure (PDB ID:3ZL9) (105) (Figure 11) and tested as stimuli for splenocytes re-stimulation, as described in the section V from the Materials and Methods.

Peptide	Sequence	SBV-N location (aa)
P1	AQPSVDLTF	58-66
P2	SNPVPDNAITL	83-91
P3	ASAQIVMPL	118-126
P4	WADGYTMYL	134-142
P5	FAPGAEMFL	144-152
P6	AAFNSVGQL	203-211
P7	FSPAARTFL	218-226

Table 2. Oligopeptide sequences used as possible MHC-I epitopes followed by their aminoacidic location in the SBV-N primary structure (Uniprot ref. H2AM13).

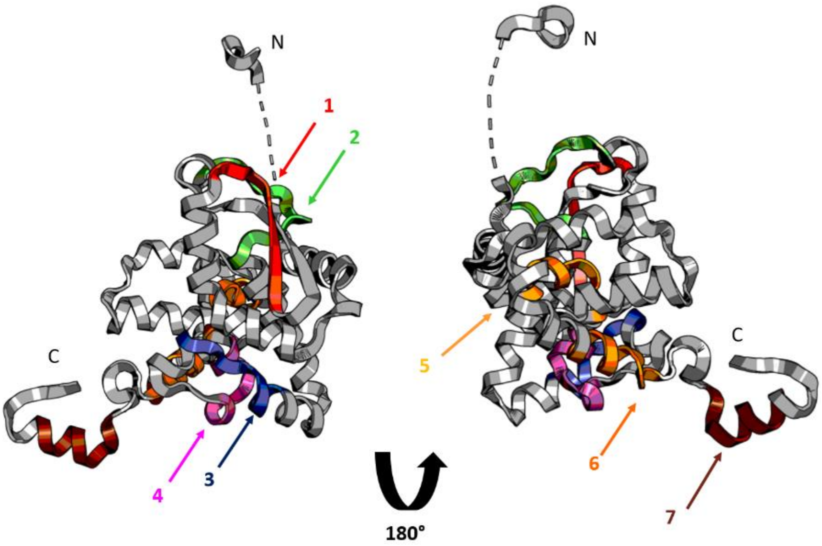

Figure 11. Schematic representation of peptides P1-P7 design. Cartoon representation from SBV-N structure (PDB:3ZL9) (105) with the corresponding locations from the different peptides (P1–P7) obtained with the NetMHCpan 4.0 server; N and C represent N- and C-terminal extremities from the protein, respectively.

Further in the project, nine new peptides were designed. Six peptides covered the full N-terminal extremity of the SBV-N (Met1-Ala58) (P. I - P. VI) with 3 aa overlaps amongst themselves. The 3 remaining peptides derive from the interface between Ala58 and Thr133 (P. VII - P. IX) (Table 3, Figure 12).

Peptide	Sequence	SBV-N location (aa)
P. I	MSSQFIFIEDVP	1-12
P. II	DVPQRNAATFNP	10-21
P. III	FNPEVGYVAFIG	19-30
P. IV	FIGKYGQQLNFG	28-39
P. V	NFGVARVFFLNQ	37-48
P. VI	LNQKKAKMVLHKTA	46-58
P. VII	SNPVPDNAITLH	83-94
P. VIII	AQPSVDLTFGGV	59-69
P. IX	ASAQIVMPLAEV	118-129

Table 3. Depiction of peptides utilized further in the project as possible MHC-I epitopes followed by their aminoacidic location in the SBV-N primary structure (Uniprot ref. H2AM13).

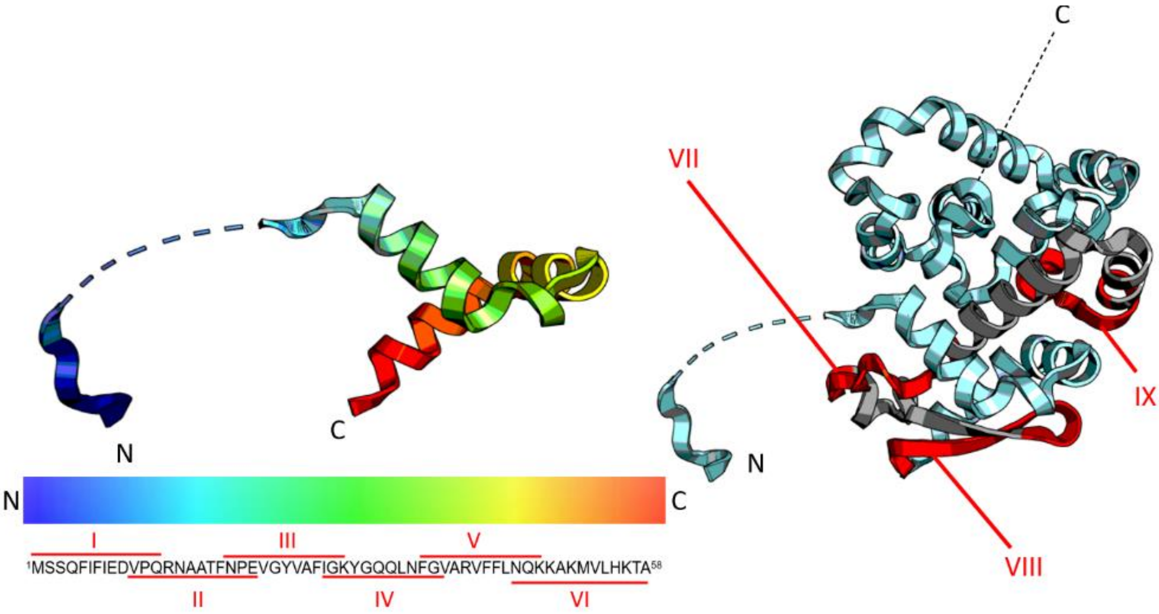

Figure 12. Schematic representation of peptides P. I – P. IX design. **Left, top** cartoon representation from the first 58 aa from SBV-N, coloured in rainbow. N and C represent N- and C-terminal extremities, respectively. **Left, bottom** corresponding FASTA sequences from truncated peptides (P. I - P. VI). **Right** SBV-N N-terminal half corresponding section with the N-terminal extremity region coloured in cyan and the aa 59-133 interface coloured in grey. Peptides P. VII - P. IX regions are coloured in red. N and C represent N- and C-terminal extremities, respectively. Dashed lines in the cartoons represent a non-structured loop at the deposited structure (PDB ID:3ZL9) (105).

All peptides described previously were synthetized lyophilized (Thermo Scientific), dissolved into Dimethyl Sulfoxide (DMSO) following the manufacturer instructions, adjusted to a concentration of 1 mg/ml and stored at -20°C until use.

II. Protein engineering and construct design

Following the efficacy of SBV-N in combination with Saponin as a vaccine candidate against SBV and its ability to be readily expressed in *E. coli* (70), different constructs from SBV-N were designed. They were bacterially expressed to help elucidating the MHC-I presented epitope(s) responsible for the cytotoxic T lymphocyte (TCD8+) cell mediated immune response observed (70). Moreover, the SBV-N constructs were afterwards tested in different immunological assays, as further described.

The three-dimensional SBV-N structure (PDB ID: 3ZL9) (105) was loaded and analysed into PyMOL (123) and different constructs were engineered as follows: Two constructs harbouring the N-terminal (Met1-Thr133) and C-terminal[a] (Trp134–Ile233) portions of SBV-N were designed to be cloned into bacterial expression vectors with different features: A C-terminal His_6-tag (pOPINE) (Figure 13A), a N-terminal His_6-tag + Glutathione S-transferase (GST) fusion (pOPINJ), a N-terminal His_6-tag + Maltose Binding protein (MBP) fusion (pOPINM) and a N-terminal His_6-tag pOPINF (124).

Briefly, the first construct was designed harbouring the entire N-terminal domain of SBV-N. This portion of the protein starts at a highly flexible N-terminal arm extending until Phe18 and is followed by 5 α-helices (α1 to α5) and 2 antiparallel β-strands, finishing at the Ala127 residue which marks the end of α5 (106). In the present study, the construct named N-terminal extends six aa residues beyond α5 to prevent the disruption of the secondary structure and has as its C-terminal residue the Thr133. Moreover, α5 (Val123 – Gly131) contains key residues such as Met124 and Leu126, both responsible for the dimer formation on the oligomerization of the protein. This residues also interact with the N-terminal arm from a different protomer, aside from being also part of dimer:dimer interactions with α1 and α4 (106). C-terminal[a] was designed starting immediately after the last residue of the previously mentioned N-terminal construct.

Later during the thesis, both N-terminal and C-terminal constructs, along with new ones within the N-terminal portion of SBV-N were designed to be cloned into the pGEX-4-T1 expression vector harbouring a GST N-terminal tag (125) (Figure 13B) as follows: N-terminal (Met1 – Thr 133), Construct 2 (C2; Met1 – Val112), Construct 3 (C3; Met1 – Ser83) and construct 4 (C4; Met1 – Ala58).

All the above-mentioned smaller constructs of the SBV-N N-term domain were designed with boundaries so that folded regions were not compromised: (*i*) C2 not containing helix α5; (*ii*) C3 not containing helix α4; and (*iii*) the N-terminal extremity C4. harbouring helices α1 and α2 and not containing the antiparallel β strands. An additional construct (C-terminal^{b}; Gln59-Ile233) was designed starting immediately after the last residue of the previously mentioned C4 construct.

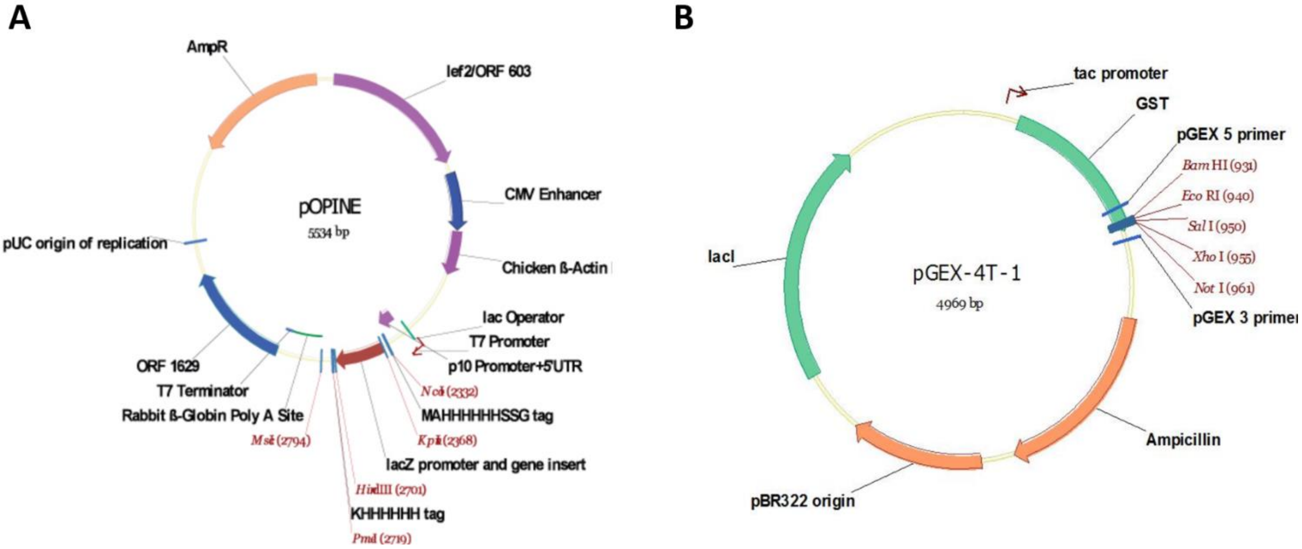

Figure 13. Expression vectors used in the present work for the SBV-N derived constructs. (A) pOPINE vector features a His$_{6}$-tag downstream from the cloning site. **(B)** pGEX-4T-1 vector harbours a GST fusion corresponding sequence upstream from the cloning site. Both vectors confer Ampicilin (Amp) resistance and harbour T7 (pOPINE) and a *tac* (pGEX-4-T1) promoters for expression.

III. Molecular cloning

Primers were designed and synthesized in order to amplify the SBV-N derived constructs corresponding DNA sequences (Table 4). Briefly, for amplifying the sequences to be cloned into pOPINJ, F and M by PCR (Polymerase Chain Reaction) the forward and reverse primers had to be 5' flanked by the sequences AAGTTCTGTTTCAGGGCCCG and ATGGTCTAGAAAGCTTTA respectively. Sequences to be cloned into pOPINE were flanked with AGGAGATATACC and GTGATGGTGATGTTT at their forward and reverse oligonucleotides, respectively. Sequences to be cloned into pGEX-4-T1 had, at their corresponding primers sequences for the restriction sites from the enzymes *Eco*RI and *Not*I at their forward and reverse oligonucleotides, respectively. Apart from the *Not*I site the reverse oligonucleotide also coded for an additional His$_6$-tag to be placed at the C-terminal of the proteins. Finally, both primers for pGEX-4-T1 cloning were also flaked by an ATATA sequence to improve restriction cleavage at their 5´ ends.

PCRs were carried out with the corresponding pair of oligonucleotides, Pyrobest™ DNA Polymerase (TAKARA™) and dNTP mix solution (TAKARA™) using a MJ Mini thermal cycler (Bio Rad). The annealing temperatures ranged from 52°C to 60°C depending on the sequence amplified. The cDNA from SBV-N used as template was obtained from the SBV-N gene previously cloned within the pUC57 or pET-28a-SUMO vectors (70). Integrity of the resulting amplicons was checked in 2% Agarose electrophoresis.

Sequence		Construct	Vector
AGGAGATATACCATGATGTCAAGCCAATTCATTTTTGAA	*F*	N-term, C2, C3, C4	pOPINE
GTGATGGTGATGTTTGGTGCATCCCTTAACCTCAGCAAG	*R*	N-terminal	
GTGATGGTGATGTTTGACACTAGCCTTGCATGTATC	*R*	C2	
GTGATGGTGATGTTTTGAGACATATTGGGGAAAATG	*R*	C3	
GTGATGGTGATGTTTTGCCGTCTTATGTAGGACCAT	*R*	C4	
AAGTTCTGTTTCAGGGCCCGATGATGTCAAGCCAATTCATTTTTGAA	*F*	N-term	pOPINJ, pOPINM, pOPINF
ATGGTCTAGAAAGCTTTAGGTGCATCCCTTAACCTCAGCAAG	*R*		
AAGTTCTGTTTCAGGGCCCGATGACCTGGGCCGATGGTTATACAATG	*F*	C-terminal[a]	
ATGGTCTAGAAAGCTTTAGATGTTGATACCGAATTGCTGCAA	*R*		
ATATA**GAATTC**ATGTCAAGCCAATTCATTTTTGA ATATA**GCGGCCGC**AAGTGATGGTGATGGTGATG	*F* *R*	N-term, C2, C3, C4	pGEX-4-T1
AGGAGATATACCATGACCTGGGCCGATGGTTATACAATG GTGATGGTGATGTTTGATGTTGATACCGAATTGCTGCAA	*F* *R*	C-terminal[a]	pOPINE
ATATA**GAATTC**CAACCAAGTGTCGATCTTACTTTT ATATA**GCGGCCGC**AAGATGTTGATACCGAATTGCTG	*F* *R*	C-terminal[b]	pGEX-4-T1

Table 4. Oligonucleotide sequences used in the present work to uplift the corresponding constructs from SBV-N, bold sequences represent either *Eco*RI or *Not*I restriction sites. F and R denote Forward and Reverse primers used in the PCR reactions, respectively. The boundaries of each construct and details in the expression vectors are both given in the main text.

The corresponding vectors were linearized either with *Kpn*I and *Hind*III (pOPINJ,F and M), *Age*I and *Kpn*I (pOPINE) or *Eco*RI and *Not*I (pGEX-4-T1) (Thermo Scientific) after passing through 1% Agarose gel electrophoresis and being gel extracted with Nucleospin gel clean-up kit (Macherey Nagel). Linearized pOPINJ,F,M and E received their amplicons following the In-Fusion® HD cloning kit (TAKARA™) that works based on the annealing of complementary ends of the insert and linearized vector. Incubation of vectors, inserts and 5X In-Fusion HD enzyme premix was carried out at 50°C for 15 mins as recommended by the manufactures.

On the other hand, classical restriction cloning was utilized to insert the corresponding amplicons at the pGEX-4-T1 vector (126). Briefly, both PCR products and vector were linearized with *Eco*RI/*Not*I overnight at 37°C. Next, samples were purified with a Nucleospin PCR clean-up kit (Macherey-Nagel) and ligated with a quick ligation kit™ (NEB®) for 5 minutes at 25°C.

All ligation mixtures were used to heat shock transform competent DH5α *E. coli*. The bacterial cells were thawed on ice 30 minutes following addition of 3 µL of ligation mixture and another 30 minutes incubation on ice. Cells were then incubated at 42°C for 45 seconds and immediately placed on ice for 3 minutes. Next, 500 µL of Luria-Bertani (LB) media was added and transformed cells were incubated at 180 rpm agitation at 37°C for 40 minutes. Finally, cells were spun at 5000 g using a table top centrifuge and the full mixture was plated into LB agar plates with 50 µg/mL of Amp, left overnight at 37°C. Positive colonies were picked to grow 5 mL inoculums in LB media with 50 µg/mL Amp overnight at 37°C with 200 rpm agitation. Plasmids were purified with a GeneJET plasmid miniprep kit (Thermo Scientific) and nanodrop quantified. The clones were sent for Sanger sequencing (STAB VIDA^{TM}, Caparica, Portugal) to check for correctness of the SBV-N derived sequences *per se* (Uniprot ID:H2AM13) and if their corresponding translation codons were correctly in frames with the different fusion proteins and/or tags present at the expression vectors.

IV. Protein expression and purification

SBV-N cDNA was initially inserted into the expression vector pET-28a-SUMO (previously pET-28-SUMO3-GFP from which the GFP coding sequence was swapped with the SBV-N cDNA obtained from the Protein Expression Facility at the European Molecular Biology Laboratory) (70). This vector has the recombinant protein expression regulated by the T7 promoter (same as pOPINE). Along with coding for SBV-N, this vector has a small ubiquitin-like modifier (SUMO) N-terminal tag to improve solubility and a C-terminal His_6-tag (127). The former tag can be cleaved by the use of SUMO-specific proteases (128). In the present work Sentrin-specific-protease-2 (SENP2) was used. The vector also codes for Kanamycin (Kan) resistance (Figure 14).

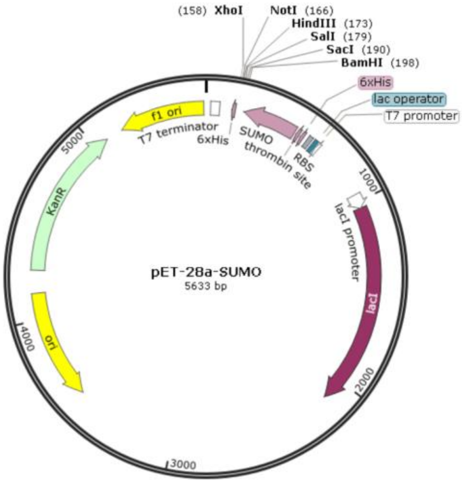

Figure 14. Expression vector for SBV-N The sequence corresponding to the protein to be expressed is placed 3´ of the solubility increaser SUMO tag. The Expression is modulated by a T7 promoter.

E. coli was used for heterologous production of all the proteins. Specifically, the BL21 (D3) strain was utilized, which is both deficient in *lon* and *ompT* proteases and contains the phage T7 RNA polymerase gene linked to an isopropyl β-d-1-thiogalactopyranoside (IPTG) inducible promoter. The T7 RNA polymerase synthesizes RNA about five times faster than the original E. *coli* RNA polymerase and is governed by the lacUV5 promoter (P_{lacUV5}), one of the many promoters constructed to date from a lac-derived regulatory element (129,130). The induction with the lactose analogue IPTG allows the production of T7 RNA polymerase that can then initiate the RNAm production by means of the T7 (pOPINE, pET) or *tac* (pGEX-4-T1) promoters located 5´. The *tac* is a hybrid version of the lacUV5 and *trp* promoters which ultimately allows a more robust RNAm production (131).

BL21 (DE3) cells were heat shock transformed with the corresponding plasmids as described previously and plated into 50 μg/mL Amp (pOPINM, pOPINJ, pOPINF, pOPINE, pGEX-4-T1) or Kan (pET-28-SUMO) LB-agar plates overnight. Inoculums were seeded overnight with the same concentration of antibiotic and positive colonies were scaled-up to 2L LB media culture at a 1:100 dilution ratio. Cells were left growing with 200 rpm agitation and 37°C until the optical density (OD) of the media reached values ranging from 0.6 to 0.8, corresponding to the exponential bacterial growth period. The cultures were then induced for protein production with 1 mM IPTG for 16 h at 18°C and same agitation fashion. Afterwards, cells were lysed using a French-press (Constant Cell Disruption Systems, UK) at 4°C for the obtention of the recombinant proteins following different purification procedures, as follows:

A) SBV-N purification (pET-28-SUMO3)

Clarified cell lysate in non-denaturing and non-reducing conditions [50 mM Tris-HCl 300 mM NaCl pH 7.0 with EDTA-free protease inhibitor cocktail] was incubated with Ni conjugated chelating Sepharose fast flow beads (Cytiva) in batch mode at 4°C for 2h. The His_6-tag present at the C-terminal of the SUMO-SBV-N construct allows the binding to Ni to occur. Then, protein-bound resin was washed and eluted with the same buffer described above supplemented with 200 mM and 500 mM imidazole (Sigma-Aldrich), respectively. Eluted fractions were concentrated to 0.5 mL and buffer exchanged to 1X Phosphate buffer saline (PBS) using 30 kDa cut-off concentrators (Sartorius) and further size-exclusion chromatography (SEC) purified using a PBS 1X equilibrated Superdex 200 Increase 10/300 column (GE Healthcare). The SBV-N corresponding eluted fractions, assessed by Sodium dodecyl-sulfate polyacrylamide gel electrophoresis (SDS-PAGE) electrophoresis and confirmed by mass spectroscopy (MS) peptide fingerprinting, were left incubating with SENP2 to cleave the SUMO tag overnight. The proteolytic products were run into the above SEC columns in the same conditions allowing the obtention of SBV-N alone, as confirmed by MS peptide fingerprinting.

B) N-terminal and C-terminal[a] constructs purifications (pOPINE)

Since the proteins were obtained as inclusion bodies, cell lysate pellets were washed six times with 50 mM Tris-HCl at pH 8.0, 100 mM NaCl, 5% Triton X-100 and once in the same conditions without any detergent. Next, the inclusion bodies were maintained under agitation in denaturing conditions [50 mM Tris, 100 mM NaCl, 5M Guanidine Hydrochloride, 4 mM Dithiothreitol (DTT)] at 4°C. The unfolded proteins were incubated with Ni conjugated beads in batch mode at 4°C and eluted with 1X PBS 500 mM imidazole. The proteins were then buffer exchanged to 1X PBS. The presence of the target proteins was evaluated by SDS-PAGE electrophoresis and confirmed by MS peptide fingerprinting.

C) pGEX-4-T1 cloned constructs purification

Clarified cell lysates in non-denaturing and non-reducing conditions [50 mM Tris-HCl at pH 8.0, 150 Mm NaCl] were loaded into GSTrap™ HP columns (Cytiva) at a low flow and eluted with the same buffer supplemented with 20 mM reduced L-glutathione (Merck). The proteins were further buffer exchanged to PBS and SEC purified being loaded into a Superdex 200 Increase 10/300 column (GE Healthcare). The corresponding fractions were evaluated by SDS-PAGE and confirmed by MS peptide fingerprinting. Additionally, attempts were made to obtain the constructs without the GST tag as follows. The GST chimeric proteins were incubated with Thrombin overnight and diluted into denaturing conditions [50 mM Tris at pH 7.0, 200 mM NaCl, 5 M Guanidine Hydrochloride] after protein precipitation. Afterwards, the unfolded probes were incubated with Ni conjugated beads, eluted with the same buffer supplemented with 500 mM Imidazole and, following SDS-PAGE evaluation and Matrix-assisted laser desorption/ionization time-of-flight mass spectroscopy (MALDI-TOF MS) confirmation, buffer exchanged to PBS 1X.

V. Evaluation of the TCD8+ stimulation with peptides following immunizations of C57BL/6 Mice

Six C57 black 6 (C57BL/6) mice were randomly divided into three groups of two and immunized at CIC bioGUNE (Derio, Spain) as follows: (1) 50 µg SBV-N + 14 µg of Quil-A Saponin (InvivoGen); (2) 50 µg untagged N-teminal + 14 µg of Quil-A Saponin; (3) PBS + 14 µg of Quil-A Saponin. Two immunizations were given subcutaneously two weeks apart. All injected solutions were made in PBS. All mice from both immunization rounds were sacrificed by cervical dislocation a week after the final vaccination. The spleens derived from the mice previously described were harvested and the splenocytes were isolated and seeded into TexMACS^{TM} medium (Miltenyi Biotec) at $5x10^6$ cells/ml on Flat-bottom 48-well plates (ThermoFisher). Positive controls were stimulated with 4 µg/ml of Concanavalin A (ConA) (Sigma Aldrich). The cells were stimulated with SBV-N, untagged N-term and peptides P1-P7 (Table 2). All stimuli were incubated at 10 µg/ml for 72 hours at 37°C with 5% CO_2. Cell surface markers of re-stimulated splenocytes were then stained with labelled antibodies (Miltenyi Biotec) for CD8a (FITC, Cat# 130-118-329), and CD107a (APC, Cat# 130-111-505) to allow distinct cell populations detection by Fluorescence-activated cell sorting (FACs). Data were acquired using a FACScalibur CANTO II (BD, Bioscience, USA) and analyzed using the FlowJo 10.8.1. software.

VI. Evaluation of the TCD8+ stimulation following immunizations of C57BL/6 Mice with the SBV-N constructs

Twelve C57BL/6 mice were randomly divided into four groups of three and immunized as follows: (1) 50 µg SBV-N + 14 µg of Quil-A Saponin; (2) 50 µg N-terminal fused to GST + 14 µg of Quil-A Saponin; (3) 50 µg GST + 14 µg of Quil-A Saponin; (4) PBS + 14 µg of Quil-A Saponin. The immunization scheme, so as the sacrifice and the splenocytes harvesting and plating proceeded in the fashion as described in the previous section. Now, the cells were stimulated with SBV-N, N-term (this time GST tagged), the GST-fused C2-4 constructs and GST alone.

All proteinaceous stimuli were incubated with the splenocytes at 10 µg/ml for 72 hours at 37°C with 5% CO_2. Cell surface markers of re-stimulated splenocytes were then stained with labelled antibodies (Miltenyi Biotec) for CD8a (FITC, Cat# 130-118-329) and CD107a (APC, Cat# 130-111-505) to allow distinct cell populations detection by FACs. Data were acquired using a FACScalibur CANTO II (BD, Bioscience, USA) and analyzed using the FlowJo 10.8.1. software. Additionally, the IFN-γ of the C57BL/6 mice derived re-stimulated splenocytes supernatants was measured using the Mouse IFN-γ enzyme-linked immunosorbent assay (ELISA) Set (RUO) kit following the manufacturer's instructions (BD OptEIA, Cat: 555138).

VII. Immunizations with SBV-N derived protein fragments and viral challenge of IFNAR$^{-/-}$ mice

To demonstrate the efficacy of the selected SBV-N short constructs against a SBV infection in a mouse model, experiments were performed at the Animal Health Research Centre (CISA-INIA/CSIC, Valdeolmos, Madrid). Four groups of A129 knockout for type I IFN receptors (IFNAR$^{-/-}$) mice (B & K Universal Ltd, UK) with 7 animals per group were immunized as described for the C57BL/6 mice previously. The (1-4) groups were as follows: (1) 50 µg SBV-N + 14 µg of Quil-A Saponin; (2) 50 µg of N-term fused to GST+ 14 µg of Quil-A Saponin; (3) 50 µg of C4 fused to GST + 14 µg of Quil-A Saponin; (4) 50 µg GST + 14 µg of Quil-A Saponin. Control groups (5) and (6) with 5 and 4 animals, respectively, were not immunized. Two weeks after the second vaccination, all mice from groups (1) to (5) were challenged with an intraperitoneal dose of 2×10^6 TCID50 SBV (strain BH619/12) previously passaged one time on Vero E6 cells and resuspended in 200 µl of Dulbecco's modified Eagle's medium (DMEM). The control group (6) was not challenged with the virus.

All animals were weighted from the first day post infection (dpi) onwards, closely monitored for the presence or absence of clinical signs of infection for 14 days and the weight averages were properly plotted. A scoring system defining the animals as ¨healthy¨ or ¨sick¨ was established, being the ‘sick’ animals those presenting at least one identifiable clinical sign *e.g.,* hunched back, ataxia, conjunctivitis etc. Animals that were found dead or euthanized upon exhibiting severe signs of morbidity before the 14th dpi did not enter in the calculation of the medians of body weights. The mice were sacrificed by cervical dislocation including those reaching the 14 dpi.

VIII. Detection and quantification of viraemia by RT-qPCR

During the IFNAR$^{-/-}$ mice SBV viral challenge, 75 µl of blood were collected at 3, 6 and 10 dpi and diluted 1:1 in PBS. RNA was extracted using the Speedtools Viral RNA extraction kit (Biotools, Spain) according to the manufacturer’s instructions, and eluted in 50 µl of RNAse free water. The presence of SBV RNA was detected using the SBV dtec-RT-qPCR kit (Genetic PCR Solutions, Elche, Spain) using 5 µl of the eluted RNA samples. RT-qPCRs were performed in an Agilent 3005 P RT-PCR system, using the FAM channel for quantification. The thermal profile used was of 50°C for 10 min, 95°C for 60 s followed by 40 cycles of 95°C for 10 s and 60°C for 60 s. Cq (Quantification cycle) values were afterward plotted in terms of viral RNA concentration using a standard curve provided by the manufacturer.

IX. ELISA for the detection of IFN-γ secretion from challenged IFNAR$^{-/-}$ mice derived splenocytes

The IFNAR$^{-/-}$ mice spleens were immediately collected after sacrifice. The splenocytes were washed twice with RPMI media (Biowest) supplemented with 10% foetal bovine serum (FBS) and 50 µM β-Mercaptoethanol. The erythroblasts were lysed for 5 mins with RBC lysis buffer (BioLegend). The cells were resuspended in RPMI, adjusted to a concentration of 2x10^{6} and added to 96-well plates (Costar) previously seeded with 10 µg/ml of N-term. 4 µg/ml ConA and RPMI 10% FBS 1% DMSO were used as controls. The cells were incubated at 37°C and 5% CO_2 for 72 h. Additionally, the supernatants from the re-stimulated IFNAR$^{-/-}$ splenocytes were then used to quantify secreted IFN-γ by ELISA. The stimulation conditions used were the same as described above (10 µg/ml) in this case the stimuli were SBV-N and N-term. Briefly, 96-well High plates

(Costar) were previously coated with 2 µg/ml anti-IFN-γ capture Ab AG-18/RA-6A2 (BD Pharmingen). After 1 h incubation at 37°C, the wells were washed twice with PBS 0.05% Tween-20 and blocked with blocking buffer [PBS 0.05% Tween-20 0.1% Bovine Serum Albumin (BSA) for 1 h at 37°C]. 50 µl of re-stimulated splenocytes derived supernatants at 1:10 dilution in blocking buffer were added to each well and incubated for 1 h at 37°C. The plates were washed three times with PBS 0.05% Tween and incubated with 1 mg/ml of anti-IFN-γ biotinylated mAb R46A2 (BD Pharmingen) for 1 h at 37°C. Plates were washed three times and 50 µl of peroxidase labelled streptavidin at a 1:500 dilution in PBS was added to each well, incubated at 37°C for 1 h. After five washing cycles, TMB substrate (Sigma-Aldrich) was added for 10 min, followed by addition of 0.5M sulfuric acid to stop the reactions. ODs were measured at a spectrophotometer as duplicates at 450 nm.

X. Investigation of IFN-γ secretion from challenged IFNAR$^{-/-}$ mice derived splenocytes re-stimulated with peptides

The splenocytes derived from the SBV challenged IFNAR$^{-/-}$ mice served to evaluate the ability from the peptides P. I – P. IX (Table 3) in re-stimulating cell derived immunity, as shown by secretion of IFN-γ upon re-stimulation of splenocytes. The spleens harvesting and plating methodologies were the same as stated previously. 4 µg/ml ConA and RPMI 10% FBS 1% DMSO were again used as controls. The cells were re-stimulated with peptides P. I – P. IX properly adjusted to a concentration of 10 µg/ml and left incubating for 72h at 37°C and 5% CO_2. The further steps regarding the IFN-γ detection ELISA were also the same as stated in the previous section, having as a final measurement the lecture of the ODs as duplicates at 450 nm.

XI. Statistical analyses

Statistical analyses were carried out with GraphPad PRISM version 8.4.2. The sample sizes of both C57BL/6 and IFNAR$^{-/-}$ mice groups were designed following the three Rs principle in animal experimentation (Replacement, Reduction and Refinement) (132). One-way analysis of variance (ANOVA) was used to assess whether there were any statistically significant differences between the resulting means of the experiments when more than two groups were analysed simultaneously.

XII. Phylogenetic analyses

The aminoacidic FASTA sequences of the corresponding constructs were obtained from SBV-N (Uniprot ref. H2AM13) and subjected to a BLASTp in order to find similar sequences utilizing a BLOSUM62 scoring matrix (133). Multisequence alignments were carried out in ClustalW (134). Further, the alignment were complemented with the SBV-N secondary structure derived from PDB ID:3ZL9 using Esprit 3.0 (105,135). Phylogenetic trees were built utilizing a maximum-likelihood method with 500 bootstrap iterations utilizing the software MEGA (136).

Part 2 –SBV Structural studies

I. SBV particles propagation and purification

For virus propagation, Baby Hamster Kidney (BHK) cells were maintained in DMEM with 5% FBS incubated at 37°C with 5% CO_2. 80% confluency BHK cell layers growing on cell culture roller bottles (Greiner Bio-One, 2152 cm^2 surface area) were infected with SBV (strain BH80/11-4). Viable cells were counted with the assistance of Trypan blue 0.4% stain (Invitrogen) and a cell counter Countess II (Invitrogen) in order to establish the correct Multiplicity of infection (MOI). The cells were seeded with SBV in 0% FBS DMEM at slow agitation for 3 h following addition of 5% FBS DMEM in order to raise the volumes and the percentage of FBS to 2%. The viral infection proceeded for 72 h.

Different SBV purification protocols were devised, they are named hereafter Purification I-V. The following purification steps consisted in separating cell organelles and both cellular and extracellular biological macromolecules from the virions, which can be achieved since these particles have different buoyant densities (g/mL) (ρ) (137) (Figure 15). BUNV particles were also reported to be purified in this fashion (138). As a first step, the supernatant containing secreted SBV virions is collected and clarified by centrifugation at 3.700g for 1h.

For *Purification I*, the virus was propagated by $3x10^8$ BHK cells (9 roller bottles) infected with a MOI of 0.01 (139). The viral particles were concentrated into 0.5 mL 30% Iodixanol solution cushions (60% Iodixanol OptiPrep™ Sigma-Aldrich + NTE buffer diluent 240 mM NaCl, 2 mM EDTA, 40 mM Tris-HCl at pH 8.0, diluted 1:1) by ultracentrifugation at 100.000g for 1h and dialysed at NTE buffer (120 mM NaCl, 1 mM EDTA, 20 mM Tris-HCl at pH 8.0) at 4°C overnight with agitation in Float-A-lyzer G2 dialysis devices with Molecular Weight cut-off (MWCO) of 1000 kDa (Spectra/Por®). This step is hereafter defined as 'the preliminary purification step'.

The Iodixanol has many advantages when compared with traditionally used solutions such as sucrose or CsCl, such as not being toxic to the cells and by having no reported deleterious effects either in the infectivity nor the physical structure of viruses to date (140). There are reports for example in which the use of sucrose caused a loss of the glycoproteins in *Retrovirus* (141).

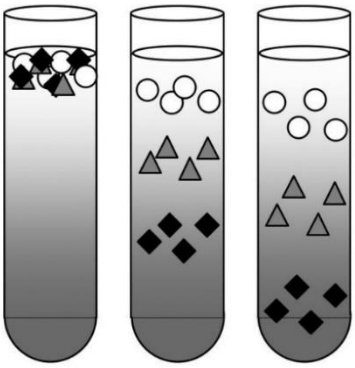

Figure 15. Schematic representation of a purification through a gradient. Particles with different buoyant densities previously pooled together are separated through a preformed density gradient by means of ultracentrifugation in a swinging-bucket rotor. Obtained by Lawrence *et al.* 2010.

Next, the particles were purified by means of an iodixanol gradient with a known range of ρ, a step called ´buoyant separation step´. Briefly, a discontinuous gradient was made with 1 mL layers of 15, 20, 25 and 30% (v/v) Optiprep™. The distinct % layers are diluted in NTE buffer, added to the centrifuge tube topped with the dialyzed cushions with the virus from the ´preliminary purification step´. The samples are then ultracentrifuged at 200.000 g with a swinging-bucket rotor SW 40 Ti (Beckman Coulter) for 2h without a break setting.

The Optiprep™ solution at different % adopts different values of ρ, which allows the separation of the particles based on this physical property. SBV particles were mainly obtained between 1.111 and 1.131 g/ml (20 and 25% Iodixanol respectively, as described in Table 5). Samples corresponding to the different buoyant ρs are carefully retrieved separately from the centrifuge tube with a micropipette and NTE-dialyzed over-night with Float-A-lyzer G2 dialysis devices MWCO 1000 kDa (Spectra/Por®).

% Optiprep™ (Iodixanol)	ρ (g/mL)
30	1.163
25	1.131
20	1.111
15	1.084

Table 5. Distinct values of ρ (g/mL) for each % of Optiprep™ used at the discontinuous purification gradients for the ¨buoyant separation step¨.

Purification II proceeded similarly as Purification I, now implementing a MOI of 0.1 when infecting the BHK cells (65,142). This MOI was kept unchanged for the next protocols. At *Purification III*, a continuous gradient between 15 and 30% Optiprep™ was prepared with a Gradient Master IP107 (Biocomp) and implemented for the ´buoyant separation step´. In *Purification IV*, 3.6 x10^{8} cells were infected. Also, this protocol had as particularities (i) using discontinuous gradient for the ´buoyant separation step´ so as Purifications I and II; (ii) an additional 22.5% Optiprep™ layer was added to this step between 20 and 25% Optiprep™ layers and (iii) all the distinct ρ layers had 2 mL of volume. *Purification V* kept the same modifications of Purifications IV, with the addition of (i) alternatively to the dialysis, in order to lower the Iodixanol concentration at the 'the preliminary purification step' the 0.5 mL 30% Optiprep™ cushions were diluted into 4.5 mL of NTE and (ii) an overnight centrifugation (for 18h) at the ´buoyant separation step´. Table 6 summarizes all the purification protocols utilized during the thesis work and their respective particularities.

Purification protocol	BHK cells infected	MOI	Volume of the fractions at the separation step	Other particularities	
I	3x10^{8}	0.01 (139)	1 mL	-	
II		0.1 (65)		-	
III			-	Continuos gradient	
IV	3.6x10^{8}		2 mL	22.5 % Optiprep™ step added	-
V					Cushions not dialysed; ultracentrifugation over-night

Table 6. Summary of viral purification protocols utilized. Depiction of the differences between the SBV purification protocols implemented in the present work.

It's worth mentioning that, before the time frame of the present thesis, other batches of SBV viral particles had already been produced by Dr. Boshra, a previous member of the Abrescia lab. Briefly, BHK cells were used to propagate the virions and those were purified by polyethylene glycol sedimentation followed by Optiprep™ density gradient ultracentrifugation. The present work had this previous protocol as a starting point. However, the attempts on implementing the production of SBV particles described previously were focused in producing a higher yield of particles, a fundamental step for automatic cryo-EM data collections.

II. Viral titration

After the buoyant densities' separation step, the different NTE-dialyzed viral samples are titrated in order to obtain the number of infectious viral units per volume. Infectious particles were obtained when cytopathic effect (CPE) was detected. The viral titers were obtained by means of the median tissue culture infectious dose ($TCID_{50}$) values: the dilution of pathogen required to infect 50% of cells in a cell culture (143). Briefly, viral samples were 1:100 diluted in 0% FBS DMEM (3µL virus: 297 µL culture media), serially 10-fold diluted and inoculated into BHK cells seeded in 96-well plates at 80% confluency previously washed with 0% FBS DMEM. The infection proceeds with agitation for 3h following the addition of 5% FBS DMEM in order to raise the percentage of FBS to 2% and finally the infected cells are incubated at 37°C with 5% CO_2 for 72h.

The $TCID_{50}$ values were then obtained using the Reed-Muench Method (144). In a first step, the 96 well infected plate were inspected with an Axiovert 40C inverted phase contrast microscope (Zeiss). CPE positive wells were identified when the BHK cells were mainly found detached from the well surface. For each dilution in which CPE is observed, the percentage of CPE positive and negative wells for the given viral dilution is retrieved. Next, the proportional distance (PD) is calculated with Formula I:

$$\mathrm{PD} = \frac{\%\text{positive above } 50\% - 50\%}{\%\text{positive above } 50\% - \%\text{positive below } 50\%}$$

Formula I: Proportional Distance, obtained from Lei *et al*. 2020.

The PD value is subsequently applied into Formula II that gives the end point dilution of the sample. The reciprocal of this value is the titer, adjusted by the viral inoculum used initially in the serial dilution.

$$\log ID_{50} = \log(\text{dilution with} > 50\% \text{ positive CPE}) + \mathrm{PD} \text{ x } (-\log(\text{dilutionfactor}))$$

Formula II: Endpoint dilution (ID_{50}) formula according to the Reed-Muench Method. Lei *et al*. 2020.

III. Immunoblot

Viral purification was also monitored by a classical immunoblot procedure (126). Briefly, to test for the presence of SBV, samples were mixed with SDS-PAGE loading dye under non-reducing conditions (no 5% β-mercaptoethanol is added) and boiled at 95°C for 5 minutes. The mixture was loaded into a 10% polyacrylamide gel followed by SDS-PAGE until separation is complete. The samples were transferred into a nitrocellulose blotting membrane (Amersham), which was blocked for 2h on 5% non-fat dry skim milk powder (VWR Chemicals) in PBS Tween-20 (Sigma) (PBST). The membrane was subsequently incubated for 1h with the 5F12 antibody (Ab), kindly provided by Dr. Aebischer and Dr. Beer (Insel Riems, Germany) and directed against the G_C protein from the SBV spike. The membrane was washed three times with PBST and incubated with Goat anti-mouse Ab conjugated with Horseadish peroxidase (Jackson Immuno Research). The membrane was again washed thrice with PBST and was revelated with ECL™ prime western blotting detection reagents (Amersham). Briefly, Luminol, the HRP substrate present in the blotting detection kit, in the presence of the secondary Ab conjugated enzyme and H_2O_2, emits light at 428 nm and allows the identification of the target proteins by imaging the membrane through an Image Quant 4000 detector (GE Healthcare).

IV. Negative stain and immunolabeling

Negative stain is an excellent technique to preliminarily assess the quality of samples in terms of homogeneity and concentration by Transmission Electron Microscopy (TEM) (145). Carbon coated copper grids (QUANTIFOIL® Carbon 300 mesh) were first glow discharged in a high vacuum coating system (10 mA 2 x 10^{-1} mbar in air for 30 seconds, MED 020 BALTEC). This is done so that the hydrophobic surface of the carbon grid is ionized and the grids are hydrophilized: ions and radicals generated by this process both remove possible contaminations from the grid and reduce its hydrophobicity, favouring the spreading of an aqueous sample (146).

Immediately after the carbon-coated grids glow discharge treatment, a drop of 10 µL of sample is deposited with a micropipette over the side where the plasma was applied After washing three times with NTE buffer to remove the excess of the targeted macromolecules that have not attached to the grid, one minute each, it was stained with 8 µL of a heavy atom solution either 2 % UAc (w/v) or 2 % Nanovan® for 1 minute. Excess of solution was removed from the side of the grid with Whatman filter paper (Cytiva). The grid was air dried overnight. The heavy metal salt solutions, apart from inactivating the viruses, work by dispersing the e^- (electron) beam which increases the contrast of the sample. This way, the specimen is easily identified.

For the negative stain immunolabeling of the virus sample, carbon coated copper grids (QUANTIFOIL® Carbon 300 mesh) were glow-discharged as described previously and receive 15 µL of sample for 10 minutes. After two washes with NTE buffer, 1 minute each, the grids were incubated with 0.2% glutaraldehyde in NTE for 15 minutes. The fixative agent prevents degradation of the sample, which is important when visualizing fragile virions like SBV, apart from inactivating the viruses (147). After 5 minutes washes in NTE, the residual glutaraldehyde was neutralized for 15 minutes in NTE containing 0.02 M glycine, that was also washed in NTE thrice for a minute. Alternatively, immunolabeling procedures without fixing step were also implemented.

Next, the grids were blocked [NTE + 1.0% ovalbumine (Sigma)] for 10 minutes and treated with the blocking solution containing the 5F12 Ab anti-SBV G_C for one hour. After four 1-minute-long washes with blocking solution, the primary Abs were detected by incubating for 1 h with anti-mouse Immunoglobulin G (IgG) conjugated to 10-nm colloidal gold (Sigma). Next to the immunolabeling and subsequent washing procedures, three times with NTE and three times with distilled water, the grids were negative stained as described above with either Uac or Nanovan®. Both standard negative stain and immunolabeling grids were visualized using a Jeol JEM-1230 TEM operating at 120 kV (kilovolts), equipped with an Orius SC1000 (4008 x 2672 pixels) cooled slow-scan charge coupled device (CCD) camera (Gatan,UK) at the EM platform at the CIC bioGUNE (Derio, Spain). The imagens were taken underfocus in a range between -2.5 and -3.5 µm at a 30k magnification.

V. Vitrification

To visualize a macromolecular complex in a close-to-native condition by TEM it is necessary to have the sample vitrified. This is achieved by flash-freezing it in a liquid cryogen avoiding the formation of ice crystals (148). This technique was first developed by Jacques Dubochet and colleagues in 1984 and allows the sample deposited onto the grid to remain in an amorphous non-crystalline state prior to image acquisition in cryo-conditions (149,150).

Specifically, in order to vitrify an aqueous solution, the temperature needs drop faster than 10^6 K/s. This is usually achieved by rapid plunge freezing the specimen into liquid ethane, propane or a mixture of both. Those cryogens are used due to their high cooling capacity (the required cooling rates to vitrify water have been estimated to range from 10^5 up to 10^8 K per second) and since they do not solidify when maintained at the temperature of liquid nitrogen (-182°C) (151,152). However, by water being a poor thermal conductor, the sample should be less than 3 µm thick so that it retains the vitrified state as whole (146). Moreover, thicker samples would unable the electrons to pass through them, resulting in undesirable multiple scattering events and a drop in the contrast of the collected images (148).

Prior to vitrification, in our case, the grids (QUANTIFOIL® R 2/2 Cu 200 and R 3.5/1.5 Cu 300) received an extra thin amorphous carbon layer. This additional film is added to overcome the low concentration of the SBV particles and improve their dispersion into the support (146, 148). Next, the grids were glow discharged as described previously and the viral samples ($TCID_{50}$ 10^8) applied on top, with or without the presence of 10 nm gold trackers (Electron Microscopy Sciences Aurion). Such gold trackers are maintained in the presence of BSA to prevent clumping and promote a better dispersion of the trackers in the grids. Such trackers, or fiducials, strongly scatter the e^- beam providing high contrast, important for the alignment of the tilted-series for cryo-ET, as described further. The vitrification proceeded using either a Vitrobot Mark III or an Automatic Plunge Freezer EM GP2 (Leica Microsystems®) operating with 95% humidity and 5°C. Different settings of sample addition were tested i.e., 4 µL followed by 30´ incubation or 2 µL followed by 10 seconds incubation repeated 3 times. The latter has improved particle dispersion and concentration on the grid. After incubation, the grid was blotted for 2 seconds with a filter paper and rapidly dropped by the plunger into liquid ethane at -182°C. Finally, the grids were stored into a liquid nitrogen container G21 (KGW Isoterm) until used for cryo-imaging.

VI. Transmission electron microscopy

The first TEM prototype was developed by Ernst Ruska in 1932, being commercially available in 1939 (153). Ruska was awarded a Nobel prize in Physics for his work in e^- optics and the design of the first EM later in 1986 (154). An e^- gun (i.e. a Tungsten filament receiving an electric current) extracts e^-s due to their thermionic energy on heating, a process called thermionic emission (155). The e^-s are then accelerated by a potential difference, typically ranging from 100 to 300 kV, to penetrate through the sample on the grid, located in a sample holder and maintained into high vacuum conditions (156). The e^- beam is then focused by electromagnetic lenses (the condenser lenses) ultimately reaching the sample (157). It's worth mentioning that the thickness of the material to be imaged has direct impact in the scattering of the e^-, being higher potential differences needed in order to cross thicker specimens (156). Objective lenses further down focus the beam that crossed the sample (157) and projector lenses work on achieving the desired magnification of the image (158). Such image, or projection, is mainly obtained by means of scattering events in the e^- waves caused by the interaction of such waves with the sample.

Following the microscope column path magnified images derived from a sample are obtained by a beam of e^- after hitting a thin specimen. The final product of this contact with the sample is a combination of unscattered, inelastic and narrow angle elastic events interacting simultaneously with each other (159). Unlike X-rays, e^- waves can be bent and focused by the magnetic field of the microscope lenses, and the re-combination of the scattered events originates the image, further on magnified by the projector lenses before being collected at the adequate detector (160). Thus, the biological specimen directly modulates the phase of newly formed e^- waves after interaction with the matter. Finally, the so-called brightfield image is obtained at a detector (160-162).

The wave nature of matter, which has been confirmed with many of particles from e^- up to whole molecules, was first proposed by the Nobel prize laureate Louis de Broglie (163) and is defined by Formula III. At a TEM however, since the e^- is being accelerated at high (and known) voltages the kinetic energy values are easily obtained along with the speed, calculated using the relativistic kinetic energy formula (Formula IV-A) given that the mass x energy of an e^- particle is known to be 511.000 eV. The de Broglie formula can then be adapted taking γ (Lorentz factor) in consideration (Formula IV-B), which is dependent on the voltage of the microscope, along with the known mass of an e^- (9.11×10^{-31} kg) and the speed of light (300,000,000 m/s) (Formula IV-C). The wavelength (λ) obtained is the theoretical limiting resolution that a TEM can achieve under a specific voltage. The real resolution of a microscope, however, is limited by a series of additional factors (164).

$$\lambda = \frac{h}{p} = \frac{h}{mv}$$

Formula III: De Broglie formula in which λ is the wavelength; h is the Planck´s constant (6.63×10^{-34} J x s); p is the momentum of the particle; m is mass and v is the speed. Adapted from Williams and Carter, 1996.

LAS PAGINAS 69 A 91 ESTAN SUJETAS A CONFIDENCIALIDAD POR EL AUTOR

All purified proteins had their integrities checked by MALDI-TOF MS as shown in Figure 26. However, the yield of proteins obtained was minimal by the end of the purification process after cleavage of the GST tags. It's worth mentioning that, for all proteins, 6 aa residues (LHPHRD) were expressed after the C-terminal His$_6$-tags. The former corresponding coding sequences are located between the cloned His$_6$-tag codons and the stop codons located downstream of the pGEX-4-T1 multiple cloning site. The addition of these 12 aa residues at the C-terminal extremity of the proteins adds approx. 2 kDa to their final molecular weights.

Due to the minimal amount of protein obtained when GST was cleaved (and that the constructs were insoluble when this fusion protein was absent), all constructs were re-purified without cleaving out the GST tags. The purifications were concluded at the SEC step with 1X PBS after the 20 mM glutathione elution. The proteins were obtained at concentrations of 0.6 mg/mL (N-terminal, C3, C4) and 1.4 mg/mL (C2). GST alone was also produced following the same protocol and obtained at a concentration of 3 mg/mL (Figure 27). After purifications and MS quality control steps, the proteins were stored at -80°C until further use.

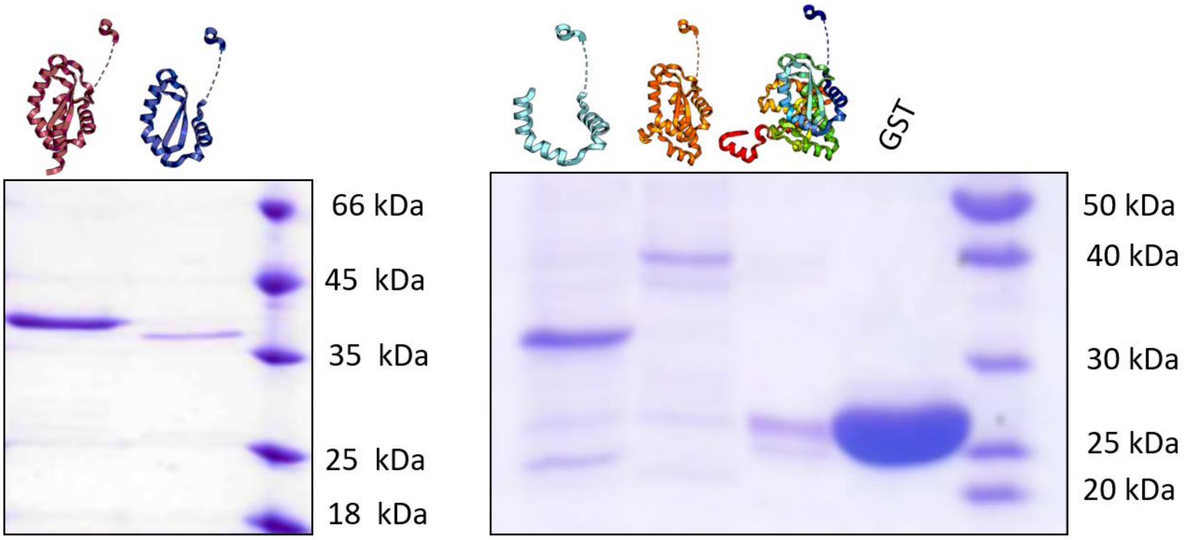

Figure 27. Purified proteins by the end of all purification routes. SDS-PAGE gel from the different proteins obtained, being the corresponding band followed by the cartoon representation of the protein on top. From left to right: C2+GST (in violet; 40 kDa), C3+GST (in dark blue; 37 kDa), C4+GST (in cyan; 32 kDa), N-terminal+GST (in orange; 42 kDa), full SBV-N (rainbow; 26.1 kDa) and GST (25 kDa).

II. Cell proliferation assays after C57BL/6 mice immunizations

A. Investigation of CD8+/ CD107+ T cell expansion and IFN-γ secretion mediated by SBV-N and N-terminal stimulation: first insights on the protective potential of the N-terminal region of the Nucleoprotein

In frame with previous immunizations assays with the SBV-N and its cDNA (69,70), our work was directed, initially, at uncovering if the N-terminal or C-terminal portions of the protein, or even both, were responsible for protection. Due to the limited production of the recombinant C-terminal[a] domain (Phe134-Ile233), only the N-terminal domain (Met1-Thr133), obtained from inclusion bodies as described previously, was used. The full SBV-N and PBS were utilized as controls apart from Quil-A Saponin utilized as adjuvant in all immunogen formulations.

C57BL/6 animals were immunized with SBV-N and N-terminal domain (n=2 per group). Further, their spleens were harvested and re-stimulated with these same proteins (see Materials and Methods). The re-stimulation with SBV-N of splenocytes derived from both N-term and SBV-N immunized groups showed a higher percentage of IFN-γ producing CD8+ cells than the PBS control by FACs (Figure 28A). This result began indicating the N-term, and consequently smaller fragments of it, as possible immunogens. Consistently with this result, IFN-γ ELISA developed with supernatants from these splenocytes showed again higher levels of the SBV-N and N-Term immunized than the PBS control, although in this case the stimulus utilized was N-term (Figure 28B).

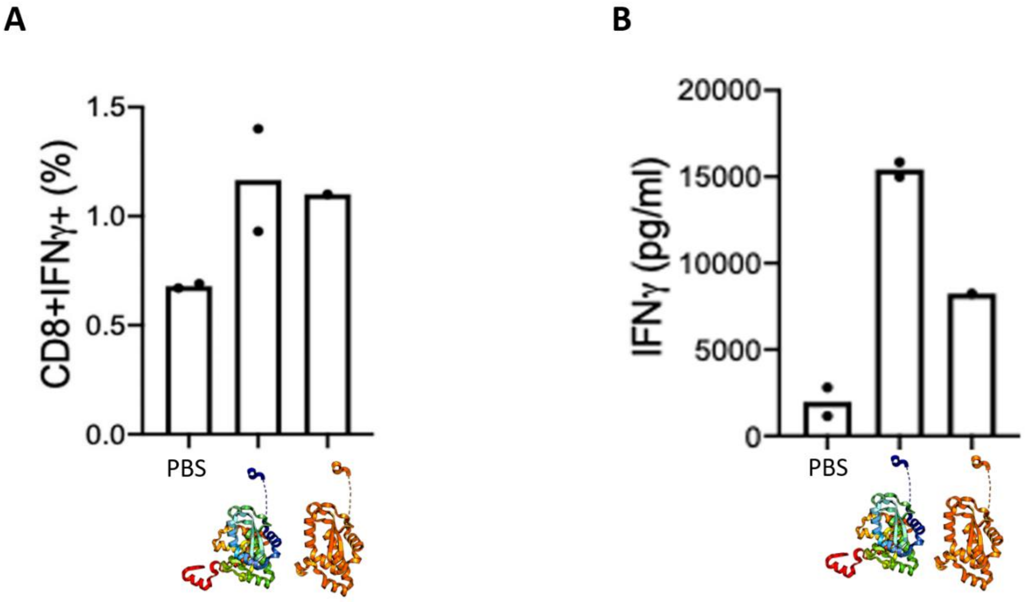

Figure 28. Insights on the capability of N-term on retrieving a cell mediated immune response. A FACs results showing the percentage of IFN-γ producing CD8+ cells mediated by stimulation with the full SBV-N. Each bar represents an immunization group of the C57BL/6 mice from the first round of immunizations: PBS, SBV-N (as shown in cartoon coloured in rainbow) or N-term (coloured in orange). **B** IFN-γ concentration (pg/ml) from the supernatants of the splenocytes re-stimulated with N-term. Bars organization follows the same pattern as in A (each one representing a group of immunization).

B. Investigation of $CD8^+$/ $CD107^+$ T cell expansion and IFN-γ secretion mediated by peptides P1-P7 stimulation

The SBV-N derived peptides obtained by the NetMHCpan-4.0 server were also used as stimulus in this first round (P1-P7, Table 2, Materials and Methods section). Briefly, the splenocytes derived both from SBV-N immunized and PBS injected controls were checked for the percentage of IFN-γ producing and 107+ CD8 cells by FACs, a primary attempt to directly uncover any of those peptides as binders to the MHC-I and consequently possible peptide vaccine prototypes. As shown in Figure 29A, apart from no prominent cell population in PBS immunized controls, as expected, none of the peptides seemed to trigger CD8+ cell re-stimulation in terms of % of IFN-γ producing CD8+ cells. The same baseline of values to the unstimulated control (in light pink) indicates that the present proportion of cells was achieved only due to the immunization itself with SBV-N. Moreover, a similar outcome was obtained regarding the % of cytotoxic $CD8^+/107^+$ cells, which by expressing 107a, a lysosomal-associated membrane protein (LAMP), can be used as a marker for cytotoxic CD8 cells, Both results corroborate that the basal stimulation obtained was guided by the immunization with SBV-N only and that all the peptides failed on retrieving a positive result in inducing cell-mediated immune response (Figure 29B).

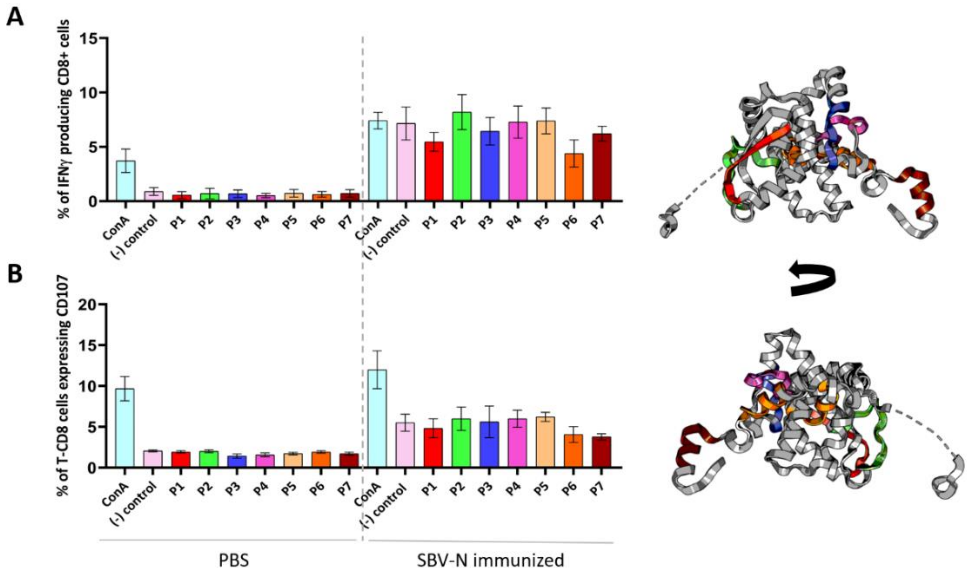

Figure 29. Inability of the in silico predicted peptides on triggering cell mediated immune response. (A) FACs results showing the percentage of IFN-γ producing CD8+ cells mediated by stimulation with the different peptides. Each bar represents a stimulus being the first 9 columns, including ConA and non-stimulated controls, referring to PBS immunized control animals and the last 9 columns to SBV-N immunized. (**B)** FACs result showing cytotoxic CD8 cells LAMP 107a+ populations upon the same stimuli as in (A), ordering of the columns also follows the same fashion. Colouring pallet of the peptidic stimuli follows the same scheme as the cartoon of SBV-N showed in the right, which was presented in details in the *peptide design* at the Materials and Methods section. Error bars represent the SD.

C. Investigation of CD8$^+$/ CD107$^+$ T cell expansion mediated by proteinaceous constructs: narrowing down to the C4 as possible vaccine target

To assess the presence of MHC-I epitopes in the N-terminal portion of the nucleoprotein (Met1-Thr133), following the previous results, new vaccine formulations containing full SBV-N, N-term or GST, each adjuvanted with Quil-A Saponin, were used to immunize a new round of C57BL/6 mice (n=3 per group). Their splenocytes were isolated and then re-stimulated with either PBS, ConA, full SBV-N, N-term, C2, C3 or C4 fragments, being all the latter four attached to a GST-tag. FACs analyses using splenocytes from mice immunized with GST and re-activated with the different constructs did not show an increase in CD8$^+$/CD107$^+$ cell populations when compared to non-re-activated cells (Figure 30, grey bars).

In the case of spleens derived from animals immunized with the full SBV-N, following re-stimulation with this same protein, the CD8$^+$/CD107$^+$ average population was 7.1% higher than the SBV-N immunized non-activated control, and 4.4% higher than the GST immunized pool subjected to the SBV-N stimulus (Figure 30 purple bars). Differently, the splenocytes derived from the mice immunized with N-term, and re-stimulated either with the N-term protein or C4 fragment showed significantly higher CD8$^+$/CD107$^+$ cell populations, 14% and 17% respectively, than the corresponding GST immunized derived splenocytes under these same stimulus (3.9% and 3.1% CD8$^+$/CD107$^+$ cells, respectively) (Figure 30, orange bars).

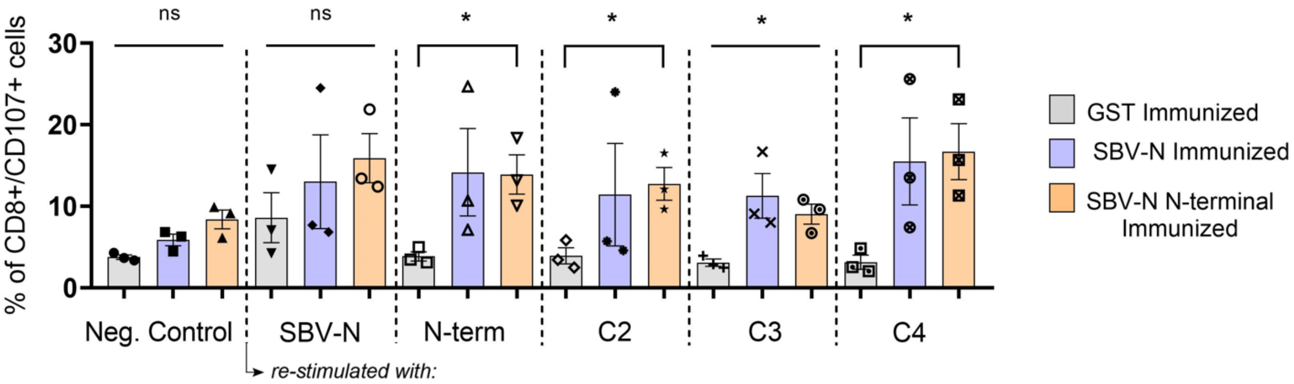

Figure 30. CD8$^+$ CD107$^+$ (%) T cells identified by FACs upon re-stimulation with different proteinaceous stimuli. Each group of columns represent the mean (%) CD8$^+$ CD107$^+$ T cells (*y* axis) obtained for the different stimulus (*x* axis); colours indicate the used immunogen: GST (grey); SBV-N (full SBV-N in purple), SBV and N-term (SBV-N N-terminal in orange). the columns represent the means; error bars represent the SDs. Asterisks represent statistical significance with $P < 0.05$ (*) on ANOVA one-way test.

The supernatants of stimulated splenocytes from differentially immunized animals were also analysed for IFN-γ secretion using ELISA. In the control group immunized with GST, IFN-γ release was detected independently of the stimulus employed even when they are compared to the group activated with ConA (Figure 31 grey bars), which suggests an intrinsic immunogenic capacity of this transferase in terms of cytokine induction. On the other hand, supernatants derived from full SBV-N and N-term immunized mice splenocytes and re-stimulated with either of the targeted proteins all elicited significant higher IFN-γ levels when compared to non-activated controls (Figure 31 purple and orange bars).

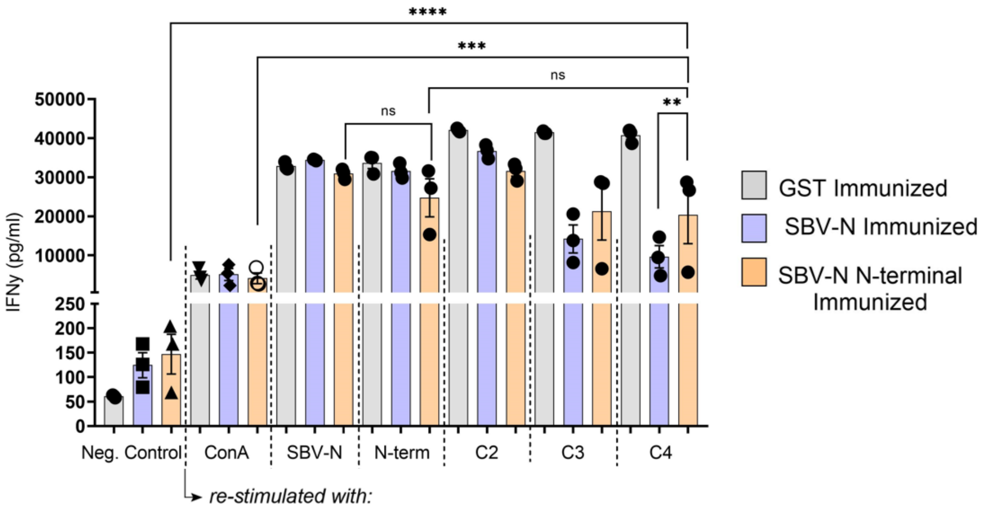

Figure 31. IFN-γ concentration (pg/ml) from the splenocytes supernatants for the given stimulus. Each group of three columns represent the mean IFN-γ concentration (*y* axis) obtained for the different stimuli (*x* axis); colours indicate the used immunogen: GST (grey); SBV-N (full SBV-N in purple) and N-term (SBV-N N-terminal in orange). ConA (concanavalin A). The columns represent the means, error bars represent the SDs. Asterisks represent statistical significance with $P< 0.01$ (**); $P < 0.001$ (***) or $P < 0.0001$ (****) on ANOVA one-way test.

The results obtained by means of the second round of C57BL/6 mice immunizations and further splenocytes re-stimulations converge with each other: first, a the robust CD8$^+$/CD107$^+$ T-cell response was seen by using C4 as stimulus. Also, the IFN-γ response derived from the re-stimulation with the smallest fragment C4 (Met1-Ala58 from the original SBV-N, present in all other larger fragments) over the negative controls was significative. Together, these results pinpointed the C4 fragment as a candidate to contain MHC-I epitope(s). Still, we cannot exclude the existence of other epitopes in the C-terminal domain of the SBV-N. As already mentioned, neither C-terminal^a (Phe134-Ile233) nor C-terminal^b (Gln59-Ile233) could be successfully expressed and further tested in this sense.

III. **IFNAR $^{-/-}$ mice immunized with subunit vaccine candidates C4 and SBV-N N-terminal are protected from virulent SBV infection**

Following the previous results that show the capability of C4 and N-terminal in stimulating CD8+ expansion and IFN-γ secretion with a C57BL/6 mice model, we performed immunological studies on vaccinated mice challenged with a virulent strain of SBV. IFNAR$^{-/-}$ mice were immunized with vaccine formulations containing either GST, SBV-N, N-term or C4, all using Quil-A saponin as adjuvant (n=7 mice per group). Then, mice were challenged with BH619/12-7, a virulent strain from SBV, subsequently both monitored for weight loss and signs of morbidity and had blood samples taken from them at different timepoints, as ascribed in the next session.

Regarding the health monitoring of the animals after the viral infection, while the not challenged group remained healthy along the duration of the experiment (up to 14 dpi) (Figure 32A), the group of mice not immunized or immunized only with GST presented the highest number of casualties (Figure 32 A and B, respectively). All animals from both groups presented at least one clinical sign of morbidity at 3 dpi (ruffled hair, hunched back, ataxia or conjunctivitis) followed by loss of weight. One animal was also found dead at 4 dpi in both groups. At 5 dpi, one severely compromised animal from the non-immunized group was sacrificed and two mice from the GST group were found dead.

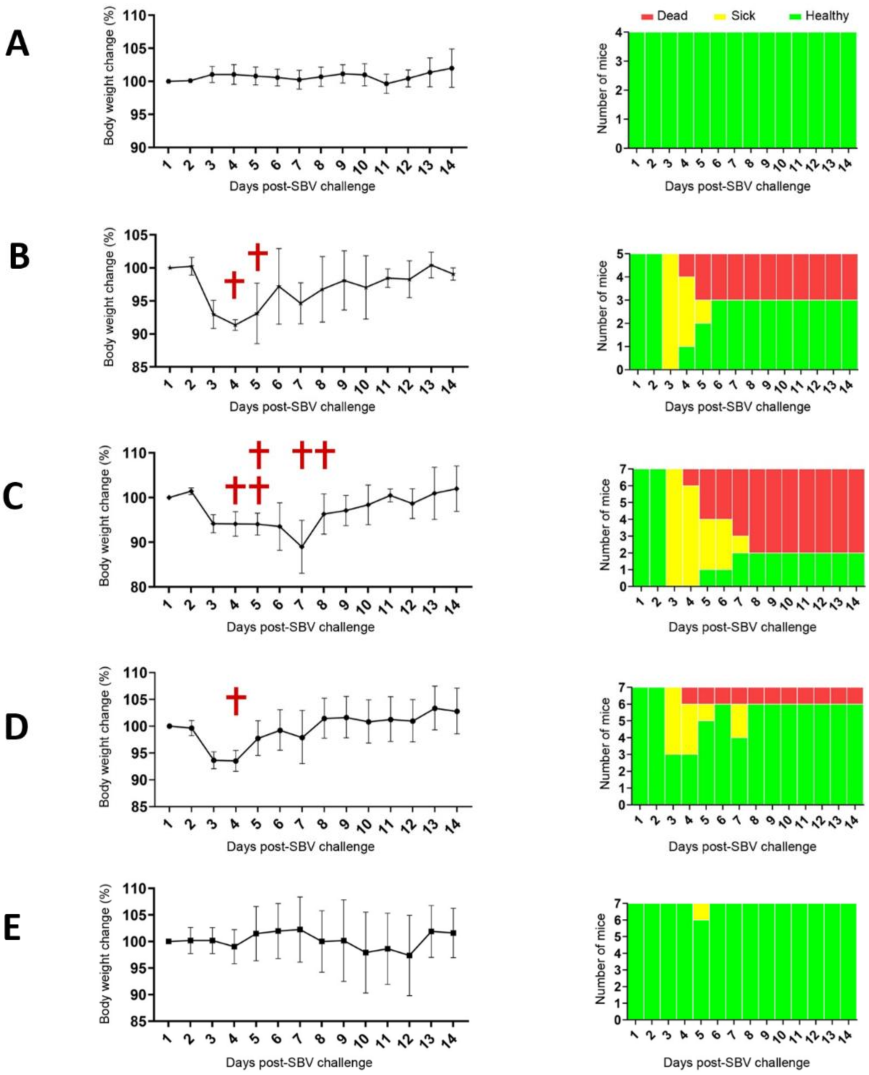

Figure 32. Health evaluation of IFNAR$^{-/-}$ mice following virulent SBV challenge. Left, body weight variation plots (%) from the different animal groups at each day post-SBV challenge shown as medians, the error bars represent the SDs, red crosses represent an animal either found dead or sacrificed at the given day. Right, health monitoring plots. Colouring scheme shows the health status of the given animal being healthy (green), presenting any signs of morbidity (yellow), and either found dead or sacrificed (red) at the given day post-infection. **(A)** Mice neither immunized nor SBV challenged. **(B)** Not immunized and SBV challenged**. (C)** GST immunized and SBV challenged. **(D)** C4 immunized and SBV challenged. **(E)** N-term immunized and SBV-challenged.

Further, another mouse from the GST group that presented both hunched back and ataxia but not a prominent weight loss since 3 dpi was sacrificed by 7 dpi and a fifth animal from the same group that presented ataxia but not a loss of weight was dead by 8 dpi. The remaining two animals from the GST group recovered their initial weights and showed no signs of morbidity from 7 dpi onwards. All remaining animals from the not-immunized group recovered from any clinical signs, gaining weight after 6 dpi.

Regarding the C4 immunized animals, at 3 dpi the group had a generalized decrease in weight and four out of seven presented ruffled hair. Only one of these animals also presented ataxia in addition to a approx. 20% of weight loss and was sacrificed at 4 dpi. By 6 dpi, all remaining animals appeared healthy although two mice that had presented ruffled hair at 3 dpi were found again in this same condition at 7 dpi. However, this event was neither accompanied by any other clinical sign nor weight loss and from 8 dpi on no clinical signs were observed again (Figure 32D). Apart from one animal that presented conjunctivitis by 5 dpi, the mice group immunized with N-term remained healthy during the whole experiment. Moreover, opposite to the non-immunized, GST and C4 immunized groups, the weight-monitoring curve of the N-term immunized animals did not vary more than 5% on average (Figure 32E). All control animals immunized with the full SBV-N remained healthy during the time course of the experiment (Appendix IA).

IV. Immunization with C4 fragment decreases viraemia in infected IFNAR$^{-/-}$ mice

Together with the health monitoring of the SBV challenged IFNAR$^{-/-}$ mice during the course of the experiment, blood samples from these animals were harvested at distinct time points (3, 6 and 10 dpi). RNA extraction from each sample and quantification of SBV´s genomic RNA was performed by RT-qPCRs (see Materials and Methods). The N-term and C4 vaccinated groups retrieved the lowest detectable levels of SBV genome copies at 3 dpi, both with statistical significance when compared to the control groups (Figure 33).

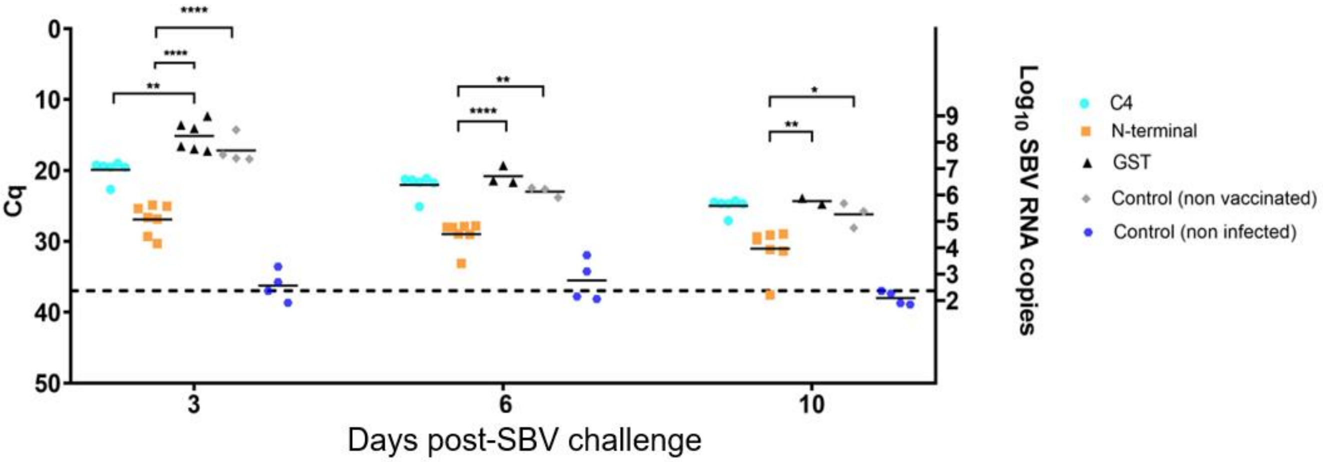

Figure 33. Quantification of viraemia post viral infection. 75 µL Blood samples were harvested at 3, 6 and 10 dpi followed by RNA extraction and RT-qPCR. Values plotted are the Cqs obtained at the RT-qPCRs and the corresponding $\log_{10}$ SBV RNA copies per sample at the given dpi, being each point a different animal that was alive at that timepoint and a blood sample could this way be harvested. The dashed intense line corresponds to the RT-qPCR threshold. Horizontal bars

represent the medians among the distinctly immunized groups, which are coloured as follows: Cyan (C4); orange (N-term); black (GST); grey (not immunized); dark blue (neither SBV challenged nor immunized). Asterisks denote statistical significance with $P < 0.05$ (*), $P < 0.01$ (**) or $P < 0.0001$ (****), as denoted by one-way ANOVA test.

At 3dpi, the difference in the RNA copy numbers between N-term and C4 derived samples was of the order of 10^3 and 10, respectively, when compared to controls. The pace of decrease of viraemia remained constant at 6 and 10 dpi for the vaccinated groups, steadily approaching the viraemia values of the controls along the experiment timeframe. By 10 dpi, the difference in the RNA copy numbers between the N-term vaccinated group and controls (GST and not-immunized groups) was in the order of 10^2 and 10, respectively, whereas for the C4 vaccinated group the difference was more modest probably because survivors in both control groups might correspond with mice that controlled better the viral replication. The viraemia analysis of the full SBV-N immunized group was similar to the previously described (70) although with higher discrepancies when compared with the control groups (Appendix IB).

V. IFN-γ secretion detected in IFNAR$^{-/-}$ mice challenged with SBV: Re-stimulation of splenocytes mediated by SBV-N N-terminal

The supernatants obtained from splenocytes derived from the IFNAR$^{-/-}$ mice, previously vaccinated with the different SBV-N constructs and subsequently challenged with virulent SBV, were tested for secretion of IFN-γ. Despite some variability, the results obtained are in line with the ones obtained with the C57BL/6 mice pilot assay: IFN-γ secretion was detected when splenocytes were stimulated ex-vivo with the N-term polypeptide (Figure 34 orange), which also contains the C4 corresponding protein nested into its N-terminal extremity. Two out of three and one out of three animals, vaccinated prior the viral challenge with N-term and C4 (Figure 34 central and right trios, respectively) secreted higher levels of IFN-γ than the unstimulated ones. The splenocytes derived from the two remaining GST immunized animals on the other hand could only be stimulated for IFN-γ secretion when incubated with the ConA (Figure 34, left trio).

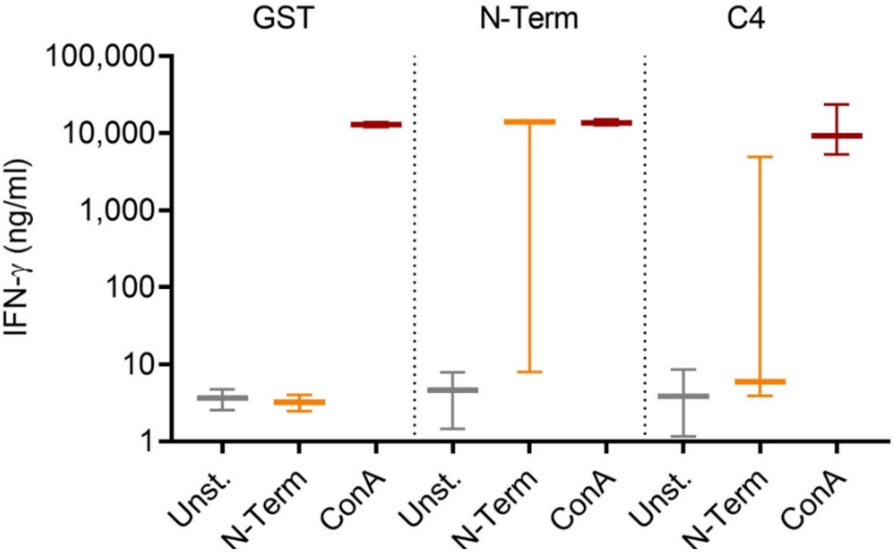

Figure 34. Secreted IFN-γ from splenocytes of IFNAR$^{-/-}$ mice after virus challenge. Splenocytes were harvested and cells were subjected to ex-vivo stimulation as follows: Three spleens from N-term and C4 immunized animals and two spleens from the remaining GST immunized controls. Secreted IFN-γ was measured by ELISA with a spectrophotometer at 450 nm and fitted to a standard curve in order to obtain the corresponding concentrations. GST (left trio) N-term (center trio) and C4 (right trio) whiskers represent the minimum to maximum values of IFN-γ concentrations along with the medians for the given group of splenocytes derived from the immunized animals unstimulated with RPMI media (left, grey) or stimulated with either N-term (center, orange) or ConA (right, brown).

Also, in agreement with the previous results using C57BL/6 mice, a basal IFN-γ secretion was detected at (i) non-stimulated splenocytes (grey bars) and (ii) GST immunized control conditions (left trio, Unst. and N-term stimuli). This could be mediated either by other cells not necessarily TCD8+ or, in this particular case, by the cell mediated response of the infection itself since the animals were challenged with SBV. This analysis, in frame with the results presented on the animal viraemia, support the ability of both C4 and N-term in providing cell-mediated protection against SBV virulent infection.

VI. Re-stimulation of challenged IFNAR$^{-/-}$ splenocytes mediated by peptides from the N-terminal of SBV-N (P. I-P. IX).

Apart from re-stimulation with N-term shown previously, the challenged IFNAR$^{-/-}$ splenocytes used above were incubated with peptides P. I-P. VI. These peptides cover the entire C4 region of SBV-N (Met-Ala58). Moreover, 3 peptides present at the interface between Ala58 and the C-terminal extremity residue of N-terminal at the original SBV-N (Thr133) were also used as stimuli (P. VII-P. IX) (details on sequences and locations of P. I-P. IX at the SBV-N structure are given at Table 3 in the Material and Methods section).

The outcome was the same as using P1-P7, which failed to re-stimulate splenocytes by obtaining CD8+ (%) populations equivalent to non-stimulated ones by FACs (in the case from the C57BL/6 mice, immunized with the entire Nucleoprotein). The results show that P. I-P. IX did not possess the ability to re-stimulate IFN-γ secretion on SBV challenged IFNAR$^{-/-}$ derived splenocytes (Figure 35). C4 (Met1-Ala58) is, at the moment, the smallest region possible of the SBV-N that we showed to provide protection against SBV infection. It remains unknown, despite our efforts on working with peptides, the exact epitope(s) that could provide binding to the MHC-I and trigger for the cell mediated immunity presented.

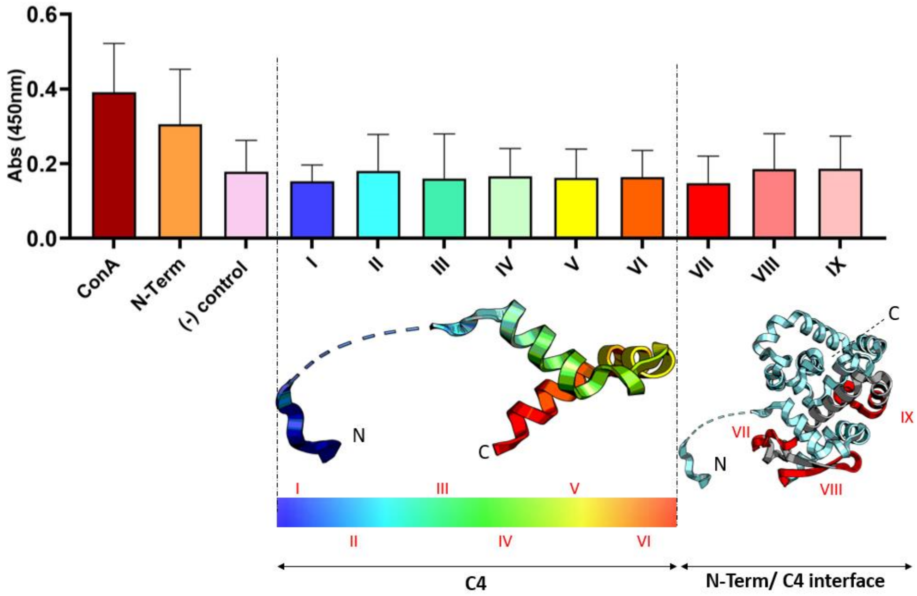

Figure 35. Analysis of secreted IFN-γ from splenocytes of IFNAR $^{-/-}$ mice after virus challenge. Splenocytes derived from N-term immunized animals were subjected to re-stimulation with different stimuli (*x*-axis): ConA, N-term and peptides P.I-PIX. Secreted IFN-γ was measured by ELISA with a spectrophotometer at 450 nm. (-) control corresponds to splenocytes unstimulated with RPMI media. Cartoons bellow the graph guide for the locations of the peptides at the C4 (P. I-P. VI) or the interface region between the C-terminal extremities of C4 and N-term (P. VII- P. IX). C and N represent the amino and carboxyterminal extremities from the constructs respectively. Error bars represent the SDs.

VII. Phylogenetic analyses

The similarities between SBV-N and its fragments C4 and N-terminal with the corresponding nucleoproteins from other *Orthobunyaviruses* was investigated. For the identification of nucleoproteins from viruses that retrieve the highest identity with the SBV-N for posterior conservation analyses by phylogeny, Blastp (133) was utilized using a BLOSUM62 scoring matrix. The obtained sequences were aligned with ClustalW (134). Panels A and B in Figure 36 depict such sequence alignment aided by the SBV-N secondary structure derived from PDB ID:3ZL9 using Esprit

3.0 (105,135). Phylogenetic tress using C4 and N-term sequences as templates were built in MEGA (136) and are also depicted. Identity values obtained by Blastp were considered and are shown in the right. A similar analysis was done with the full SBV-N (Appendix II).

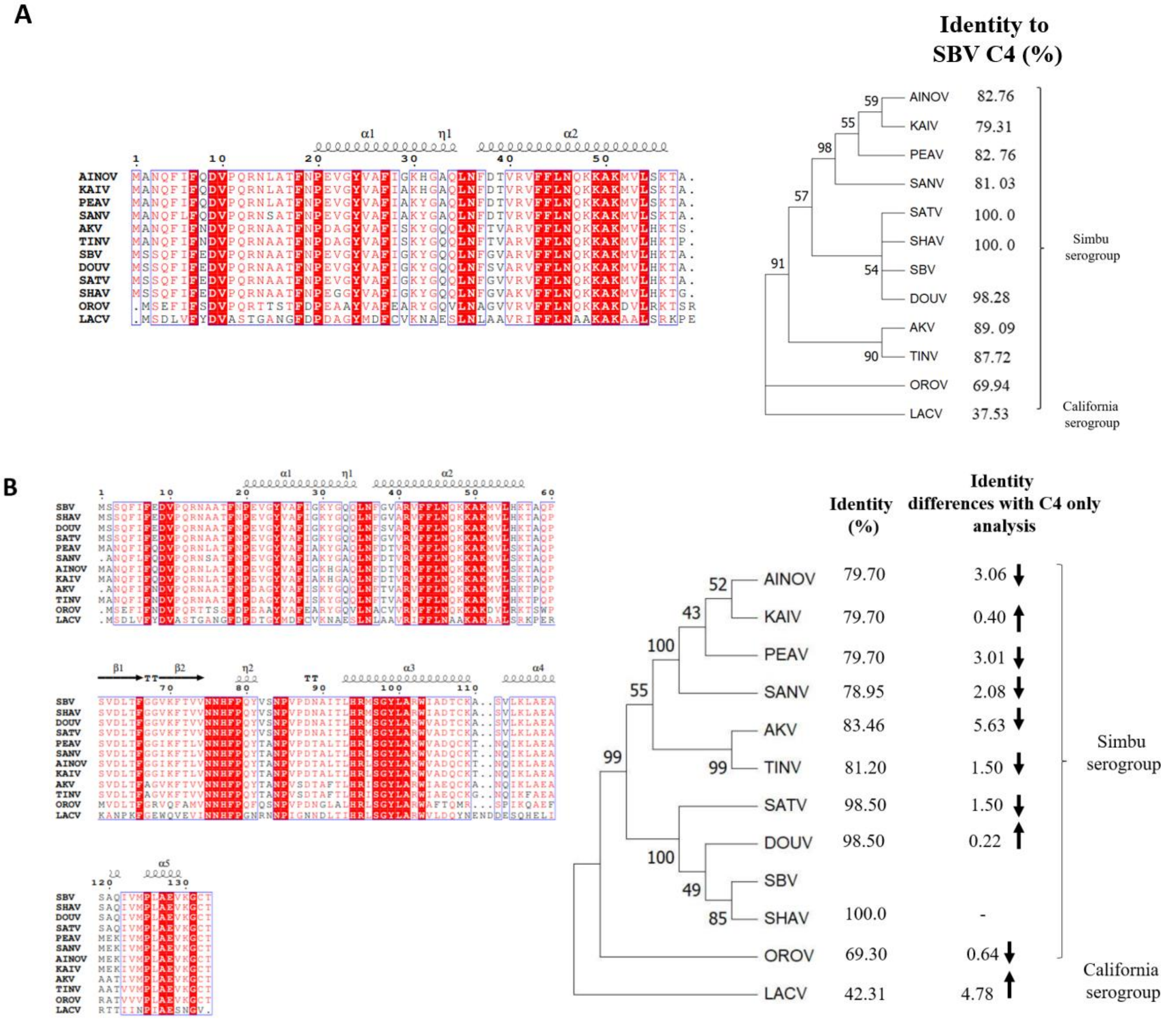

Figure 36. C4 evolutionary conservation across Simbu serogroup Left: ESPrit multiple alignments from SBV-N C4 **(A)** and N-terminal **(B)** motifs with nucleoproteins from distinct *Orthobunyaviruses*, hits were given by BLASTp and ordered from top to bottom according to the corresponding pairwise identities; above the alignments the secondary structure elements derived from PDB ID 3ZL9 (105) are shown. AINOV Aino virus; KAIV Kaikalur virus; PEAV Peaton virus; SANV Sango Virus; AKV Akabane virus; TINV Tinaroo virus; SBV Schmallenberg virus; DOUV Douglas virus; SATV Sathuperi virus; SHAV Shamonda virus; OROV Oropouche virus; LACV La Crosse virus. **Right:** Phylogenetic analysis from the previously aligned sequences carried out on MEGA with a 500-bootstrap method, correlation values are given at the tree nods being values bellow 40 not depicted. Sequences identities with the corresponding regions from SBV and the different *Orthobunyaviruses* are given at the right.

Part 2 – SBV structural studies

I. Pilot propagation and purification of SBV particles

Previous studies have shown that HeLa, Vero, and BHK cell lines support SBV infection *in vitro* (65,137,228). For our studies, we used the BHK cells for virus infection and propagation. The final purification protocol is the result of modifications and optimizations at each batch of production (*Purification I – Purification V*). The purifications had as a starting reference the purification protocol used for BUNV (140) and adapted by Dr. Boshra, a previous member of the Abrescia lab. BUNV is not only phylogenetically but most importantly morphologically very similar to SBV as already mentioned. The results obtained from the different purification protocols were the following.

As a result of the setting-up of the pilot purification (*Purification I*, Figure 37 A-C) distinct bands at the heights corresponding to the initial interfaces from the different ρ Optiprep™ steps were detected (Figure 37A). Further immunoblot showed dispersion of the possible viral particles among fractions 2-8, having each being collected as 1 mL aliquots (Figure 37B). Serial dilution followed by infection at a BHK cells seeded plate led to viral titers of the order of 10^8, specifically 3.3×10^7 and 7.2×10^8 for the fractions 4 and 5, respectively, the ones with the higher titers. It's worth mentioning that those fractions correspond to the 20%/25% Optiprep™ steps in the original gradient (Figure 37C).

Next, *Purification II* (Figure 37 D-F) was performed as an alternative virus production protocol to increase the viral yield. Despite the higher MOI utilized (0.1 versus 0.01), the outcome from Purification II was similar to I. We again obtained dispersion of possible viral particles among several fractions of the buoyant densities' separation step (fractions 3-9, Figure 37 D, E). The viral concentration outcomes were also similar. The most concentrated fractions reached titers of the order of 10^8, 5.2×10^8 and 5.9×10^8 for fractions 6 and 7 respectively, corresponding to the 25% Optiprep™ layer in the original gradient (Figure 37F).

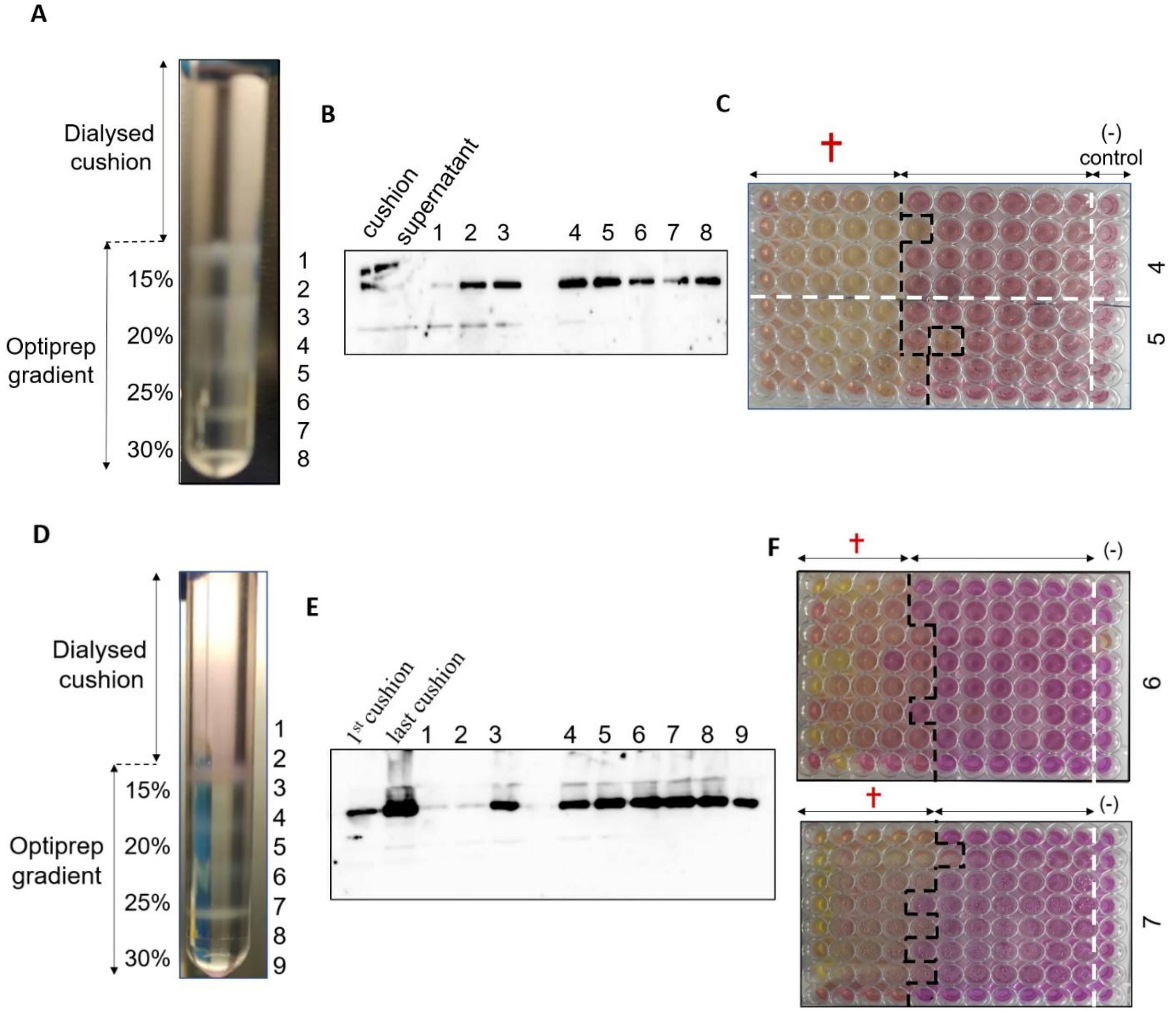

Figure 37. SBV Purifications I and II. **(A) and (D)** Depiction of the ¨buoyant separation step¨ where the dialysed cushion is loaded on top of the ρ gradient. Distinct bands are seen at the heights from the original ρ interfaces, % of Optiprep solution on NTE media at each ρ step is given (left). Corresponding fractions collected (right). A and D refer to *Purifications I and II* respectively. **(B) and (E)** Immunoblots utilizing anti G_C Ab 5F12 after non-denaturing SDS-PAGE from the distinct collected purified fractions and probes from the ¨preliminary purification step¨ (cushion and supernatant samples) for tracking. B and E refer to *Purifications I and II* respectively. **(C) and (F)** BHK seeded 96-well plates infected with serially diluted viral particles from the distinct dialysed fractions obtained at the ¨buoyant separation step¨. The dilution was performed one column to the next from left to right of the plate. Black dashed lines indicate separation between wells where CPE was detected (left, with the red cross on top) or not (right). White vertical dashed lines indicate the control column (12^{nd}), not infected with virus (-). Plates are followed by the numeration from the fraction of the purification used for infection at the right. C and F correspond to fractions from *Purification I and II* respectively.

II. SBV purification through a continuous density gradient and negative stain immunolabeling

To improve the viral yield and purity, apart from testing different MOIs and scaling-up the number of infected cells, we attempted to reduce the volume of the distinct ρ fractions. Ideally, the infective (presumably with the glycoprotein spikes intact) and integral particles should all land at a similar ρ value outcome when subjected to ultracentrifugation. To obtain the smallest volume possible of each fraction with different buoyant densities along the full range of Optiprep™ gradient in the tube, *Purification III* was devised with a continuous Optiprep™ gradient. The same ρ range as in Purifications I and II (15-30% Optiprep™) was utilized (Figure 38). Immunoblot detection with fractions 8-19, as in Purifications I and II, shows dispersion of possible SBV particles being the highest signal the one retrieved from fraction 11 (Figure 38 A and B). Fraction 11 had a viral concentration of 3.11 x 10^8 virions/mL, also in the same magnitude range of the outcomes from Purifications I and II (Figure 38 C).

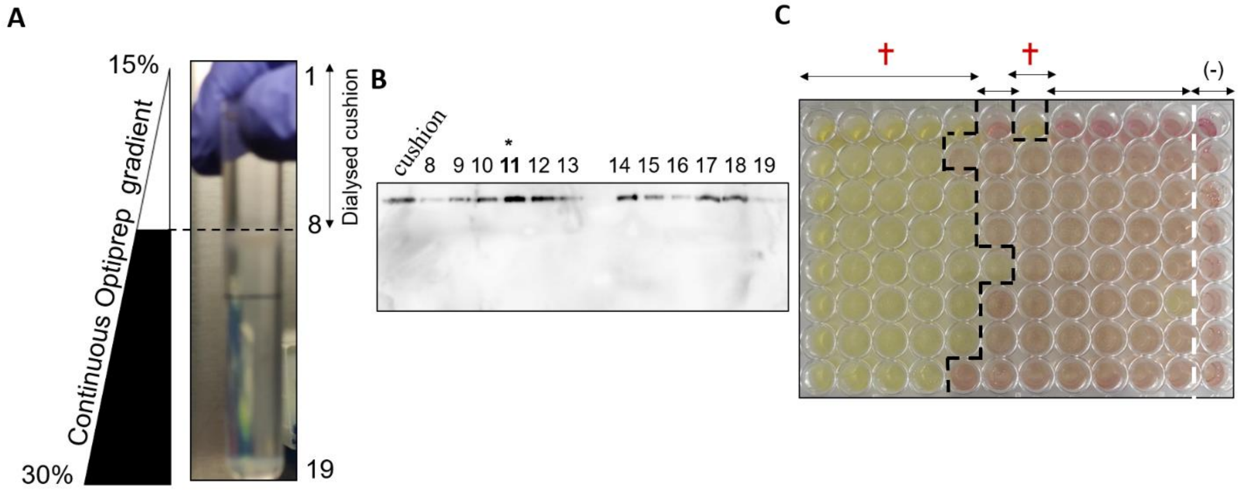

Figure 38. Purification III. **(A)** Depiction of the ¨buoyant separation step¨ where the dialysed cushion is loaded on top of the continuous 15%-30% Optiprep™ gradient. The upper part of the gradient (lower ρ section; white triangle) is replaced by the dialysed cushion (4mL) before the ultracentrifugation, the lower part of the gradient (black triangle base) remains with the higher densities. The 30% Optiprep™ region is located at the bottom of the tube. Heights of the corresponding 0.5 mL purified fractions collected 8 and 19 are depicted at the right of the tube. **(B)** Immunoblot utilizing anti G_C Ab 5F12 after non-denaturing SDS-PAGE from the distinct 0.5 mL fractions and from a sample of the dialysed cushion from the ¨preliminary purification step¨. **(C)** BHK seeded 96-well plate infected with serially diluted viral particles from the dialysed fraction 11 obtained at the separation step. The dilution was performed one column to the next from left to right of the plate. Black dashed lines indicate separation between wells where CPE was detected (left, with the red cross on top) or not (right). White dashed lines indicate the control column (12nd) not infected with virus (-).

Different layers from the purification gradient always seem to present infective particles, retrieving titers from 10^6 to 10^8 in different purification batches. This points out the dispersive behaviour of the ρ from the produced particles and complements the immunoblot outcomes.

However, the presence of vesicles containing G_C that not are necessarily mature virions, so as the presence of broken/punctuated viral particles, cannot be discharged at this step.

To further characterize the SBV particles derived from the purification procedures, negative stain immunolabeling was performed with fraction 11 from Purification III (Figure 39). Particles at the expected size range of SBV (80-110 nm) were visualized, both undecorated and decorated with high contrasted 10 nm fiducials. This was an indication of the presence of the G_C glycoprotein anchored into the lipidic envelope and that indeed the particle in question is SBV. The grid was extensively searched for potential SBV vesicles and particles were found decorated with a range of gold fiducials between 1 and 5. Despite the strong background contrast along with the presence of other vesicles and protein contaminants, Figure 39 shows particles found with nearby 4 and 5 nanogolds.

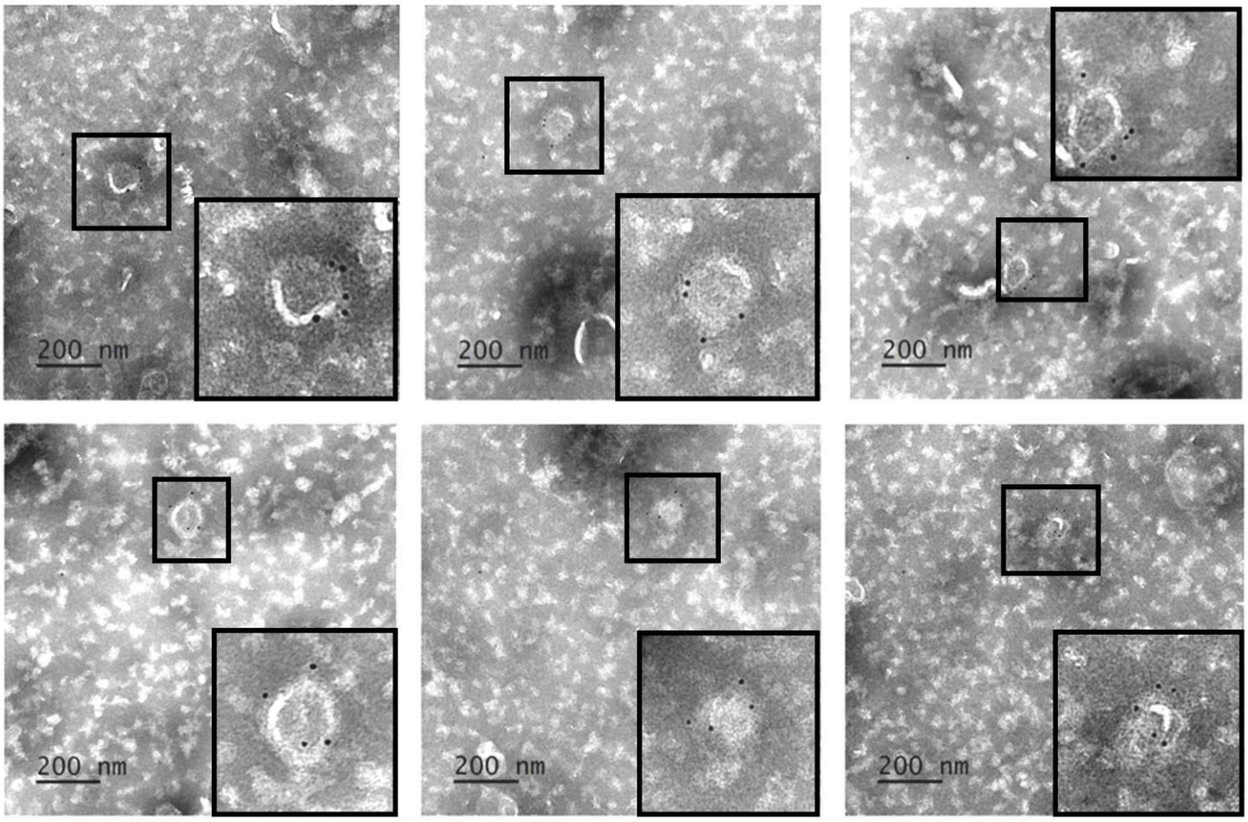

Figure 39. Immunolabelling of viral particles from Purification III. Fraction 11 of *Purification III* was dialysed in NTE buffer and placed of top of glow discharged carbon coated copper grids. Incubation was done with anti-G_C Ab 5F12 and further anti-mouse 10 nm gold fiducials conjugated Ab. Staining was obtained with two 30 seconds incubations with U2% UAc. SBV size matching particles (80-110 nm) were decorated with 4 and 5 fiducials per particle. Dashed lines squares indicate the SBV particles zoomed in the corner or the micrographs. Images retrieved at 30k magnification with a Jeol JEM1230 operating at 120kv in a ΔZ range of -2.5 and -3.5 μm.

III. Further batches of discontinuous gradient purification

Encouraged by the imaging results obtained by the negative stain immunolabeling the next purifications were carried out using a discontinuous gradient. In Purification III, the gradient was continuous between fractions 1 (15 % Optiprep™, ρ = 1.084 g/mL) and 19 (30 % Optiprep™, ρ = 1.163 g/mL). The highest viral titer was obtained at the fraction 11, with an approximate value of ρ of 1.129 g/mL. Moreover, in Purification I and II protocols, the highest viral titers were found at the interface between 20/25% (Purification I) and 25% (Purification II), regions with ρ Optiprep™ values of approximately 1.121 and 1.131 g/mL.

In the light of the above results, we devised the *Purification IV* protocol that presented an additional layer of 22.5% Optiprep™ (ρ = 1.121 g/mL) at the ¨buoyant separation step¨. This was a new attempt to both concentrate the virus in order to obtain workable titers for EM data collection and prevent a great loss of purity. Also, a slightly higher number of BHK cells were infected for viral propagation ($3.6x10^8$). Now, the fraction 5 was the one with the strongest signal in immunoblot and with the highest titer (1.5×10^8 particles/mL) (Figure 40A).

The first dialysis step applied on 30% Optiprep™ cushions, done in all initial purification protocols (I-IV), always resulted in a slightly loss of infectivity of the particles as whole. Previous TCID50 calculations with Optiprep™ cushions samples from Purification III before and after dialysis have shown a decrease of the titers of the order of $10^{0.5}$. Interestingly, this decreased titer was not accompanied by a raise of the volumes by using the Float-A-lyzer G2 dialysis devices (Spectra/Por®). In *Purification V,* the Optiprep™ cushions were diluted in NTE buffer instead of being dialysed after the ¨preliminary purification step¨ (details given in the Materials and Methods section). The strongest signal of the immunoblot from this protocol was once again at the ρ=1.121 g/mL interface (fraction 5) with a titer of 2×10^8 particles/mL (Figure 40B).

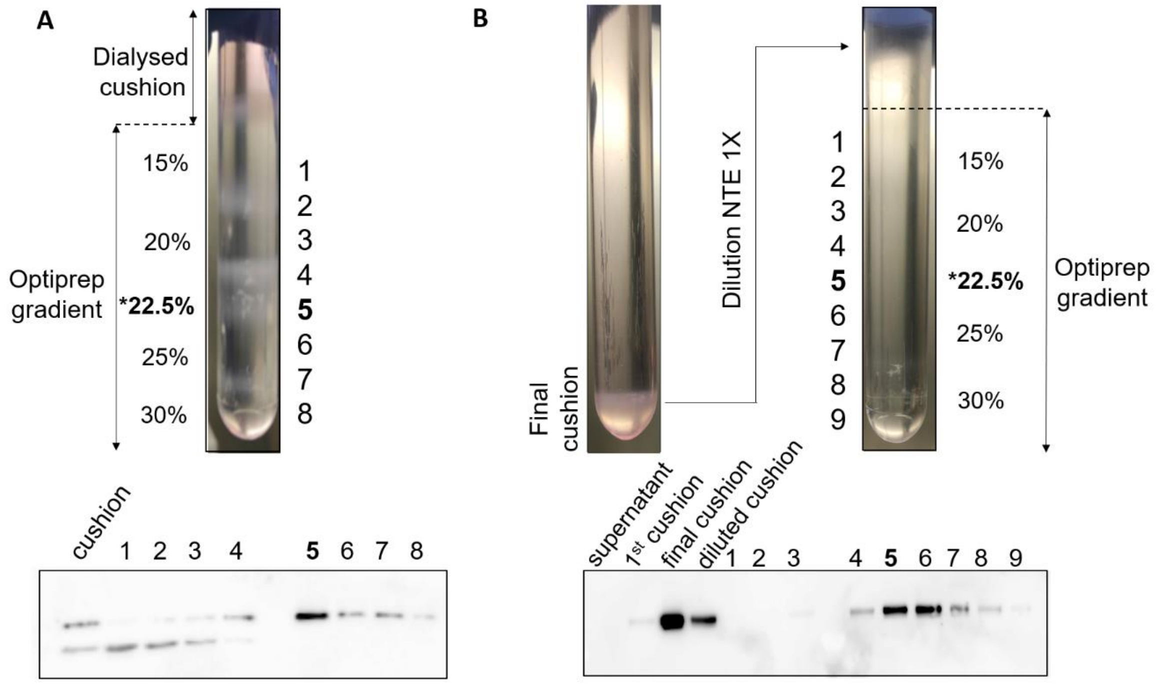

Figure 40. Outcomes of the addition of an extra 22.5% Optiprep$^{\mathrm{TM}}$ layer at the separation gradient. **(A)** *Purification IV.* Top: ρ gradient with the dialysed cushion loaded on top, ρ=1.121 g/mL step (22.5%) corresponding fraction (5) is shown in bold. Bottom: Immunoblot with cushion and corresponding separation fractions in each layer. **(B)** *Purification V***.** Top: Preliminary purification step with the final cushion (0.5 mL) at the bottom of the tube and following ρ gradient with the diluted cushion loaded on top, ρ=1.121 g/mL step (22.5%) corresponding fraction (5) is shown in bold. Bottom: Immunoblot with preliminary purification samples and corresponding separation fractions in each layer.

Despite the apparent improvement in terms of concentration of the particles at the 22.5% Optiprep$^{\mathrm{TM}}$ (ρ=1.121 g/mL) interface, when the samples were imaged by negative stain immunolabelling a poor level of particle decoration was noted.

Negative stain from fractions 5 of Purifications IV and V also included a fixing step with 0.2% glutaraldehyde and 0.2 M glycine neutralization. Alternatively, negative stain immunolabelling without glutaraldehyde fixing steps were tested as well. Apart from 2% UAc (w/v), Methylamine Vanadate (Nanovan®) was also tested for the staining. Putative SBV particles, based on their sizes, were detected but without any anti-G$_C$+anti-mouse nanogold decoration in the fraction 5 of both Purifications IV and V (Figures 41-42).

Due to the consistent results from Purification III, samples derived from this protocol were used in further steps of cryo-EM data collection aiming 2D analyses of the viral spikes, as shown in the further sections of the thesis.

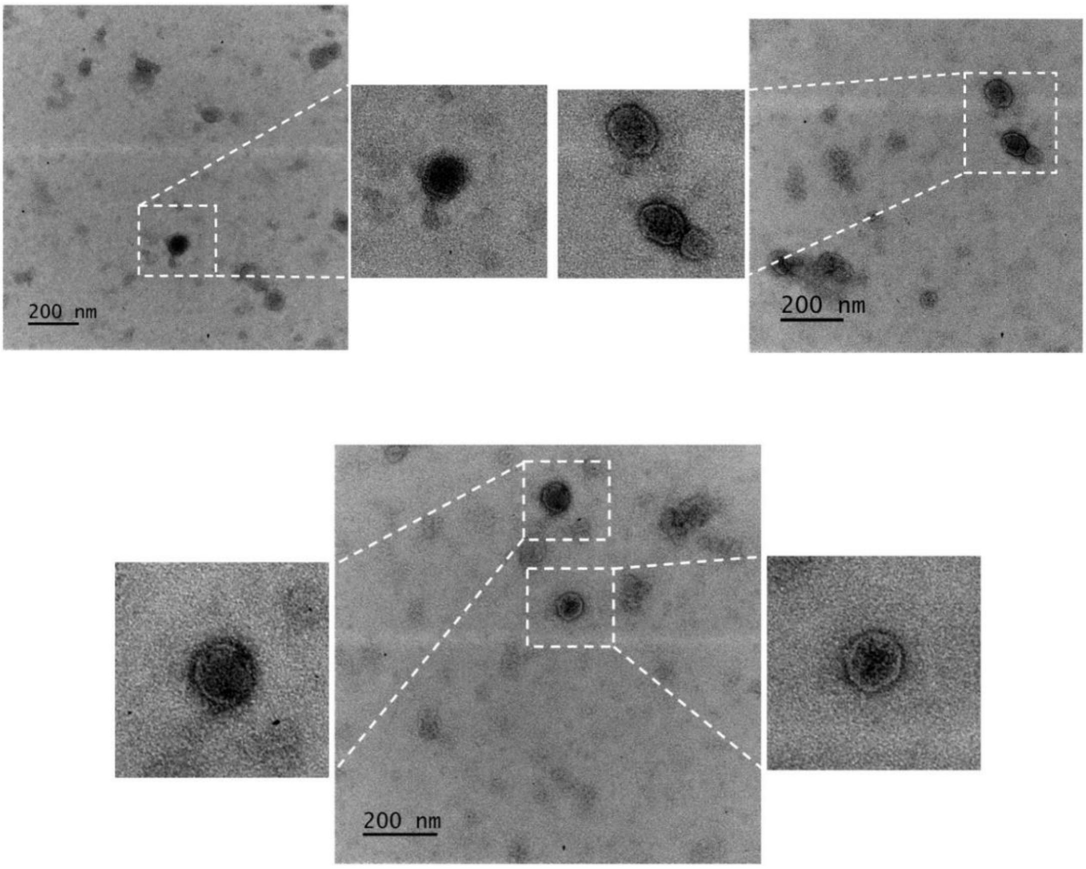

Figure 41. Negative stain from Purification IV. Fraction 5 of Purification IV was dialysed and was placed on top of glow discharged carbon coated copper grids. Fixing was achieved with 0.2% glutaraldehyde and 0.2 M glycine neutralization. Incubation was done with with anti-G_C Ab 5F12 and further anti-mouse 10 nm gold fiducials conjugated Ab. Staining was obtained with two 30 seconds incubations with Methylamine Vanadate (Nanovan®). SBV size matching particles (80-110 nm) were successfully stained but had no anti-G_C+anti-mouse nanogold decoration. White dashed lines squares indicate the putative SBV particles zoomed out of the micrographs. Images acquired with a Jeol JEM1230 Transmission EM operating at 120 Kv, images had 30k magnification. ΔZ applied was -2.5 μm.

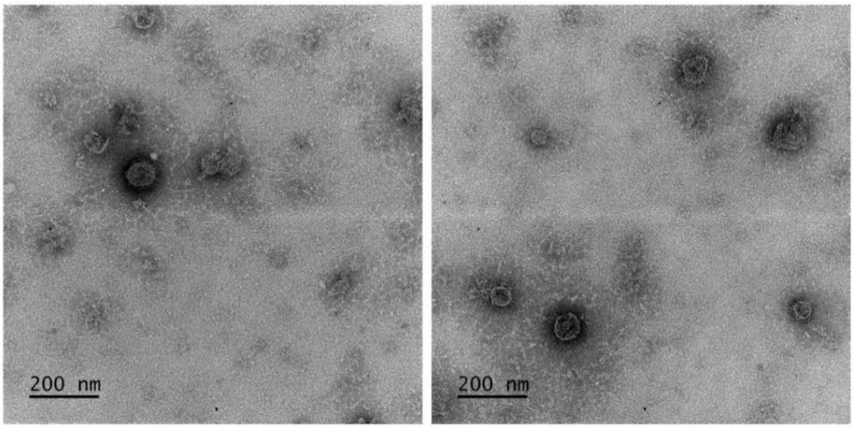

Figure 42. Negative stain from Purification V. Fraction 5 of Purification V was dialysed and placed on top of glow discharged carbon coated copper grids. Fixing was achieved with 0.2% glutaraldehyde and 0.2 M glycine neutralization. Incubation was done with anti-G_C Ab 5F12 and further anti-mouse 10 nm gold fiducials conjugated Ab. Staining was obtained with two 30´ incubations with Uranyl Acetate. SBV size matching particles (80-110 nm) were successfully stained but had no anti-G_C+anti-mouse nanogold decoration. White dashed lines squares indicate the putative SBV particles zoomed out of the micrographs. Images acquired with a Jeol JEM1230 Transmission EM operating at 120 Kv, images had 30k magnification. ΔZ applied was -3 μm.

IV. SBV particles images by cryo-EM

In the light of the different SBV particles purification protocols presented, we visualised samples from Purification III which were positive for negative stain immunolabelling. As expected, due to the viral titer of 10^8 (relatively low for cryo-EM automatic data collection) SBV particles had to be extensively searched at a low magnification in order to be found. Still, particles with the correct size range (80-110 nm diameter) were present. Most importantly, they appeared to display an ordered ¨crowning¨ of repetitive, presumably proteinaceous, entities on the top of the viral envelope. Finally, a densely contrasted interior of such particles should correspond to the RNPs. (Figure 43).

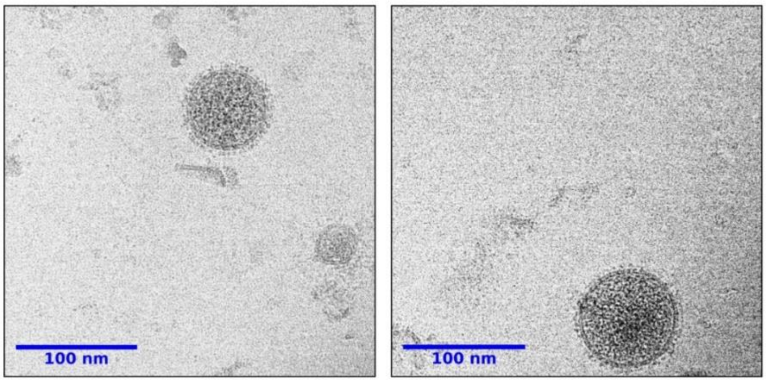

Figure 43. Cryo-EM images of SBV particles obtained at Purification III. Sample were loaded on top of carbon coated Cu 200 R 2/2 grids and plunge frozen in liquid ethane. Images were retrieved at a JEM 2200FS transmission EM operating at 200 kV, at 30k magnification and a ΔZ range of -2.0/-3.0 µm. Scaling was done on FIJI (198). Densely packed particles within SBV size range (80-110 nm) are seen decorated on top of the lipid membrane by the putative G_C/G_N glycoprotein spike.

Next, 10 nm gold fiducials were added to the samples (1:16 v:v proportion) aiming for a cryo-ET data collection. During the process of vitrification, 2 µL of sample was pipetted on top of the grid following a 10 seconds interval (total 6 µL of sample added). This was repeated three times before plunge freezing the grid into liquid ethane as an attempt to concentrate the virus. Again, SBV particles were scarce but present and with the putative glycoprotein spike decoration. SBV particles that fulfilled the criteria of being (i) around the correct size range; (ii) densely packed (containing high contrasted putative RNPs densities inside the bilayer) and (iii) decorated on top of their envelopes with densities that should correspond to the G_N/G_C glycoprotein spike were imaged. In total, 13 micrographs were collected, 6 of which are depicted in Figure 44.

LAS PAGINAS 113 A 129 ESTAN SUJETAS A CONFIDENCIALIDAD POR EL AUTOR

Chapter 5:

DISCUSSION

I. A small fragment of the SBV-N highly conserved across the *Orthobunyaviruses* of the Simbu serogroup protects SBV challenged IFNAR$^{-/-}$ mice

Viruses from the *Orthobunyavirus* genus from the *Peribunyaviridae* family are constantly being identified, having the number of catalogued species reached 87 in 2019 according to the ICTV (14,15). By being an arbovirus, it is plausible to link the emergence of new species to the human action in climate change, particularly on deforestation of large areas and cattle farming, favouring either directly or indirectly the constant dissemination of the insect vectors (16,52,53). Remarkably, SBV was initially restricted to Europe and has already reached eastern-Asia: antibodies against it were detected in cattle farms from China in 2018 for example (45). Moreover, African countries such as Namibia in 2018 (46), South Africa in 2021 (50) and most recently Uganda in 2022 (229) have also reported SBV circulation in their territories.

The emergence of new viruses poses the quest of vaccines capable of generating a cross-reactive immunity. Surface viral glycoproteins are highly immunogenic and logically the first choice as potential vaccine prototypes (230). However, these vaccines often require updated formulation as viral glycoproteins are under high immune and environmental pressures. Differently, viral nucleoproteins interact with the viral genome forming the densely packed RNPs and fill the interior of the virions. Consequently, this proteins are less exposed and thus are regarded as more conservative targets (231).

In this sense, nucleoproteins of viruses belonging to different families have been pointed as effectors of IFN-γ^+ CD8$^+$ T cell responses: Human Influenza A (fam. *Orthomyxoviridae*) (232); LASV (fam. *Arenaviridae*) (233); Ebolavirus (fam. *Filoviridae*) (234); CCHFV (fam. *Nairoviridae*) (235,236) and RVFV (fam. *Phenuiviridae*) (237-239). However, the investigation of nucleoproteins as possible immunogens against members of the *Orthobunyavirus* genus from the *Peribunyaviridae* family remains limited.

Our present research focuses on determining a minimal polypeptide chain of the *Orthobunyavirus* SBV nucleoprotein capable to confer protection to IFNAR$^{-/-}$ mice when challenged with a SBV virulent strain. This quest emerges from the fact that smaller antigenic polypeptides are better suited for the nanovaccine technology. Proteinaceous nanoparticles can be used as platforms by harbouring repetitive array of antigens on the particle surface, which improves considerably antigen presenting cell uptake and naïve cell activation (240).

Previous studies showed that both SBV-N cDNA and the protein itself can serve as candidate vaccines against SBV infection by eliciting a cell-mediated immune response (69,70). Now, we tested progressively smaller protein fragments, each with a sequence nested within the previous larger one (N-terminal, C2, C3 and C4). The protein design was inspired by the SBV-N crystal structure and its secondary structure organization (105).

We show that the minimal fragment conferring protection is the polypeptide comprising residues from Met1 to Ala58 (C4) of the SBV-N. To sustain this result, different proteins were administrated with the adjuvant Quil-A saponin to IFNAR$^{-/-}$ mice subsequently infected with a virulent strain of SBV (BH619/12-7). The C4 immunized group re-gained weight after 5 dpi and showed a higher percentage of surviving mice after 14 dpi when compared to control groups: 86% (C4 immunized) *versus* 60% (not immunized) and 29% (GST immunized). Also, quantification of viraemia and ELISA assay for detection of secreted IFN-γ demonstrated that C4 + Saponin was able to dampen viral replication and to generate a CD8^{+} IFN-γ^{+} cell mediated immunity.

Another group, immunized with the SBV N-term fragment (Met1-Thr133) and subsequently infected with SBV remained practically healthy and with an increased ability to clear the virus as shown by the viraemia quantification results. However, the N-term region is 75 residues longer than the C4 fragment and approximately half of the full nucleoprotein sequence itself. Indeed, the full SBV-N has been shown to clear SBV RNA after 10 dpi (70) while our current study shows a decrease in viraemia by an order of 10 and $10^{1.5}$ for the C4 and N-term candidate vaccines, respectively, within this same period. Nonetheless, the health and weight assessment of the animals, combined to the N-term mediated splenocytes re-stimulation for IFN-γ secretion and C4 mediated CD8^{+} T cell re-stimulation assays support those shorter polypeptides to be capable of mediating a protective immune response.

Our current findings also highlight the contrasting interference that GST and GFP, used in a previous study (70), impacted of detection of IFN-γ. The percentage of animals that died in the control groups were also higher (71% and 60% of the GST and non-vaccinated controls compared to 25%, 50% and 20% of dead animals for the GFP, Saponin and PBS controls).

It's worth mentioning that a basal IFN-γ was detected in different negative controls utilized in the present work, both on C57BL/6 and IFNAR$^{-/-}$ derived splenocytes supernatants. It was already reported that IFN-γ production is ascribed to several immune cell types such as T lymphocytes, macrophages, natural killers, and dendritic cells. Moreover, GST has the ability to stimulate IFN production in CD4⁺ T cells (241). Considering, for example, the non-expanded CD8⁺/CD107⁺ populations in GST immunized C57BL/6 mice, the observed IFN-γ secretion could be produced by other cell populations rather than CD8⁺ T cells.

The Simbu serogroup of *Orthobunyaviruses* includes SBV along with several other pathogens of veterinary and medical importance such as the animal-infecting AKV and SHAV and human-infecting OROV (242,243). The former animal-infecting viruses are known to reassort, an event occurring when they co-infect the same cell although only for a limited time frame (244).

Comparison of nucleoprotein sequences across several members of the Simbu serogroup shows a high degree of homology ranging from 80 to 100% identity within the first 58 residues of SBV nucleoprotein (C4 fragment). A lower identity value was obtained when SBV-N was compared to the human pathogens OROV (70%) and the California serogroup LACV (38%). The average identity of C4 with the corresponding regions of all the analysed Simbu serogroup nucleoproteins is 87.1% whereas for the full SBV-N and N-term fragment the corresponding identities slightly decrease to 84.3% and 84.9%, respectively.

Taking all the previously shown results together, we propose that the C4 fragment, properly adjuvanted with Quil-A Saponin, could be used as pan-immunogen against Simbu serogroup viruses (Figure 59).

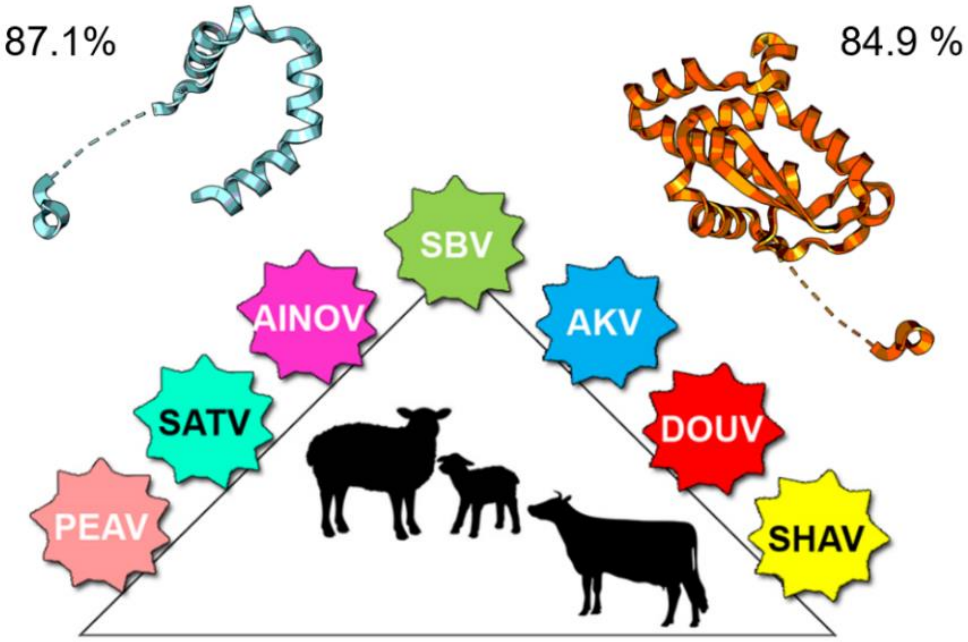

Figure 59. A possible pan-vaccine harbouring C4 might be protective against several members of the Simbu serogroup. Cartoon representations of SBV-N C4 (cyan) and N-terminal (orange) followed by their corresponding mean values of homology against the analysed members of the Simbu serogroup corresponding nucleoprotein regions. Simbu serotype *Orthobunyavirus* are depicted as shadows. SBV Schmallenberg virus, in green; AINOV Aino virus, in pink; AKV Akabane virus, in blue; SATV Sathuperi virus in dark cyan, DOUV Douglas virus, in red; PEAV Peaton virus, in salmon; SHAV Shamonda virus, in yellow.

This same idea was recently reported for Influenza: Based on an evolutionary conserved region of its nucleoprotein (aa. 137-182), a universal vaccine against flu infection was proposed earlier in 2022, since this region was capable to raise virus-specific TCD8+ responses in mice (245).

Our efforts in restricting the region of the SBV nucleoprotein capable to protect mice from SBV infection are driven by the generation of biologics that could be readily implemented in nanovaccine technology: smaller fragments will present less steric hindrance when posed onto an array increasing the packing decoration and thus prime the nanoparticle for a strong immune response.

Currently, the smallest protective region(s) within the nucleoprotein (the exact MHC-I epitope(s) from C4/SBV-N) are unknown, as shown by both attempts with peptides P1-P7 and P. I-P. IX on re-stimulating a TCD8+ response. Still, the evolutionary sequence conservation of the SBV C4 portion of the nucleoprotein across other viruses of the Simbu serogroup might constitute the cornerstone for developing nanoparticles vaccine with potential cross-protective properties.

II. A Preliminary morphological characterization of SBV using cryo-EM

The envelope of SBV is decorated by the glycoproteins G_N and G_C as in the case of other *Peribunyaviruses.* Such proteins play crucial roles both in the assembly of the virions and in the virus-cell entry mechanism, apart from being intrinsic tropism restriction factors (79). However, the limited structural knowledge not only regarding SBV but also other *Orthobunyaviruses* constitutes a bottleneck for the rational design of drugs and vaccines. This situation would be ameliorated by a better understanding of viral protein structures and function, particularly those that constitute the viral spikes (246).

The outward-oriented domains of the lipidic envelope anchored glycoproteins are the protagonists in the attachment of the virus into the host cell. These proteins are extremely variable in terms of structural organization among different viral families (246). This broad variety is directly translated into the wide range of host receptors utilized for cell binding among *Orthobunyaviruses* e.g., DC-SIGN for the California serogroup LACV (112) and HSPG for the Simbu serogroup AKV and SBV (85), to name a few. The latter linking between AKV and SBV cell primary attachment to HSPG was already stated to be still pending on the full G_C/G_N spike structure to be resolved: then, the binding site(s) from the spike to the HSPG could be properly addressed (87).

Besides, the *Peribunyaviruses* glycoprotein spikes constitute the prime targets of the immune system defenses, enclosing the main epitopes of neutralizing antibodies (NAbs) (79,92). This was already demonstrated specifically for SBV (92). Thus, such viral features are key targets for vaccine development, and the understanding and further engineering of optimal antigens aiming for a strong immune response is a fundamental aspect for the efficiency of a vaccine prototype (247).

Here, we had as an initial goal the improvement of SBV particles production protocols necessary for structural studies by cryo-ET. Specifically, being able to raise the titer outcomes from the purifications would directly improve the EM data collection e.g., by allowing automatic and semi-automatic methodologies to be implemented (248). In this case images would be collected without the need of exhaustively searching for the virions at low magnifications.

All purification results showed dispersion of possible viral particles through the density gradient. The different layers from the Optiprep^{TM} gradient retrieved a signal in immunoblot experiments using an anti-G_C Ab as a primary, which indicates the presence of G_C in SBV mature virions presumably with different ρ values. This was already expected given the nature of the virus. It was already described that in the process of RNPs packaging, SBV particles can harbour its three genomic segments, distinct combinations of them or even no genome at all, requiring the latter co-infection with full genome packed particles to properly infect the cells (100).

As already mentioned, we cannot rule out the presence of broken particles or vesicles that are not necessarily mature SBV virions but contain the G_C protein embedded in their membranes. All of the latter, in this case, could have been pooled together with mature virions (undoubtedly present as showed by positive CPE in TCID50 BHK cells assays). *Purification III* (titer 3.11 x 10^8 virions/mL), in which a continuous Iodixanol was used for the ¨buoyant separation step¨, retrieved the best outcomes principally for allowing positive immunolabeling decoration of the virions.

A possible explanation for the lack of anti-G_C labelling derived from *Purifications IV* and *V* might be due to low concentration of virus. Fractions 5 from *Purifications IV* and *V* presented 1.5 and 2 x 10^8 virions/mL, respectively. On the other hand, 3.11 x 10^8 virions/mL were obtained from the Fraction 11 of *Purification III* that could be labelled with the anti-G_C Ab. Also, the fixing steps could interfere with the binding of the Abs to the spikes. If this is the case, the % of glutaraldehyde might have been too high to the point of being deleterious. Still, SBV particles coming from *Purification IV* were also attempted to be labelled without any fixing steps, again without success.

Alternatively, the 5F12 anti-G_C Ab could not have been working properly. *Purifications III* and *IV/V* were done with a 3 months gap and after the negative result on the labelling of *Purification IV*, new aliquots of 5F12 were kindly provided by our collaborators from Insel Riems, Germany. Despite the new Abs batch utilized, the labelling of samples from *Purification V* was still negative.

We cannot exclude that *Purifications IV* and *V* do not separate the virus as well as *Purification III*, in which, as already mentioned, a continuous Optiprep™ gradient was utilized. However, both the presence of a strong immunoblot band and noticeable titers from TCID50 plates, especially the latter, support the presence of viruses in such samples.

2-D side view projections are valuable tools to provide an initial morphological information (186). Neuman and colleagues for example utilized this kind of analysis to describe distinct configurations of the M protein from Severe Acute Respiratory Syndrome Virus (249). In our analysis, the densities on top of the bilayers from SBV particles provided an initial average from the spike complex of approx. 5-7 nm, between two and three times shorter than the BUNV spike (18 nm) (110). This discrepancy in size can even be seen without any classifications when both particles are sided (Figure 60).

Bowden and colleagues also present a spike configuration at the post-fusion state by vitrifying the BUNV samples into an acidic pH. Such environment resulted in a clear alteration of the interconnecting protein lattice, that was disrupted, impairing clear visualization of the outermost regions of the spikes (Head/Stalk) (110). Our SBV samples, however, were solely maintained in pH 8.0 and presumably the spikes should only adopt pre-fusion states of organization.

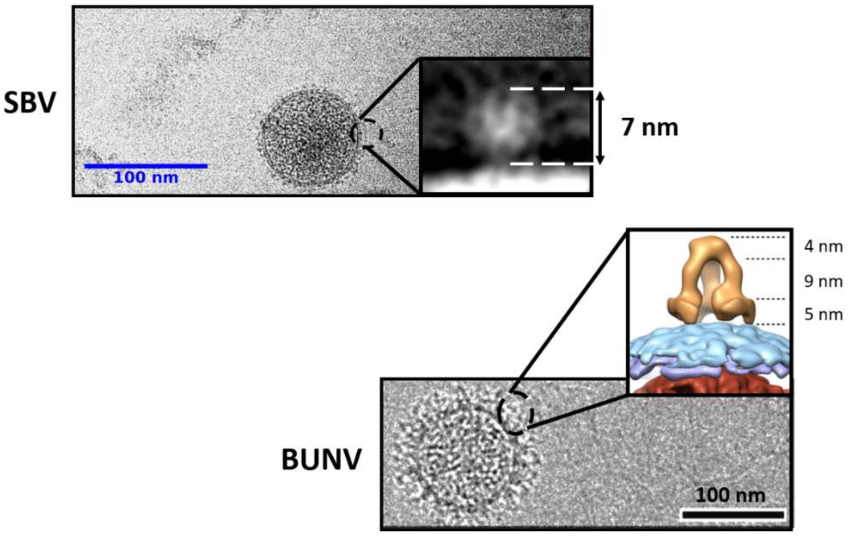

Figure 60. Comparison of SBV and BUNV spikes. Top: Cryo images of SBV particles from the presented results, sided with the 2-D average of the densities present on top of the lipidic bilayer. Bottom: BUNV particles and final spike structure as presented by Bowden *et al.* 2013.

Next, a preliminary cryo-ET characterization of the SBV G_C/G_N spike complex was achieved. After distinct STA pipelines, high density layers were retrieved. Our preliminary estimations show that such features are approx. 4.2-6.3 nm distal from the viral envelope densities (considering the number 4 density layer from preliminary averages drawn from *Datasets A-D*, all with sub tomograms that had 27.8 x 27.8 x 27.8 nm^3 volumes (Figure 61).

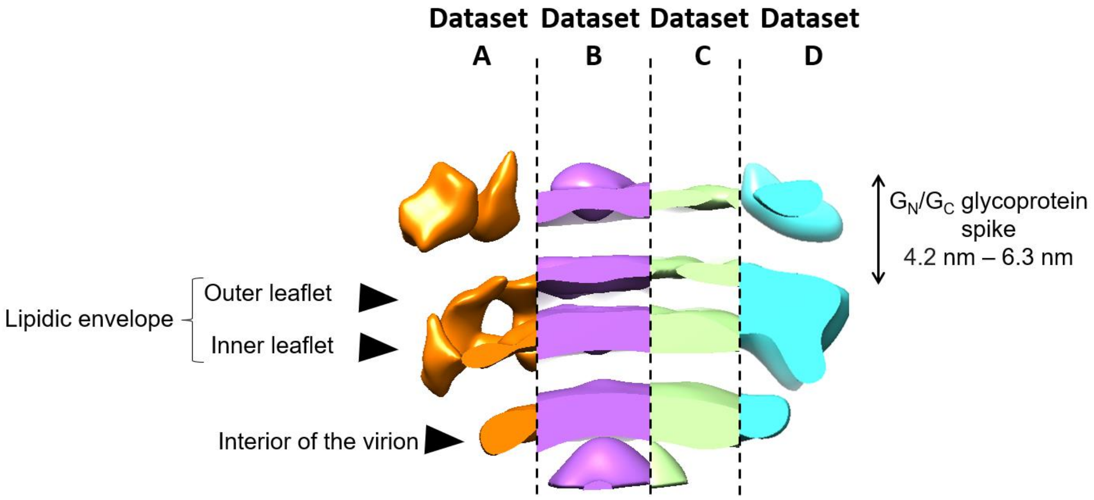

Figure 61. Preliminary STA results from *Datasets A-D*. Superposition from the distinct STA resulting volumes from the manually (*Dataset A*), vesicle model (*Datasets B and C*) and dipole model (*Dataset D*) extracted sub-tomograms with 27.8 x 27.8 x 27.8 nm^3 volumes. Averaged densities corresponding to the outer and inner leaflets of the lipidic envelope and the interior of the virion are depicted with black arrow heads. The range of the G_N/G_C glycoprotein spike height starting from the outer leaflet of the distinct averages is shown in the right. Volumes displayed with Chimera (227).

Cryo-ET analysis from BUNV have previously pointed out the region between the RNP internal core and the lower leaflet of the lipidic membrane as a region with low contrast, and more importantly, with a lower contrast than the one observed for its lipid bilayer (110). This could both be explained by this region being composed mainly of motifs of the long G_N cytoplasmic tails (55 aa residues in the case of BUNV) that do not interact with RNPs (100). The envelope, on the other hand, comprehends both the lipids and the array of transmembrane helices from G_N and G_C (78). If the results on *Datasets A-D* are in frame with the prior statements, the density corresponding to the interior of the virion (number 1) would be approx. 3.7-5.1 nm away from the lower leaflet of the viral membrane (number 2).

Dataset E particles were picked with larger dimensions (44.4 x 44.4 x 44.4 nm^3 volume). For this reason, extra care must be taken on trying to correlate the now 5 layers of high density obtained at the resulting average volume with SBV structural features. By being a result of STA from larger sub tomograms than the previous datasets particles (*Datasets A-D*, with 27.8 x 27.8 x 27-8 nm^3 particles), *Dataset E* sub-tomograms presumably harbour much more densities coming from the interior of the viral particles.

Bowden and colleagues, at a radial density analysis from BUNV tomograms, show that the inner core of this virus presents at least three regions of high density, separated by approx. 8 nm among themselves. Such regions are pointed by the authors as probably corresponding to interactions from the nucleoprotein oligomers with the RNA and the cytoplasmic tail of G_N (110). Thus, the high-density layers obtained at the *Dataset E* average volume might correspond to an alignment of one or more regions within the densely packed SBV RNP core. In such scenario, the SBV interior would present itself similarly to the observed in BUNV, although the heights between high density sections in this case are always shorter than 8 nm.

The height of the uppermost densities in *Datasets A-D* (numbered as 4) was estimated to be between 4.2 and 6.3 nm, this region corresponds to the SBV G_C/G_N spike. Most importantly (i) these values are in line with the ones observed for the 2-D analyses as a whole (4.2-5.0 nm from the radial densities and 7 nm from the 2-D classifications) and (ii) altogether, the results point out that SBV spike is undoubtedly shorter than the BUNV spike (18 nm) (110).

The morphological results from the present work, although represent an advance in our current knowledge of the SBV structure are still in an early phase. For this reason, conclusions can be drawn only regarding the general architecture of the SBV spike at the present moment. One could speculate that, if SBV indeed adopts a similar configuration of BUNV, the previously mentioned 4.2-6.3 nm high density regions could correspond to the G_N/G_C crowded floor region of BUNV (approx. 5 nm) (110). However, in the study by Bowden and colleagues in the BUNV particles, the authors cannot discard that more configurations of the spike are present on the virions' envelope apart from the 3D reconstructed trimers (e.g., G_C/G_N monomers) (110); a possible situation also for SBV. Taken together, our preliminary structural results point out that SBV G_C/G_N spikes do not follow the same organization as BUNV, as previously thought. We describe the SBV spike complex as being shorter in height and presumably more compact than BUNVs, ranging from 4 to 7 nm. Finally, a larger dataset and further data processing are highly needed in order to narrow down the findings presented, ultimately leading to the final architecture of the SBV spikes.

Tackling pleomorphic viruses' structures remains a challenge. Still, our current work might give an initial insight into the spike architecture of SBV. To note, no SBV production methodologies nor cryo-ET derived images of the whole virions and from the G_C/G_N glycoproteins are available in the literature. Thus, altogether, the current novel results allow an initial description of the SBV virions and its viral spike complexes and contribute to expand the current knowledge on SBV: vital prerequisites to ultimately implement new strategies for viral control since the G_C/G_N spike is the prime gateway for viral infection.

Chapter 6:

CONCLUSIONS AND PERSPECTIVES

I. The N-terminal (Met1-Thr133) and C4 (Met1-Ala58) proteinaceous fragments of SBV-N proved themselves as promising vaccine prototypes against SBV infection by means of extensive immunological assays utilizing SBV challenged IFNAR$^{-/-}$ mice model. These results open the door for further testing in larger ruminants and engineering nanoparticles with these proteins.

II. Based on the observed high sequence conservation with other *Orthobunyaviruses* from the Simbu serogroup, specifically regarding the Nucleoprotein N-terminal extremity (C4 from SBV-N), show that this fragment might be used as a ¨pan-vaccine¨ prototype. This study paves the way to nanovaccine formulation and testing in large ruminants across different viruses of the Simbu serogroup.

III. An improved systematic protocol for SBV particles purification was successfully established and implemented, which allowed further characterization of the viral morphology.

IV. Our 2D and 3D analyses by means of SPA and STA respectively have elucidated a preliminary, and yet novel, characterization of the SBV spike decorating the viral lipidic bilayer. Our results suggest a possible alternative conformation when compared to the close related BUNV: The SBV spike is, in principle, shorter, which would mean a possible novel arrangement of the G_C and G_N glycoproteins with respect to the BUNV tripodal spike previously described. These results support a feasible characterization of the SBV spike complexes, specifically by means of STA.

Bibliography

1. Lefkowitz EJ, Dempsey DM, Hendrickson RC, Orton RJ, Siddell SG, Smith DB. Virus taxonomy: the database of the International Committee on Taxonomy of Viruses (ICTV). Nucleic Acids Res. 2018 Jan 4;46(D1):D708-D717. doi: 10.1093/nar/gkx932. PMID: 29040670; PMCID: PMC5753373.

2. Hughes HR, Adkins S, Alkhovskiy S, Beer M, Blair C, Calisher CH, Drebot M, Lambert AJ, de Souza WM, Marklewitz M, Nunes MRT, Shí 石晓宏 X, Ictv Report Consortium. ICTV Virus Taxonomy Profile: *Peribunyaviridae*. J Gen Virol. 2020 Jan;101(1):1-2. doi: 10.1099/jgv.0.001365. PMID: 31846417; PMCID: PMC7414433.

3. Maes P, Alkhovsky SV, Bào Y, Beer M. et al. Taxonomy of the family Arenaviridae and the order Bunyavirales: update 2018. Arch Virol. 2018 Aug;163(8):2295-2310. doi: 10.1007/s00705-018-3843-5. Epub 2018 Apr 21. PMID: 29680923.

4. Dutuze MF, Nzayirambaho M, Mores CN, Christofferson RC. A Review of Bunyamwera, Batai, and Ngari Viruses: Understudied *Orthobunyaviruses* With Potential One Health Implications. Front Vet Sci. 2018 Apr 12;5:69. doi: 10.3389/fvets.2018.00069. PMID: 29707545; PMCID: PMC5906542.

5. Leventhal SS, Wilson D, Feldmann H, Hawman DW. A Look into *Bunyavirales* Genomes: Functions of Non-Structural (NS) Proteins. *Viruses*. 2021;13(2):314. Published 2021 Feb 18. doi:10.3390/v13020314

6. Saeed MF, Li L, Wang H, Weaver SC, Barrett ADT. Phylogeny of the Simbu serogroup of the genus Bunyavirus. J Gen Virol. 2001 Sep;82(Pt 9):2173-2181. doi: 10.1099/0022-1317-82-9-2173. PMID: 11514727.

7. Sakkas H, Bozidis P, Franks A, Papadopoulou C. Oropouche Fever: A Review. Viruses. 2018 Apr 4;10(4):175. doi: 10.3390/v10040175. PMID: 29617280; PMCID: PMC5923469.

8. Borucki MK, Kempf BJ, Blitvich BJ, Blair CD, Beaty BJ. La Crosse virus: replication in vertebrate and invertebrate hosts. Microbes Infect. 2002 Mar;4(3):341-50. doi: 10.1016/s1286-4579(02)01547-2. PMID: 11909745.

9. Charles JA. Akabane virus. Vet Clin North Am Food Anim Pract. 1994 Nov;10(3):525-46. doi: 10.1016/s0749-0720(15)30537-5. PMID: 7728635.

10. De Regge N. Akabane, Aino and Schmallenberg virus-where do we stand and what do we know about the role of domestic ruminant hosts and Culicoides vectors in virus transmission and overwintering? Curr Opin Virol. 2017 Dec;27:15-30. doi: 10.1016/j.coviro.2017.10.004. Epub 2017 Nov 6. PMID: 29096232.

11. Ali H, Ali AA, Atta MS, Cepica A. Common, emerging, vector-borne and infrequent abortogenic virus infections of cattle. Transbound Emerg Dis. 2012 Feb;59(1):11-25. doi: 10.1111/j.1865-1682.2011.01240.x. Epub 2011 Jul 7. PMID: 21733134.

LAS PAGINAS 142 A 147 ESTAN SUJETAS A CONFIDENCIALIDAD POR EL AUTOR

peptidase. Proc Natl Acad Sci U S A. 2016 Aug 2;113(31):8825-30. doi: 10.1073/pnas.1603364113. Epub 2016 Jul 20. PMID: 27439867; PMCID: PMC4978261.

79. Hulswit RJG, Paesen GC, Bowden TA, Shi X. Recent Advances in Bunyavirus Glycoprotein Research: Precursor Processing, Receptor Binding and Structure. Viruses. 2021 Feb 23;13(2):353. doi: 10.3390/v13020353. PMID: 33672327; PMCID: PMC7926653.

80. Kobayashi T, Yanase T, Yamakawa M, Kato T, Yoshida K, Tsuda T. Genetic diversity and reassortments among Akabane virus field isolates. Virus Res. 2007 Dec;130(1-2):162-71. doi: 10.1016/j.virusres.2007.06.007. Epub 2007 Jul 30. PMID: 17659802.

81. Coupeau D, Claine F, Wiggers L, Kirschvink N, Muylkens B. In vivo and in vitro identification of a hypervariable region in Schmallenberg virus. J Gen Virol. 2013 Jun;94(Pt 6):1168-1174. doi: 10.1099/vir.0.051821-0. Epub 2013 Jan 30. PMID: 23364190.

82. Fischer M, Hoffmann B, Goller KV, Höper D, Wernike K, Beer M. A mutation 'hot spot' in the Schmallenberg virus M segment. J Gen Virol. 2013 Jun;94(Pt 6):1161-1167. doi: 10.1099/vir.0.049908-0. Epub 2013 Jan 30. PMID: 23364189.

83. Doceul V, Lara E, Sailleau C, Belbis et al. Epidemiology, molecular virology and diagnostics of Schmallenberg virus, an emerging orthobunyavirus in Europe. Vet Res. 2013 May 15;44(1):31. doi: 10.1186/1297-9716-44-31. PMID: 23675914; PMCID: PMC3663787.

84. Elliott RM, Blakqori G, van Knippenberg IC, Koudriakova E, Li P, McLees A, Shi X, Szemiel AM. Establishment of a reverse genetics system for Schmallenberg virus, a newly emerged orthobunyavirus in Europe. J Gen Virol. 2013 Apr;94(Pt 4):851-859. doi: 10.1099/vir.0.049981-0. Epub 2012 Dec 19. PMID: 23255627; PMCID: PMC3709688.

85. Maginnis MS. Virus-Receptor Interactions: The Key to Cellular Invasion. J Mol Biol. 2018 Aug 17;430(17):2590-2611. doi: 10.1016/j.jmb.2018.06.024. Epub 2018 Jun 18. PMID: 29924965; PMCID: PMC6083867

86. Windhaber S, Xin Q, Lozach PY. Orthobunyaviruses: From Virus Binding to Penetration into Mammalian Host Cells. Viruses. 2021 May 10;13(5):872. doi: 10.3390/v13050872. PMID: 34068494; PMCID: PMC8151349.

87. Murakami S, Takenaka-Uema A, Kobayashi T, Kato K, Shimojima M, Palmarini M, Horimoto T. Heparan Sulfate Proteoglycan Is an Important Attachment Factor for Cell Entry of Akabane and Schmallenberg Viruses. J Virol. 2017 Jul 12;91(15):e00503-17. doi: 10.1128/JVI.00503-17. PMID: 28539443; PMCID: PMC5512253.

88. Thamamongood T, Aebischer A, Wagner V, Chang MW, Elling R, Benner C, García-Sastre A, Kochs G, Beer M, Schwemmle M. A Genome-Wide CRISPR-Cas9 Screen Reveals the Requirement of Host Cell Sulfation for Schmallenberg Virus Infection. J Virol. 2020 Aug 17;94(17):e00752-20. doi: 10.1128/JVI.00752-20. PMID: 32522852; PMCID: PMC7431805.

89. Albornoz A, Hoffmann AB, Lozach PY, Tischler ND. Early Bunyavirus-Host Cell Interactions. Viruses. 2016 May 24;8(5):143. doi: 10.3390/v8050143. PMID: 27213430; PMCID: PMC4885098.

90. Santos RI, Rodrigues AH, Silva ML, Mortara RA, Rossi MA, Jamur MC, Oliver C, Arruda E. Oropouche virus entry into HeLa cells involves clathrin and requires endosomal acidification. Virus Res. 2008 Dec;138(1-2):139-43. doi: 10.1016/j.virusres.2008.08.016. Epub 2008 Oct 28. PMID: 18840482; PMCID: PMC7114418.

91. Harrison SC. Viral membrane fusion. Virology. 2015 May;479-480:498-507. doi: 10.1016/j.virol.2015.03.043. Epub 2015 Apr 10. PMID: 25866377; PMCID: PMC4424100.

92. Hellert J, Aebischer A, Wernike K, Haouz A, Brocchi E, Reiche S, Guardado-Calvo P, Beer M, Rey FA. Orthobunyavirus spike architecture and recognition by neutralizing antibodies. Nat Commun. 2019 Feb 20;10(1):879. doi: 10.1038/s41467-019-08832-8. PMID: 30787296; PMCID: PMC6382863.

93. Vialat P, Bouloy M. Germiston virus transcriptase requires active 40S ribosomal subunits and utilizes capped cellular RNAs. J Virol. 1992 Feb;66(2):685-93. doi: 10.1128/JVI.66.2.685-693.1992. PMID: 1731108; PMCID: PMC240767.

94. Dunn EF, Pritlove DC, Jin H, Elliott RM. Transcription of a recombinant bunyavirus RNA template by transiently expressed bunyavirus proteins. Virology. 1995 Aug 1;211(1):133-43. doi: 10.1006/viro.1995.1386. PMID: 7544044.

95. Le Sage V, Kanarek JP, Snyder DJ, Cooper VS, Lakdawala SS, Lee N. Mapping of Influenza Virus RNA-RNA Interactions Reveals a Flexible Network. Cell Rep. 2020 Jun 30;31(13):107823. doi: 10.1016/j.celrep.2020.107823. PMID: 32610124; PMCID: PMC7372595.

96. Kohl A, Lowen AC, Léonard VHJ, Elliott RM. Genetic elements regulating packaging of the Bunyamwera orthobunyavirus genome. J Gen Virol. 2006 Jan;87(Pt 1):177-187. doi: 10.1099/vir.0.81227-0. PMID: 16361430.

97. Wichgers Schreur PJ, Kormelink R, Kortekaas J. Genome packaging of the Bunyavirales. Curr Opin Virol. 2018 Dec;33:151-155. doi: 10.1016/j.coviro.2018.08.011. Epub 2018 Sep 15. PMID: 30227361.

98. Liljeroos L, Butcher SJ. Matrix proteins as centralized organizers of negative-sense RNA virions. Front Biosci (Landmark Ed). 2013 Jan 1;18:696-715. doi: 10.2741/4132. PMID: 23276954.

99. Strandin T, Hepojoki J, Vaheri A. Cytoplasmic tails of bunyavirus Gn glycoproteins-Could they act as matrix protein surrogates? Virology. 2013 Mar 15;437(2):73-80. doi: 10.1016/j.virol.2013.01.001. Epub 2013 Jan 26. PMID: 23357734

100. Bermúdez-Méndez E, Katrukha EA, Spruit CM, Kortekaas J, Wichgers Schreur PJ. Visualizing the ribonucleoprotein content of single bunyavirus virions reveals more efficient genome packaging in the arthropod host. Commun Biol. 2021 Mar 22;4(1):345. doi: 10.1038/s42003-021-01821-y. PMID: 33753850; PMCID: PMC7985392.

101. Sicard A, Michalakis Y, Gutiérrez S, Blanc S. The Strange Lifestyle of Multipartite Viruses. PLoS Pathog. 2016 Nov 3;12(11):e1005819. doi: 10.1371/journal.ppat.1005819. PMID: 27812219; PMCID: PMC5094692.

102. Shi X, van Mierlo JT, French A, Elliott RM. Visualizing the replication cycle of bunyamwera orthobunyavirus expressing fluorescent protein-tagged Gc glycoprotein. J Virol. 2010 Sep;84(17):8460-9. doi: 10.1128/JVI.00902-10. Epub 2010 Jun 23. PMID: 20573824; PMCID: PMC2919021.

103. Salanueva IJ, Novoa RR, Cabezas P, López-Iglesias C, Carrascosa JL, Elliott RM, Risco C. Polymorphism and structural maturation of bunyamwera virus in Golgi and post-Golgi compartments. J Virol. 2003 Jan;77(2):1368-81. doi: 10.1128/jvi.77.2.1368-1381.2003. PMID: 12502853; PMCID: PMC140787.

104. Shi X, Kohl A, Léonard VH, Li P, McLees A, Elliott RM. Requirement of the N-terminal region of orthobunyavirus nonstructural protein NSm for virus assembly and morphogenesis. J Virol. 2006 Aug;80(16):8089-99. doi: 10.1128/JVI.00579-06. PMID: 16873265; PMCID: PMC1563826.

105. Ariza A, Tanner SJ, Walter CT et al. Nucleocapsid protein structures from orthobunyaviruses reveal insight into ribonucleoprotein architecture and RNA polymerization. Nucleic Acids Res. 2013 Jun;41(11):5912-26. doi: 10.1093/nar/gkt268. Epub 2013 Apr 17. PMID: 23595147; PMCID: PMC3675483.

106. Zheng W, Tao YJ. Genome encapsidation by orthobunyavirus nucleoproteins. Proc Natl Acad Sci U S A. 2013 May 28;110(22):8769-70. doi: 10.1073/pnas.1306838110. Epub 2013 May 21. PMID: 23696659; PMCID: PMC3670359.

107. Dong H, Li P, Böttcher B, Elliott RM, Dong C. Crystal structure of Schmallenberg orthobunyavirus nucleoprotein-RNA complex reveals a novel RNA sequestration mechanism. RNA. 2013 Aug;19(8):1129-36. doi: 10.1261/rna.039057.113. Epub 2013 Jun 24. PMID: 23798666; PMCID: PMC3708532.

108. Dong H, Li P, Elliott RM, Dong C. Structure of Schmallenberg orthobunyavirus nucleoprotein suggests a novel mechanism of genome encapsidation. J Virol. 2013 May;87(10):5593-601. doi: 10.1128/JVI.00223-13. Epub 2013 Mar 6. PMID: 23468499; PMCID: PMC3648147.

109. Raymond DD, Piper ME, Gerrard SR, Skiniotis G, Smith JL. Phleboviruses encapsidate their genomes by sequestering RNA bases. Proc Natl Acad Sci U S A. 2012 Nov 20;109(47):19208-13. doi: 10.1073/pnas.1213553109. Epub 2012 Nov 5. PMID: 23129612; PMCID: PMC3511139.

110. Bowden TA, Bitto D, McLees A, Yeromonahos C, Elliott RM, Huiskonen JT. Orthobunyavirus ultrastructure and the curious tripodal glycoprotein spike. PLoS Pathog. 2013;9(5):e1003374. doi: 10.1371/journal.ppat.1003374. Epub 2013 May 16. PMID: 23696739; PMCID: PMC3656102.

111. Guardado-Calvo P, Rey FA. The Envelope Proteins of the Bunyavirales. Adv Virus Res. 2017;98:83-118. doi: 10.1016/bs.aivir.2017.02.002. Epub 2017 Apr 8. PMID: 28433053.

112. Stass R, Ng WM, Kim YC, Huiskonen JT. Structures of enveloped virions determined by cryogenic electron microscopy and tomography. Adv Virus Res. 2019;105:35-71. doi: 10.1016/bs.aivir.2019.07.009. Epub 2019 Aug 20. PMID: 31522708; PMCID: PMC7112279.

113. Hofmann H, Li X, Zhang X, Liu W, Kühl A, Kaup F, Soldan SS, González-Scarano F, Weber F, He Y, Pöhlmann S. Severe fever with thrombocytopenia virus glycoproteins are targeted by neutralizing antibodies and can use DC-SIGN as a receptor for pH-dependent entry into human and animal cell lines. J Virol. 2013 Apr;87(8):4384-94. doi: 10.1128/JVI.02628-12. Epub 2013 Feb 6. PMID: 23388721; PMCID: PMC3624395.

114. Hollidge BS, Nedelsky NB, Salzano MV, Fraser JW, González-Scarano F, Soldan SS. Orthobunyavirus entry into neurons and other mammalian cells occurs via clathrin-mediated endocytosis and requires trafficking into early endosomes. J Virol. 2012 Aug;86(15):7988-8001. doi: 10.1128/JVI.00140-12. Epub 2012 May 23. PMID: 22623766; PMCID: PMC3421672.

115. Bangphoomi N, Takenaka-Uema A, Sugi T, Kato K, Akashi H, Horimoto T. Akabane virus utilizes alternative endocytic pathways to entry into mammalian cell lines. J Vet Med Sci. 2014 Nov;76(11):1471-8. doi: 10.1292/jvms.14-0155. Epub 2014 Jul 24. PMID: 25056673; PMCID: PMC4272979.

116. Kielian M, Rey FA. Virus membrane-fusion proteins: more than one way to make a hairpin. Nat Rev Microbiol. 2006 Jan;4(1):67-76. doi: 10.1038/nrmicro1326. PMID: 16357862; PMCID: PMC7097298.

117. Backovic M, Jardetzky TS. Class III viral membrane fusion proteins. Adv Exp Med Biol. 2011;714:91-101. doi: 10.1007/978-94-007-0782-5_3. PMID: 21506008.

118. Dessau M, Modis Y. Crystal structure of glycoprotein C from Rift Valley fever virus. Proc Natl Acad Sci U S A. 2013 Jan 29;110(5):1696-701. doi: 10.1073/pnas.1217780110. Epub 2013 Jan 14. PMID: 23319635; PMCID: PMC3562824.

119. Willensky S, Bar-Rogovsky H, Bignon EA, Tischler ND, Modis Y, Dessau M. Crystal Structure of Glycoprotein C from a Hantavirus in the Post-fusion Conformation. PLoS Pathog. 2016 Oct 26;12(10):e1005948. doi: 10.1371/journal.ppat.1005948. PMID: 27783673; PMCID: PMC5081248.

120. Vaney MC, Rey FA. Class II enveloped viruses. Cell Microbiol. 2011 Oct;13(10):1451-9. doi: 10.1111/j.1462-5822.2011.01653.x. Epub 2011 Aug 11. PMID: 21790946.

121. Lescar J, Roussel A, Wien MW, Navaza J, Fuller SD, Wengler G, Wengler G, Rey FA. The Fusion glycoprotein shell of Semliki Forest virus: an icosahedral assembly primed for fusogenic activation at endosomal pH. Cell. 2001 Apr 6;105(1):137-48. doi: 10.1016/s0092-8674(01)00303-8. PMID: 11301009.

122. Jurtz V, Paul S, Andreatta M, Marcatili P, Peters B, Nielsen M. NetMHCpan-4.0: Improved Peptide-MHC Class I Interaction Predictions Integrating Eluted Ligand and Peptide Binding Affinity Data. J Immunol. 2017 Nov 1;199(9):3360-3368. doi: 10.4049/jimmunol.1700893. Epub 2017 Oct 4. PMID: 28978689; PMCID: PMC5679736.

123. Schrödinger, L., & DeLano, W. (2020). *PyMOL*. Retrieved from http://www.pymol.org/pymol.

124. Berrow NS, Alderton D, Sainsbury S, Nettleship J, Assenberg R, Rahman N, Stuart DI, Owens RJ. A versatile ligation-independent cloning method suitable for high-throughput expression screening applications. Nucleic Acids Res. 2007;35(6):e45. doi: 10.1093/nar/gkm047. Epub 2007 Feb 22. PMID: 17317681; PMCID: PMC1874605.

125. Smith DB, Johnson KS. Single-step purification of polypeptides expressed in Escherichia coli as fusions with glutathione S-transferase. Gene. 1988 Jul 15;67(1):31-40. doi: 10.1016/0378-1119(88)90005-4. PMID: 3047011.

126. Sambrook, Joseph. Molecular Cloning: A Laboratory Manual. Cold Spring Harbor, N.Y. :Cold Spring Harbor Laboratory Press, 2001.

127. Kuo D, Nie M, Courey AJ. SUMO as a solubility tag and in vivo cleavage of SUMO fusion proteins with Ulp1. Methods Mol Biol. 2014;1177:71-80. doi: 10.1007/978-1-4939-1034-2_6. PMID: 24943315

128. Xu Z, Au SW. Mapping residues of SUMO precursors essential in differential maturation by SUMO-specific protease, SENP1. Biochem J. 2005 Mar 1;386(Pt 2):325-30. doi: 10.1042/BJ20041210. PMID: 15487983; PMCID: PMC1134797.

129. Terpe K. Overview of bacterial expression systems for heterologous protein production: from molecular and biochemical fundamentals to commercial systems. Appl Microbiol Biotechnol. 2006 Sep;72(2):211-22. doi: 10.1007/s00253-006-0465-8. Epub 2006 Jun 22. PMID: 16791589.

130. Du F, Liu YQ, Xu YS, Li ZJ, Wang YZ, Zhang ZX, Sun XM. Regulating the T7 RNA polymerase expression in E. coli BL21 (DE3) to provide more host options for recombinant protein production. Microb Cell Fact. 2021 Sep 26;20(1):189. doi: 10.1186/s12934-021-01680-6. PMID: 34565359; PMCID: PMC8474846.

131. de Boer HA, Comstock LJ, Vasser M. The tac promoter: a functional hybrid derived from the trp and lac promoters. Proc Natl Acad Sci U S A. 1983 Jan;80(1):21-5. doi: 10.1073/pnas.80.1.21. PMID: 6337371; PMCID: PMC393301.

132. Russell WM. The development of the three Rs concept. Altern Lab Anim. 1995 May-Jun;23(3):298-304. PMID: 11656565.

133. Altschul SF, Gish W, Miller W, Myers EW, Lipman DJ. Basic local alignment search tool. J Mol Biol. 1990 Oct 5;215(3):403-10. doi: 10.1016/S0022-2836(05)80360-2. PMID: 2231712.

134. Thompson JD, Higgins DG, Gibson TJ. CLUSTAL W: improving the sensitivity of progressive multiple sequence alignment through sequence weighting, position-specific gap penalties and weight matrix choice. Nucleic Acids Res. 1994 Nov 11;22(22):4673-80. doi: 10.1093/nar/22.22.4673. PMID: 7984417; PMCID: PMC308517.

135. Robert X, Gouet P. Deciphering key features in protein structures with the new ENDscript server. Nucleic Acids Res. 2014 Jul;42(Web Server issue):W320-4. doi: 10.1093/nar/gku316. Epub 2014 Apr 21. PMID: 24753421; PMCID: PMC4086106.

136. Hall BG. Building phylogenetic trees from molecular data with MEGA. Mol Biol Evol. 2013 May;30(5):1229-35. doi: 10.1093/molbev/mst012. Epub 2013 Mar 13. PMID: 23486614.

137. Lawrence, J. E., Steward, G. F., Wilhelm, S. W., Weinbauer, M. G., & Suttle, C. A. (2010). Manual of aquatic viral ecology. *American Society of Limnology and Oceanography, Inc*

138. Novoa RR, Calderita G, Cabezas P, Elliott RM, Risco C. Key Golgi factors for structural and functional maturation of bunyamwera virus. J Virol. 2005 Sep;79(17):10852-63. doi: 10.1128/JVI.79.17.10852-10863.2005. PMID: 16103138; PMCID: PMC1193595.

139. Gouzil J, Fablet A, Lara E, Caignard G, Cochet M, Kundlacz C, Palmarini M, Varela M, Breard E, Sailleau C, Viarouge C, Coulpier M, Zientara S, Vitour D. Nonstructural Protein NSs of Schmallenberg Virus Is Targeted to the Nucleolus and Induces Nucleolar Disorganization. J Virol. 2016 Dec 16;91(1):e01263-16. doi: 10.1128/JVI.01263-16. PMID: 27795408; PMCID: PMC5165206.

140. Dantas-Lima JJ, Corteel M, Cornelissen M, Bossier P, Sorgeloos P, Nauwynck HJ. Purification of white spot syndrome virus by iodixanol density gradient centrifugation. J Fish Dis. 2013 Oct;36(10):841-51. doi: 10.1111/jfd.12082. Epub 2013 Feb 6. PMID: 23384051.

141. Palker, T.J. (1990) Mapping of epitopes on human T-cell leukemia virus type 1 envelope glycoprotein In: Human Retrovirology: HTLV (ed. Blattner, W.A.) Raven Press, NY, pp 435-445

142. Wernike K, Reimann I, Banyard AC, Kraatz F, La Rocca SA, Hoffmann B, McGowan S, Hechinger S, Choudhury B, Aebischer A, Steinbach F, Beer M. High genetic variability of Schmallenberg virus M-segment leads to efficient immune escape from neutralizing antibodies. PLoS Pathog. 2021 Jan 26;17(1):e1009247. doi: 10.1371/journal.ppat.1009247. PMID: 33497419; PMCID: PMC7872300.

143. Lei C, Yang J, Hu J, Sun X. On the Calculation of $TCID_{50}$ for Quantitation of Virus Infectivity. Virol Sin. 2021 Feb;36(1):141-144. doi: 10.1007/s12250-020-00230-5. Epub 2020 May 26. PMID: 32458296; PMCID: PMC7973348.

144. Reed LJ, Muench H. A simple method of estimating fifty per cent endpoints. *Am J Hyg.* 1938;27:493–497.

145. Harris JR, De Carlo S. Negative staining and cryo-negative staining: applications in biology and medicine. Methods Mol Biol. 2014;1117:215-58. doi: 10.1007/978-1-62703-776-1_11. PMID: 24357366.

146. Passmore LA, Russo CJ. Specimen Preparation for High-Resolution Cryo-EM. Methods Enzymol. 2016;579:51-86. doi: 10.1016/bs.mie.2016.04.011. Epub 2016 Jun 16. PMID: 27572723; PMCID: PMC5140023.

147. Blancett CD, Monninger MK, Nguessan CA, Kuehl KA, Rossi CA, Olschner SP, Williams PL, Goodman SL, Sun MG. Utilization of Capsules for Negative Staining of Viral Samples within Biocontainment. J Vis Exp. 2017 Jul 19;(125):56122. doi: 10.3791/56122. PMID: 28745647; PMCID: PMC5612576.

148. Sgro GG, Costa TRD. Cryo-EM Grid Preparation of Membrane Protein Samples for Single Particle Analysis. Front Mol Biosci. 2018 Jul 31;5:74. doi: 10.3389/fmolb.2018.00074. PMID: 30131964; PMCID: PMC6090150.

149. Dubochet J, Adrian M, Lepault J, McDowall A. Emerging techniques: Cryo-electron microscopy of vitrified biological specimens. Trends in Biological Sciences. 1985:143–146.

150. Adrian M, Dubochet J, Lepault J, McDowall AW. Cryo-electron microscopy of viruses. Nature. 1984; 308(5954):32–36.

151. Weissenberger G, Henderikx RJM, Peters PJ. Understanding the invisible hands of sample preparation for cryo-EM. Nat Methods. 2021 May;18(5):463-471. doi: 10.1038/s41592-021-01130-6. Epub 2021 May 7. PMID: 33963356.

152. Dobro MJ, Melanson LA, Jensen GJ, McDowall AW. Plunge freezing for electron cryomicroscopy. Methods Enzymol. 2010;481:63-82. doi: 10.1016/S0076-6879(10)81003-1. PMID: 20887853.

153. Ruska E. The development of the electron microscope and of electron microscopy Rev. Mod. Phys. 1987. 59, 627–638 doi: 10.1103/RevModPhys.59.627.

154. Robinson AL. Electron Microscope Inventors Share Nobel Physics Prize: Ernst Ruska built the first electron microscope in 1931; Gerd Binnig and Heinrich Rohrer developed the scanning tunneling microscope 50 years later. Science. 1986 Nov 14;234(4778):821-2. doi: 10.1126/science.234.4778.821. PMID: 17758103.

155. Piazza, L., Masiel, D. J., LaGrange, T., Reed, B. W., Barwick, B., & Carbone, F. (2013). Design and implementation of a fs-resolved transmission electron microscope based on thermionic gun technology. Chemical Physics, 423, 79–84.

156. Egerton RF. Choice of operating voltage for a transmission electron microscope. Ultramicroscopy. 2014 Oct;145:85-93. doi: 10.1016/j.ultramic.2013.10.019. Epub 2014 Mar 12. PMID: 24679438.

157. Xing Q, Lograsso TA. A rapid method to correct objective lens astigmatism in a TEM. Ultramicroscopy. 2009 Mar;109(4):287-90. doi: 10.1016/j.ultramic.2008.11.014. Epub 2008 Dec 6. PMID: 19150754.

158. Capitani GC, Oleynikov P, Hovmöller S, Mellini M. A practical method to detect and correct for lens distortion in the TEM. Ultramicroscopy. 2006 Jan;106(2):66-74. doi: 10.1016/j.ultramic.2005.06.003. Epub 2005 Jul 1. PMID: 16046067.

159. Malatesta M. Transmission Electron Microscopy as a Powerful Tool to Investigate the Interaction of Nanoparticles with Subcellular Structures. Int J Mol Sci. 2021 Nov 26;22(23):12789. doi: 10.3390/ijms222312789. PMID: 34884592; PMCID: PMC8657944.

160. Wade R. H. A brief look at imaging and contrast transfer. 1992. Ultramicroscopy 46(1-4) 145-156 doi: 10.1016/0304-3991(92)90011-8.

161. Uka A, Ndreu Halili A, Polisi X, Topal AO, Imeraj G, Vrana NE. Basis of Image Analysis for Evaluating Cell Biomaterial Interaction Using Brightfield Microscopy. Cells Tissues Organs. 2021;210(2):77-104. doi: 10.1159/000512969. Epub 2021 Jun 29. PMID: 34186537.

162. Wang HW, Fan X. Challenges and opportunities in cryo-EM with phase plate. Curr Opin Struct Biol. 2019 Oct;58:175-182. doi: 10.1016/j.sbi.2019.06.013. Epub 2019 Jul 30. PMID: 31374473.

163. Williams, D.B., Carter, C.B. (1996). The Transmission Electron Microscope. In: Transmission Electron Microscopy. Springer, Boston, MA. https://doi.org/10.1007/978-1-4757-2519-3_1

164. Scherzer O. Über einige fehler von elektronenlinsen. Zeitschrift für Physik. 1936 Sep;101(9):593-603.

165. Sheppard CJR. Resolution and super-resolution. Microsc Res Tech. 2017 Jun;80(6):590-598. doi: 10.1002/jemt.22834. Epub 2017 Feb 9. PMID: 28181372.

166. Jia CL, Lentzen M, Urban K. High-resolution transmission electron microscopy using negative spherical aberration. Microsc Microanal. 2004 Apr;10(2):174-84. doi: 10.1017/S1431927604040425. PMID: 15306044.

167. Haider M, Hartel P, Müller H, Uhlemann S, Zach J. Current and future aberration correctors for the improvement of resolution in electron microscopy. Philos Trans A Math Phys Eng Sci. 2009 Sep 28;367(1903):3665-82. doi: 10.1098/rsta.2009.0121. PMID: 19687059.

168. Leary, R., & Brydson, R. Chromatic Aberration Correction. Advances in Imaging and Electron Physics. 2011 *73–130.* doi:10.1016/b978-0-12-385861-0.00003-8.

169. Vargas J, Otón J, Marabini R, Jonic S, de la Rosa-Trevín JM, Carazo JM, Sorzano CO. FASTDEF: fast defocus and astigmatism estimation for high-throughput transmission electron microscopy. J Struct Biol. 2013 Feb;181(2):136-48. doi: 10.1016/j.jsb.2012.12.006. Epub 2012 Dec 20. PMID: 23261401.

170. DeRosier DJ. Correction of high-resolution data for curvature of the Ewald sphere. Ultramicroscopy. 2000 Mar;81(2):83-98. doi: 10.1016/s0304-3991(99)00120-5. PMID: 10998793.

171. Wade R. H. A brief look at imaging and contrast transfer. 1992. Ultramicroscopy 46(1-4) 145-156 doi: 10.1016/0304-3991(92)90011-8.

172. H. Lipson, C.A. Taylor, Fourier Transforms and X-ray Difraction. 1958. G. Bell and Sons Ltd.

173. Thon F. Zur Defokussierungsabhängigkeit des Phasenkontrastes bei der elektronenmikroskopischen Abbildung. Z Naturforschung. 1966; 21a:476–478.

174. Reimer L., Helmut K. Transm. Electron Microsc. – Phys. Image Form 2008. 5th Edition, Springer.

175. Scherzer O. The Theoretical Resolution Limit of the Electron Microscope. J. Appl. Phys. 20, 20 (1949); doi: 10.1063/1.1698233

176. Erickson HP, Klug A. The Fourier Transform of an Electron micrograph: Effects of Defocussing and Aberrations, and Implications for the Use of Underfocus Contrast Enhancement. 2010 Physical Chemistry Chemical Physics 74(11):1129 – 113.

177. Humphreys CJ. The significance of Bragg's law in electron diffraction and microscopy, and Bragg's second law. Acta Crystallogr A. 2013 Jan;69(Pt 1):45-50. doi: 10.1107/S0108767312047587. Epub 2012 Dec 5. PMID: 23250060.

178. Zanetti G, Riches JD, Fuller SD, Briggs JA. Contrast transfer function correction applied to cryo-electron tomography and sub-tomogram averaging. J Struct Biol. 2009 Nov;168(2):305-12. doi: 10.1016/j.jsb.2009.08.002. Epub 2009 Aug 8. PMID: 19666126; PMCID: PMC2806944.

179. Williams DB, Carter CB (1996) Transmission electron microscopy: a textbook for material science. Plenum Press, New York

180. Jeong, H.S., Park, H.N., Kim, J.G., Hyun, J.K. Critical importance of the correction of contrast transfer function for transmission electron microscopy-mediated structural biology. Journal of Analytical Science and Technology 2013 4(1), 14. doi:10.1186/2093-3371-4-14

181. P. Penczek, J. Zhu, R. Schröder, and J. Frank, Three-dimensional reconstruction with contrast transfer compensation from defocus series, 1997Scanning Microscopy 11, 47–154 doi: 10.1142/9789813234864_0021.

182. Fan X, Zhao L, Liu C, Zhang JC, Fan K, Yan X, Peng HL, Lei J, Wang HW. Near-Atomic Resolution Structure Determination in Over-Focus with Volta Phase Plate by Cs-Corrected Cryo-EM. Structure. 2017 Oct 3;25(10):1623-1630.e3. doi: 10.1016/j.str.2017.08.008. Epub 2017 Sep 21. PMID: 28943337.

183. Bhamre T, Zhang T, Singer A. Denoising and covariance estimation of single particle cryo-EM images. J Struct Biol. 2016 Jul;195(1):72-81. doi: 10.1016/j.jsb.2016.04.013. Epub 2016 Apr 27. PMID: 27129418.

184. Ren L, Zheng B, Liu H. Tutorial on X-ray photon counting detector characterization. J Xray Sci Technol. 2018;26(1):1-28. doi: 10.3233/XST-16210. PMID: 29154310; PMCID: PMC5909414.

185. Rohou A, Grigorieff N. CTFFIND4: Fast and accurate defocus estimation from electron micrographs. J Struct Biol. 2015 Nov;192(2):216-21. doi: 10.1016/j.jsb.2015.08.008. Epub 2015 Aug 13. PMID: 26278980; PMCID: PMC6760662.

186. Cheng Y, Grigorieff N, Penczek PA, Walz T. A primer to single-particle cryo-electron microscopy. Cell. 2015 Apr 23;161(3):438-449. doi: 10.1016/j.cell.2015.03.050. PMID: 25910204; PMCID: PMC4409659.

187. Luo W, Zhang Y, Feizi A, Göröcs Z, Ozcan A. Pixel super-resolution using wavelength scanning. Light Sci Appl. 2016 Apr 8;5(4):e16060. doi: 10.1038/lsa.2016.60. PMID: 30167157; PMCID: PMC6059953.

188. Glaeser RM, Hall RJ. Reaching the information limit in cryo-EM of biological macromolecules: experimental aspects. Biophys J. 2011 May 18;100(10):2331-7. doi: 10.1016/j.bpj.2011.04.018. PMID: 21575566; PMCID: PMC3093552.

189. McMullan G, Faruqi AR, Clare D, Henderson R. Comparison of optimal performance at 300keV of three direct electron detectors for use in low dose electron microscopy. Ultramicroscopy. 2014 Dec;147:156-63. doi: 10.1016/j.ultramic.2014.08.002. Epub 2014 Aug 9. PMID: 25194828; PMCID: PMC4199116.

190. Fischer N, Neumann P, Konevega AL, Bock LV, Ficner R, Rodnina MV, Stark H. Structure of the E. coli ribosome-EF-Tu complex at <3 Å resolution by Cs-corrected cryo-EM. Nature. 2015 Apr 23;520(7548):567-70. doi: 10.1038/nature14275. Epub 2015 Feb 23. PMID: 25707802.

191. Brilot AF, Chen JZ, Cheng A, Pan J, Harrison SC, Potter CS, Carragher B, Henderson R, Grigorieff N. Beam-induced motion of vitrified specimen on holey carbon film. J Struct Biol. 2012 Mar;177(3):630-7. doi: 10.1016/j.jsb.2012.02.003. Epub 2012 Feb 16. PMID: 22366277; PMCID: PMC3322646.

192. Ripstein ZA, Rubinstein JL. Processing of Cryo-EM Movie Data. Methods Enzymol. 2016;579:103-24. doi: 10.1016/bs.mie.2016.04.009. Epub 2016 Jun 1. PMID: 27572725.

193. Cheng Y. Single-particle cryo-EM-How did it get here and where will it go. Science. 2018 Aug 31;361(6405):876-880. doi: 10.1126/science.aat4346. PMID: 30166484; PMCID: PMC6460916.

194. Zheng SQ, Palovcak E, Armache JP, Verba KA, Cheng Y, Agard DA. MotionCor2: anisotropic correction of beam-induced motion for improved cryo-electron microscopy. Nat Methods. 2017 Apr;14(4):331-332. doi: 10.1038/nmeth.4193. Epub 2017 Feb 27. PMID: 28250466; PMCID: PMC5494038.

195. Scheres SH. RELION: implementation of a Bayesian approach to cryo-EM structure determination. J Struct Biol. 2012;180(3):519-530. doi:10.1016/j.jsb.2012.09.006

196. Zivanov J, Nakane T, Forsberg BO, Kimanius D, Hagen WJ, Lindahl E, Scheres SH. New tools for automated high-resolution cryo-EM structure determination in RELION-3. Elife. 2018 Nov 9;7:e42166. doi: 10.7554/eLife.42166. PMID: 30412051; PMCID: PMC6250425.

197. Marabini R, Masegosa IM, San Martin MC, Marco S, Fernandez JJ, de la Fraga LG, Vaquerizo C, Carazo JM. Xmipp: An Image Processing Package for Electron Microscopy. J Struct Biol. 1996 Oct;116(1):237-40. doi: 10.1006/jsbi.1996.0036. PMID: 8812978.

198. Schindelin J, Arganda-Carreras I, Frise E, Kaynig V, Longair M, Pietzsch T, Preibisch S, Rueden C, Saalfeld S, Schmid B, Tinevez JY, White DJ, Hartenstein V, Eliceiri K, Tomancak P, Cardona A. Fiji: an open-source platform for biological-image analysis. Nat Methods. 2012 Jun 28;9(7):676-82. doi: 10.1038/nmeth.2019. PMID: 22743772; PMCID: PMC3855844.

199. Garces DH, Rhodes WT, Peña NM. Projection-slice theorem: a compact notation. J Opt Soc Am A Opt Image Sci Vis. 2011 May 1;28(5):766-9. doi: 10.1364/JOSAA.28.000766. PMID: 21532686.

200. Lyumkis D. Challenges and opportunities in cryo-EM single-particle analysis. J Biol Chem. 2019 Mar 29;294(13):5181-5197. doi: 10.1074/jbc.REV118.005602. Epub 2019 Feb 25. PMID: 30804214; PMCID: PMC6442032.

201. De Rosier DJ, Klug A. Reconstruction of three-dimensional structures from electron micrographs. Nature. 1968 Jan 13;217(5124):130-4. doi: 10.1038/217130a0. PMID: 23610788.

202. Kuo IA, Glaeser RM. Development of methodology for low exposure, high resolution electron microscopy of biological specimens. Ultramicroscopy. 1975 Jul;1(1):53-66. doi: 10.1016/s0304-3991(75)80007-6. PMID: 1236019.

203. Penczek PA. Resolution measures in molecular electron microscopy. Methods Enzymol. 2010;482:73-100. doi: 10.1016/S0076-6879(10)82003-8. PMID: 20888958; PMCID: PMC3165049.

204. Henderson R, Sali A, Baker ML, Carragher B, Devkota B, Downing KH, Egelman EH, Feng Z, Frank J, Grigorieff N, Jiang W, Ludtke SJ, Medalia O, Penczek PA, Rosenthal PB, Rossmann MG, Schmid MF, Schröder GF, Steven AC, Stokes DL, Westbrook JD, Wriggers W, Yang H, Young J, Berman HM, Chiu W, Kleywegt GJ, Lawson CL. Outcome of the first electron microscopy validation task force meeting. Structure. 2012 Feb 8;20(2):205-14. doi: 10.1016/j.str.2011.12.014. PMID: 22325770; PMCID: PMC3328769.

205. Scheres SH, Chen S. Prevention of overfitting in cryo-EM structure determination. Nat Methods. 2012 Sep;9(9):853-4. doi: 10.1038/nmeth.2115. PMID: 22842542; PMCID: PMC4912033.

206. Galaz-Montoya JG, Ludtke SJ. The advent of structural biology *in situ* by single particle cryo-electron tomography. Biophys Rep. 2017;3(1):17-35. doi: 10.1007/s41048-017-0040-0. Epub 2017 May 29. PMID: 28781998; PMCID: PMC5516000.

207. Wan W, Briggs JA. Cryo-Electron Tomography and Subtomogram Averaging. Methods Enzymol. 2016;579:329-67. doi: 10.1016/bs.mie.2016.04.014. Epub 2016 Jun 22. PMID: 27572733.

208. Hagen WJH, Wan W, Briggs JAG. Implementation of a cryo-electron tomography tilt-scheme optimized for high resolution subtomogram averaging. J Struct Biol. 2017 Feb;197(2):191-198. doi: 10.1016/j.jsb.2016.06.007. Epub 2016 Jun 14. PMID: 27313000; PMCID: PMC5287356.

209. Kremer JR, Mastronarde DN, McIntosh JR. Computer visualization of three-dimensional image data using IMOD. J Struct Biol. 1996 Jan-Feb;116(1):71-6. doi: 10.1006/jsbi.1996.0013. PMID: 8742726.

210. Turk M, Baumeister W. The promise and the challenges of cryo-electron tomography. FEBS Lett. 2020 Oct;594(20):3243-3261. doi: 10.1002/1873-3468.13948. Epub 2020 Oct 23. PMID: 33020915.

211. Schmid MF, Booth CR. Methods for aligning and for averaging 3D volumes with missing data. J Struct Biol. 2008 Mar;161(3):243-8. doi: 10.1016/j.jsb.2007.09.018. Epub 2007 Oct 1. PMID: 18299206; PMCID: PMC2680136.

212. Hoppe W, Hegerl R. Three-dimensional structure determination by electron microscopy. In: Hawkes PW, editor. Computer Processing of Electron Microscope Images. Springer-Verlag; Heidelberg: 1980. pp. 127–186

213. Radermacher M. Weighted Back-projection Methods. In: Frank J. (eds) 2007 Electron Tomography. Springer, New York, NY. https://doi.org/10.1007/978-0-387-69008-7_9

214. Gilbert P. Iterative methods for the three-dimensional reconstruction of an object from projections. J Theor Biol. 1972 Jul;36(1):105-17. doi: 10.1016/0022-5193(72)90180-4. PMID: 5070894.

215. Navarro PP. Quantitative Cryo-Electron Tomography. Front Mol Biosci. 2022 Jul 6;9:934465. doi: 10.3389/fmolb.2022.934465. PMID: 35874617; PMCID: PMC9296768.

216. Bharat TAM, Russo CJ, Löwe J, Passmore LA, Scheres SHW. Advances in Single-Particle Electron Cryomicroscopy Structure Determination applied to Sub-tomogram Averaging. Structure. 2015 Sep 1;23(9):1743-1753. doi: 10.1016/j.str.2015.06.026. Epub 2015 Aug 6. PMID: 26256537; PMCID: PMC4559595.

217. Hoppe W, Gassmann J, Hunsmann N, Schramm HJ, Sturm M. Three-dimensional reconstruction of individual negatively stained yeast fatty-acid synthetase molecules from tilt series in the electron microscope. Hoppe Seylers Z Physiol Chem. 1974 Nov;355(11):1483-7. PMID: 4142629.

218. Baumeister W, Grimm R, Walz J. Electron tomography of molecules and cells. Trends Cell Biol. 1999 Feb;9(2):81-5. doi: 10.1016/s0962-8924(98)01423-8. PMID: 10087625.

219. Baumeister W, Hahn M. Relevance of three-dimensional reconstructions of stain distributions for structural analysis of biomolecules. Hoppe Seylers Z Physiol Chem. 1975 Aug;356(8):1313-6. doi: 10.1515/bchm2.1975.356.2.1313. PMID: 51815.

220. Frank J. Introduction: Principles of Electron Tomography. 2007 In: Frank J. (eds) Electron Tomography. Springer, New York, NY. https://doi.org/10.1007/978-0-387-69008-7_1

221. Zhang P. Advances in cryo-electron tomography and subtomogram averaging and classification. Curr Opin Struct Biol. 2019 Oct;58:249-258. doi: 10.1016/j.sbi.2019.05.021. Epub 2019 Jul 5. PMID: 31280905; PMCID: PMC6863431.

222. Leigh KE, Navarro PP, Scaramuzza S, Chen W, Zhang Y, Castaño-Díez D, Kudryashev M. Subtomogram averaging from cryo-electron tomograms. Methods Cell Biol. 2019;152:217-259. doi: 10.1016/bs.mcb.2019.04.003. Epub 2019 May 15. PMID: 31326022.

223. Castaño-Díez D, Kudryashev M, Arheit M, Stahlberg H. Dynamo: a flexible, user-friendly development tool for subtomogram averaging of cryo-EM data in high-performance computing environments. J Struct Biol. 2012 May;178(2):139-51. doi: 10.1016/j.jsb.2011.12.017. Epub 2012 Jan 8. PMID: 22245546.

224. Förster F, Hegerl R. Structure determination in situ by averaging of tomograms. Methods Cell Biol. 2007;79:741-67. doi: 10.1016/S0091-679X(06)79029-X. PMID: 17327182.

225. Kudryashev M, Castaño-Díez D, Deluz C, Hassaine G, Grasso L, Graf-Meyer A, Vogel H, Stahlberg H. The Structure of the Mouse Serotonin 5-HT3 Receptor in Lipid Vesicles. Structure. 2016 Jan 5;24(1):165-170. doi: 10.1016/j.str.2015.11.004. Epub 2015 Dec 24. PMID: 26724993.

226. Briggs JA. Structural biology in situ--the potential of subtomogram averaging. Curr Opin Struct Biol. 2013 Apr;23(2):261-7. doi: 10.1016/j.sbi.2013.02.003. Epub 2013 Mar 4. PMID: 23466038.

227. Pettersen EF, Goddard TD, Huang CC, Couch GS, Greenblatt DM, Meng EC, Ferrin TE. UCSF Chimera--a visualization system for exploratory research and analysis. J Comput Chem. 2004 Oct;25(13):1605-12. doi: 10.1002/jcc.20084. PMID: 15264254.

228. Punch EK, Hover S, Blest HTW, Fuller J, Hewson R, Fontana J, Mankouri J, Barr JN. Potassium is a trigger for conformational change in the fusion spike of an enveloped RNA virus. J Biol Chem. 2018 Jun 29;293(26):9937-9944. doi: 10.1074/jbc.RA118.002494. Epub 2018.

229. Balinandi S, Hayer J, Cholleti H, Wille M, Lutwama JJ, Malmberg M, Mugisha L. Identification and molecular characterization of highly divergent RNA viruses in cattle, Uganda. Virus Res. 2022 May;313:198739. doi: 10.1016/j.virusres.2022.198739. Epub 2022 Mar 8. PMID: 35271887.

230. Wichgers Schreur PJ, van de Water S, Harmsen M, Bermúdez-Méndez E, Drabek D, Grosveld F, Wernike K, Beer M, Aebischer A, Daramola O, Rodriguez Conde S, Brennan K, Kozub D, Søndergaard Kristiansen M, Mistry KK, Deng Z, Hellert J, Guardado-Calvo P, Rey FA, van Keulen L, Kortekaas J. Multimeric single-domain antibody complexes protect against bunyavirus infections. Elife. 2020 Apr 21;9:e52716. doi: 10.7554/eLife.52716. PMID: 32314955; PMCID: PMC7173960.

231. Šantak M, Matić Z. The Role of Nucleoprotein in Immunity to Human Negative-Stranded RNA Viruses-Not Just Another Brick in the Viral Nucleocapsid. Viruses. 2022 Mar 3;14(3):521. doi: 10.3390/v14030521. PMID: 35336928; PMCID: PMC8955406.

232. Sridhar S, Begom S, Bermingham A, Hoschler K, Adamson W, Carman W, Bean T, Barclay W, Deeks JJ, Lalvani A. Cellular immune correlates of protection against symptomatic pandemic influenza. Nat Med. 2013 Oct;19(10):1305-12. doi: 10.1038/nm.3350. Epub 2013 Sep 22. PMID: 24056771.

233. Sullivan BM, Sakabe S, Hartnett JN, Ngo N, Goba A, Momoh M, Demby Sandi J, Kanneh L, Cubitt B, Garcia SD, Ware BC, Kotliar D, Robles-Sikisaka R, Gangavarapu K, Branco L, Eromon P, Odia I, Ogbaini-Emovon E, Folarin O, Okogbenin S, Okokhere PO, Happi C, de la Torre JC, Sabeti PC, Andersen KG, Garry RF, Grant DS, Schieffelin JS, Oldstone MBA. High crossreactivity of human T cell responses between Lassa virus lineages. PLoS Pathog. 2020 Mar 6;16(3):e1008352. doi: 10.1371/journal.ppat.1008352. PMID: 32142546; PMCID: PMC7080273.

234. Sakabe S, Sullivan BM, Hartnett JN, Robles-Sikisaka R, Gangavarapu K, Cubitt B, Ware BC, Kotliar D, Branco LM, Goba A, Momoh M, Sandi JD, Kanneh L, Grant DS, Garry RF, Andersen KG, de la Torre JC, Sabeti PC, Schieffelin JS, Oldstone MBA. Analysis of CD8$^+$ T cell response during the 2013-2016 Ebola epidemic in West Africa. Proc Natl Acad Sci U S A. 2018 Aug 7;115(32):E7578-E7586. doi: 10.1073/pnas.1806200115. Epub 2018 Jul 23. PMID: 30038008; PMCID: PMC6094108.

235. Dowall SD, Buttigieg KR, Findlay-Wilson SJ, Rayner E, Pearson G, Miloszewska A, Graham VA, Carroll MW, Hewson R. A Crimean-Congo hemorrhagic fever (CCHF) viral vaccine expressing nucleoprotein is immunogenic but fails to confer protection against lethal disease. Hum Vaccin Immunother. 2016;12(2):519-27. doi: 10.1080/21645515.2015.1078045. PMID: 26309231; PMCID: PMC5049717.

236. Goedhals D, Paweska JT, Burt FJ. Long-lived CD8+ T cell responses following Crimean-Congo haemorrhagic fever virus infection. PLoS Negl Trop Dis. 2017 Dec 19;11(12):e0006149. doi: 10.1371/journal.pntd.0006149. PMID: 29261651; PMCID: PMC5752039.

237. Boshra H, Lorenzo G, Rodriguez F, Brun A. A DNA vaccine encoding ubiquitinated Rift Valley fever virus nucleoprotein provides consistent immunity and protects IFNAR(-/-) mice upon lethal virus challenge. Vaccine. 2011 Jun 15;29(27):4469-75. doi: 10.1016/j.vaccine.2011.04.043. Epub 2011 May 5. PMID: 21549790.

238. Harmon JR, Barbeau DJ, Nichol ST, Spiropoulou CF, McElroy AK. Rift Valley fever virus vaccination induces long-lived, antigen-specific human T cell responses. NPJ Vaccines. 2020 Feb 28;5(1):17. doi: 10.1038/s41541-020-0166-9. PMID: 32140261; PMCID: PMC7048758.

239. Xu W, Watts DM, Costanzo MC, Tang X, Venegas LA, Jiao F, Sette A, Sidney J, Sewell AK, Wooldridge L, Makino S, Morrill JC, Peters CJ, Kan-Mitchell J. The nucleocapsid protein of Rift Valley fever virus is a potent human CD8+ T cell antigen and elicits memory responses. PLoS One. 2013;8(3):e59210. doi: 10.1371/journal.pone.0059210. Epub 2013 Mar 18. PMID: 23527138; PMCID: PMC3601065.

240. Nguyen B, Tolia NH. Protein-based antigen presentation platforms for nanoparticle vaccines. NPJ Vaccines. 2021 May 13;6(1):70. doi: 10.1038/s41541-021-00330-7. PMID: 33986287; PMCID: PMC8119681.

241. Mbanefo EC, Kumagai T, Kodama Y, Kurosaki T, Furushima-Shimogawara R, Cherif MS, Mizukami S, Kikuchi M, Huy NT, Ohta N, Sasaki H, Hirayama K. Immunogenicity and anti-fecundity effect of nanoparticle coated glutathione S-transferase (SjGST) DNA vaccine against murine Schistosoma japonicum infection. Parasitol Int. 2015 Aug;64(4):24-31. doi: 10.1016/j.parint.2015.01.005. Epub 2015 Jan 17. PMID: 25603531.

242. Goller KV, Höper D, Schirrmeier H, Mettenleiter TC, Beer M. Schmallenberg virus as possible ancestor of Shamonda virus. Emerg Infect Dis. 2012 Oct;18(10):1644-6. doi: 10.3201/eid1810.120835. PMID: 23017842; PMCID: PMC3471646.

243. Hechinger S, Wernike K, Beer M. Evaluating the protective efficacy of a trivalent vaccine containing Akabane virus, Aino virus and Chuzan virus against Schmallenberg virus infection. Vet Res. 2013 Dec 5;44(1):114. doi: 10.1186/1297-9716-44-114. PMID: 24313924; PMCID: PMC4028744.

244. Wernike K, Brocchi E, Beer M. Effective interference between Simbu serogroup orthobunyaviruses in mammalian cells. Vet Microbiol. 2016 Nov 30;196:23-26. doi: 10.1016/j.vetmic.2016.10.007. Epub 2016 Oct 11. PMID: 27939151.

245. McGee MC, Huang W. Evolutionary conservation and positive selection of influenza A nucleoprotein CTL epitopes for universal vaccination. J Med Virol. 2022 Jun;94(6):2578-2587. doi: 10.1002/jmv.27662. Epub 2022 Feb 26. PMID: 35171514; PMCID: PMC9052727.

246. Ter Horst S, Conceição-Neto N, Neyts J, Rocha-Pereira J. Structural and functional similarities in bunyaviruses: Perspectives for pan-bunya antivirals. Rev Med Virol. 2019 May;29(3):e2039. doi: 10.1002/rmv.2039. Epub 2019 Feb 11. PMID: 30746831; PMCID: PMC7169261.

247. Serris A. The Input of Structural Vaccinology in the Search for Vaccines against Bunyaviruses. Viruses. 2021 Sep 4;13(9):1766. doi: 10.3390/v13091766. PMID: 34578349; PMCID: PMC8473429.

248. Tan YZ, Cheng A, Potter CS, Carragher B. Automated data collection in single particle electron microscopy. Microscopy (Oxf). 2016 Feb;65(1):43-56. doi: 10.1093/jmicro/dfv369. Epub 2015 Dec 15. PMID: 26671944; PMCID: PMC4749047.

249. Neuman BW, Adair BD, Yoshioka C, Quispe JD, Orca G, Kuhn P, Milligan RA, Yeager M, Buchmeier MJ. Supramolecular architecture of severe acute respiratory syndrome coronavirus revealed by electron cryomicroscopy. J Virol. 2006 Aug;80(16):7918-28. doi: 10.1128/JVI.00645-06. PMID: 16873249; PMCID: PMC1563832.

Appendix I

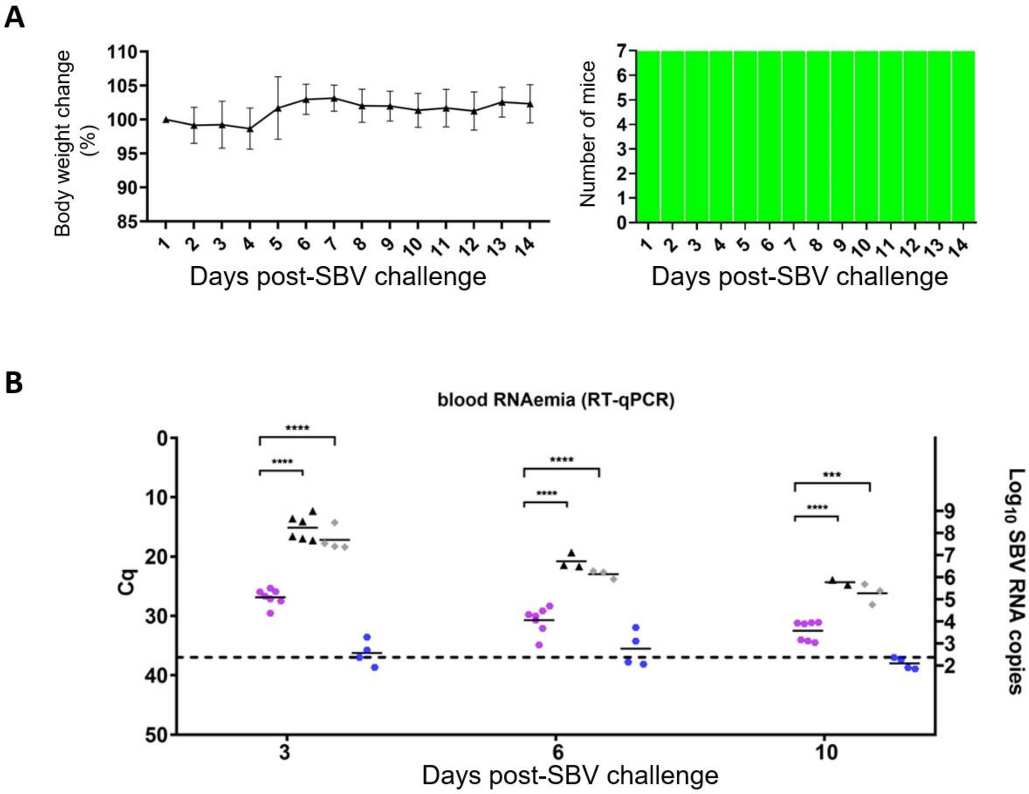

(A) Health assessment of the SBV-N vaccinated mice. Left: Body weight variation plot (%) from full SBV-N vaccinated animal group (n=7) at each day post-SBV challenge shown as medians, the error bars represent the SDs. Right: Health monitoring plots. Colouring scheme shows the health status of the given animal being the health shown in green at the given day post-infection. **(B) Quantification of viraemia post viral infection of the SBV-N vaccinated mice.** 75 µL Blood samples were harvested at 3, 6 and 10 dpi followed by RNA extraction and RT-qPCR. Values plotted are the Cqs obtained at the RT-qPCRs and the corresponding $\log_{10}$ SBV RNA copies per sample at the given dpi, being each point a different animal. The dashed intense line corresponds to the RT-qPCR threshold. Horizontal bars represent the medians among the distinctly immunized groups, which are coloured as follows: Purple (SBV-N); black (GST); grey (not immunized); dark blue (neither SBV challenged nor immunized). Asterisks denote statistical significance with $P < 0.001$ (***) or $P < 0.0001$ (****), as denoted by one-way ANOVA test.

Appendix II

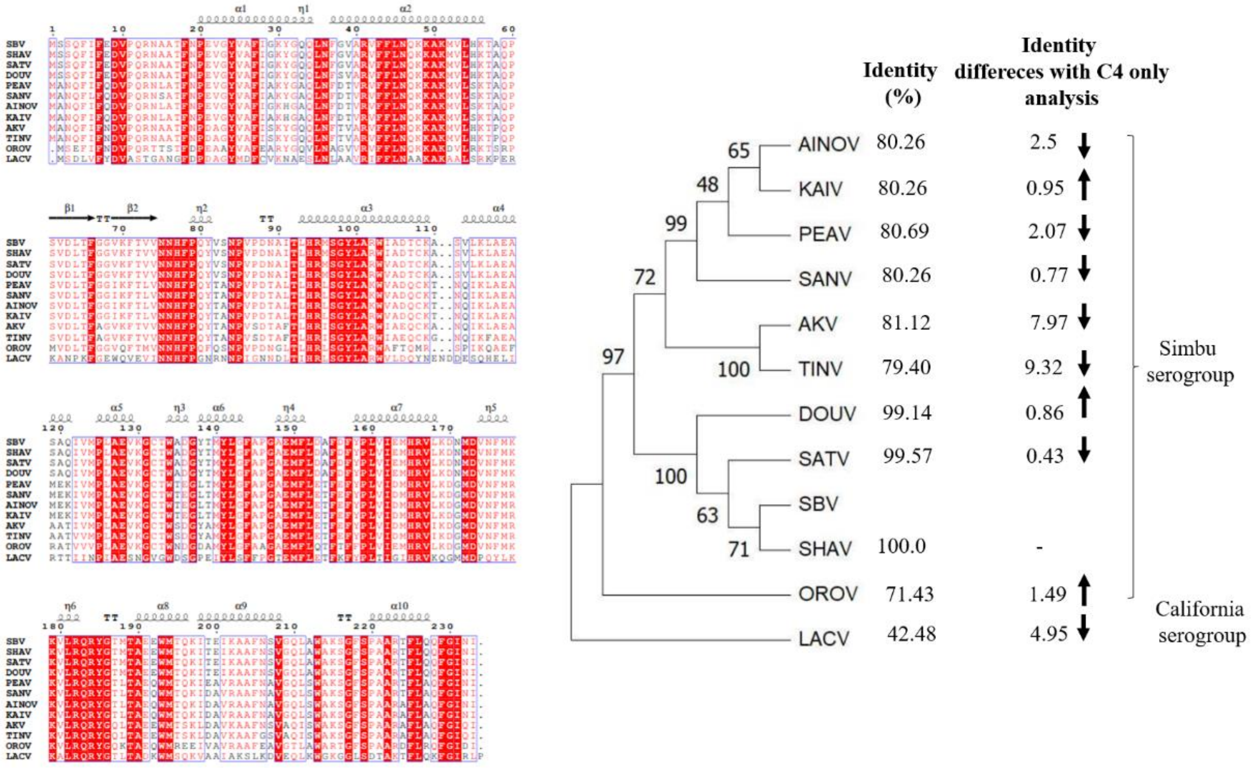

Left: ESPrit multiple alignments from the full SBV-N with nucleoproteins from distinct *Orthobunyaviruses*, hits were given by BLASTp and ordered from top to bottom according to the corresponding pairwise identities; above the secondary structure elements derived from the crystal structure PDB ID 3ZL9 (104). AINOV Aino virus; KAIV Kaikalur virus; PEAV Peaton virus; SANV Sango Virus; AKV Akabane virus; TINV Tinaroo virus; SBV Schmallenberg virus; DOUV Douglas virus; SATV Sathuperi virus; SHAV Shamonda virus; OROV Oropouche virus; LACV La Crosse virus. **Right:** Phylogenetic analysis from the previously aligned sequences carried out on MEGA with a 500-bootstrap method. Sequences identities with the corresponding regions from SBV and the different *Orthobunyaviruses* are given at the right.

Appendix III

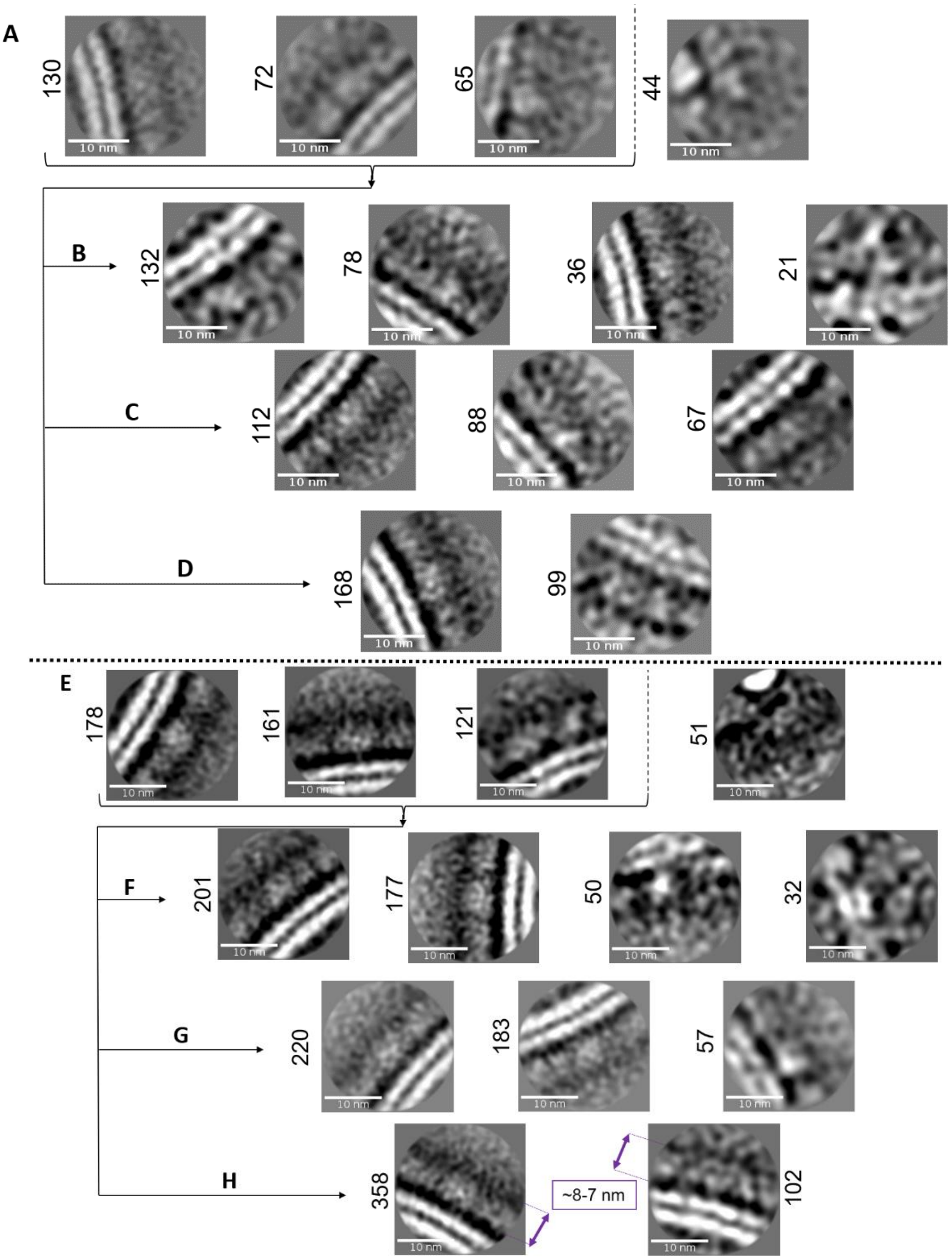

Initial 2D classifications. (A) K=4^a classification of the initial dataset (n=311). **(B)** K=4^b, a k=4 classification from the pool of the first 3 classes obtained from the initial dataset in k=4^a. **(C)** K=3 classification from the pool of the first 3 classes obtained from the initial dataset in k=4^a. **(D)** k=2 classification from the pool of the first 3 classes obtained from the initial dataset in k=4^a. **(E)** K=4^a classification of the whole dataset (n=511). **(F)** K=4^b, a k=4 classification from the pool of the first 3 classes obtained in k=4^a from the whole dataset. **(G)** K=3 classification from the pool of the first 3 classes from the whole dataset obtained in k=4^a. **(H)** K=2 classification from the pool of the first 3 classes obtained in k=4^a from the whole dataset, the upper region of the bilayers with the putative viral glycoprotein spike was measured with FIJI and has its size depicted in purple arrows. All classes obtained are accompanied on their sides by the number of particles belonging to them.

Appendix IV

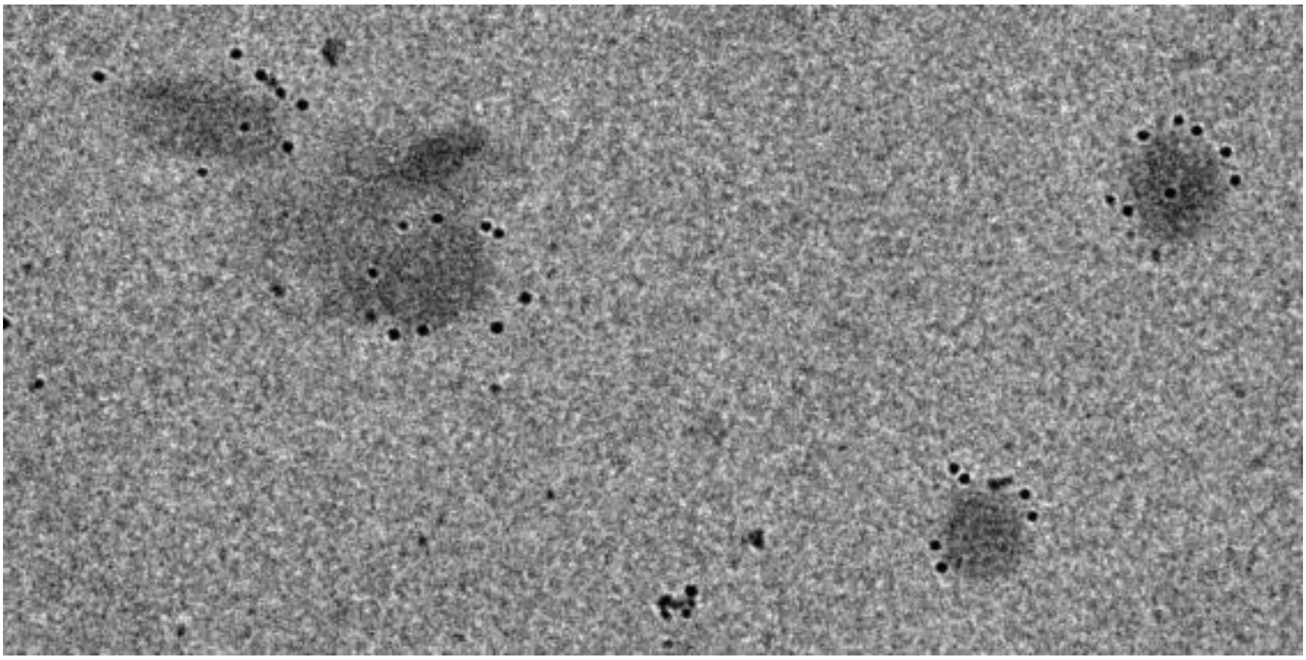

Immunolabelling of viral particles. Purified SBV particles were loaded on top of carbon coated copper grids. Incubation done with anti-G_C Ab 5F12 and further anti-mouse 10 nm gold fiducials conjugated Ab. Staining obtained 2% UAc. Images retrieved with a JEOL JEM1230 operating at 120kv.